LATTICE BOLTZMANN STUDY OF EVAPORATION PHENOMENA

Gianluca Laghezza
St. Anne's College
University of Oxford

A thesis submitted for the degree of
Doctor of Philosophy
Supervised by Prof. Julia M. Yeomans FRS
Michaelmas Term 2016

LATTICE BOLTZMANN STUDY OF EVAPORATION PHENOMENA

Gianluca Laghezza, St. Anne's College, University of Oxford

A thesis submitted for the degree of *Doctor of Philosophy*, Michaelmas Term 2016

Abstract

Evaporation phenomena are having a resurgent interest in the recent years thanks to new techniques that allow for better flow visualization and microfabrication techniques of surfaces with interesting wetting properties. From the theoretical point of view the development of simulation techniques for evaporation phenomena is a challenging work due to the presence of moving interfaces and multiphase flows.

Thanks to its mesoscopic nature, the Lattice Boltzmann method is an ideal candidate for the simulation of evaporation phenomena. Here we present a Lattice Boltzmann algorithm capable to correctly reproduce the diffusion-limited evaporation dynamics.

We apply this numerical method to study the dynamics of multiple droplets evaporating together and we compare the results with experimental measures. We show that the presence of other droplets can dramatically increase the evaporation lifetime compared to the single droplet case; we also investigate the competition between convection and collective effects.

We then develop a theory to predict the instability behaviour of liquid fronts in two dimensional confined geometries and we consider the interplay between capillary forces, wettability gradients and phase changes. We use LB simulations to investigate the effect of a three dimensional geometry that cannot be taken into account in the analytical theory.

Finally we investigate the effect of flows on droplet evaporation. We consider both buoyancy induced and external flows. We show that even when diffusion is the

dominant mechanism, flow effects are not negligible.

This thesis is dedicated to Giada and my parents

Publications Related to this Thesis

This thesis has used material from the following publications:

Chapter 3 uses material from: G. Laghezza, E. Dietrich, J. M. Yeomans, R. Ledesma-Aguilar, E. S. Kooij, H. J. W. Zandvliet, and D. Lohse. Soft Matter, 12:5787–5796, 2016. doi:10.1039/C6SM00767H. URL `http://dx.doi.org/10.1039/C6SM00767H`.

Acknowledgements

First and foremost, I would like to thank my supervisor, Prof Julia M. Yeomans FRS, for welcoming me at Oxford and guiding me during my DPhil journey. I am also deeply grateful to Dr Rodrigo Ledesma-Aguilar, who, even from distance, has always helped me during my work.

I also thank Erik Dietrich and collaborators at Twente for the collaboration that led to part of the work presented in the thesis.

I have enjoyed the time spent with my group colleagues Tyler Shendruk, Amin Doostmohammadi, Milos Knezevic, Matthew Andrew, Andrew Kaan Balin, Luuk Metselaar, Sumesh Thampi, Andreas Zottl, Mitya Pushkin, Romain Muller, Daiki Matsunaga, Fanlong Meng, Xin Wang which have all become good friends. A special thanks to the “good-old” Arnold Mathijssen, and his contagious enthusiasm.

I’d like to thank the friends that I met here: Mira Zorkot, Mohammed Fahes, Mattia Sormani, Viviana Ponta, Bruno Bertini, Philomena Yuqian Gan, Lorenzo Rovigatti, Gabriele Pezzulli, Pedro Fonseca, Piere Illien, Lorenzo Rossi, Benedetta Pacini, Ferdinando Randisi, Diana Di Paolo, Alessandro Geraldini, Kalpana Sivabalah, hoping these friendships will last in the future.

I also want to thank my family for supporting me in all my choices even when they imply a long distance from home.

Last but not least I want to thank Giada Nuzzo, for being the other half of the apple.

Contents

List of Figures

List of Tables

CHAPTER 1

Introduction

Evaporation is a common phenomenon that we experience everyday in countless situations; for example it is responsible for the formation of coffee stains but it is also used in technological applications such as inkjet printing, surface coating, cleaning, and the deposition of small particles[9–12].

Although from the theoretical point of view evaporation is well understood[13,14], recently there has been a resurgent interest in this phenomenon thanks to technological advances in fluid manipulation at the micrometer scale[15,16]; examples of such technologies are microfluidics[17], micropatterned and superhydrophobic surfaces[18–38].

On the other hand these new technologies have enabled a deeper understanding of the phenomena; for example thanks to advances in particle tracking[39] it has been possible to explain the so-called "coffee ring" effect[5] by showing that the deposition of particles at the contact line of an evaporating drop is due to a capillary flow from the interior of the drop to the contact line.

1.1 Drops

Since we will focus most of our attention on liquid droplets it is useful to give here a brief description of their main characteristics. A simple definition of a drop is of a small portion of liquid. Our everyday experience tells us that drops are usually spherical (if they are not too big); this behaviour comes from the fact that surfaces are energetically costly for liquids, and the spherical shape minimizes the drop's surface.

In order to quantify this energy cost we use the surface tension γ, which is the energy per unit area needed to increase a liquid's surface. Because of the spherical shape there is a difference in pressure Δp at the drop's surface given by the Young-Laplace equation[40]

$$\Delta P = \gamma \left(\frac{1}{R_1} + \frac{1}{R_2} \right) = \frac{2\gamma}{R} \tag{1.1}$$

where R_1 and R_2 are the principal radii of curvature and R the mean curvature. In Eq. 1.1 gravity has not been considered, but in general it causes a gradient in pressure of the form

$$\frac{dP}{dz} = -\rho g. \tag{1.2}$$

This means that for a spherical droplet there is a pressure variation due to gravity equal to

$$\Delta P(gravity) = -\rho g 2R. \tag{1.3}$$

However if this term is much smaller than the Young-Laplace pressure difference

$$\rho g 2R \ll \frac{2\gamma}{R} \tag{1.4}$$

it can be neglected and the shape of the droplet is spherical. From Eq. 1.4 we conclude that this happens for lengthscales smaller than

$$l_c = \sqrt{\frac{\gamma}{\rho g}} \tag{1.5}$$

which is called capillary length. For pure water at standard temperature and pressure

$l_c \approx 2.7mm$.

1.1.1 Droplet evaporation

Evaporation is a phase transition of the liquid phase of a given substance into its gaseous phase. It occurs when the concentration of the vapor of the substance is less than the saturation concentration.

The saturation concentration is the vapour concentration at which the vapour phase is in thermodynamic equilibrium with its liquid (or solid) phase at a given temperature in a closed system. Loosely speaking, evaporation occurs because a liquid substance is in a non-equilibrium situation with its vapour, so some of the liquid evaporates to restore the equilibrium. For a pure substance the liquid vapour equilibrium is described by the Clausius-Clapeyron equation[41]

$$\ln \frac{P_2}{P_1} = -\frac{\Delta H_{vap}}{R_{gas}} \left(\frac{1}{T_2} - \frac{1}{T_1} \right) \tag{1.6}$$

where P_1, P_2 are the vapour pressures at temperatures T_1, T_2 respectively, ΔH_{vap} is the enthalpy of vaporization, and R_{gas} is the universal gas constant. The vapour pressure is directly connected to the saturation concentration through the equation of state for ideal gases. During evaporation the vapour concentration is not uniform (intuitively we expect more vapour to be near the liquid phase) in either space or time, thus it will be subject to diffusion.

We will now describe in more detail the dynamics of the vapour concentration of an evaporating droplet.

Let us consider a drop of a fluid A surrounded by another fluid B. The drop will shrink if the concentration of A in fluid B is less than its saturation value c_s. The terminology depends on whether A and B are liquid-gas, gas-liquid or liquid-liquid. Shrinking in the liquid-gas case (e.g., a water droplet in air) is usually called evaporation, whereas in the latter two cases (bubble in liquid, or a droplet in liquid) it is called dissolution. In most dissolution cases of interest, thermal exchanges are negligible so we consider the dissolution as isothermal.

In order to determine the temporal evolution of the drop, one has to determine the rate-limiting step in the mass exchange; in principle this could be either the transfer rate of fluid A across the droplet interface, or the diffusion of the solute through the bulk. However for almost every liquid, transfer rates across the interface are of the order of 10^{-10} s[15], much faster than diffusion timescales, so diffusion is the rate-limiting process. The temporal evolution of the solute concentration field $c(r,t)$ (where r is the distance from the drop's center; we are assuming radial symmetry) is then described by the diffusion equation

$$\frac{\partial c(r,t)}{\partial t} = D\nabla^2 c(r,t) \tag{1.7}$$

where D is the diffusion coefficient of the solute through the bulk. If the dissolution of the droplet takes sufficient time, the concentration reaches a steady state and we can describe the concentration field by the Laplace equation:

$$\nabla^2 c(r) = 0. \tag{1.8}$$

In order to completely define the problem we have to fix boundary conditions for Eq. 1.8. First we fix the solute concentration at infinity, $c(r \to \infty) = c_\infty$. At the drop interface we assume the concentration in the bulk to be the saturation value, i.e., $c = c_s$. If the drop radius is R, then the concentration profile obtained from Eq. 1.8 is

$$c(r) - c_s = \frac{R}{r}(c_s - c_\infty). \tag{1.9}$$

The evaporative flux at the droplet surface is

$$J = -\frac{D}{\rho_d}\left.\frac{dc(r)}{dr}\right|_{r=R} \tag{1.10}$$

where ρ_d is the droplet density. Using Eq. 1.9 J is

$$J = \frac{D}{R}\frac{c_s - c_\infty}{\rho_d}. \tag{1.11}$$

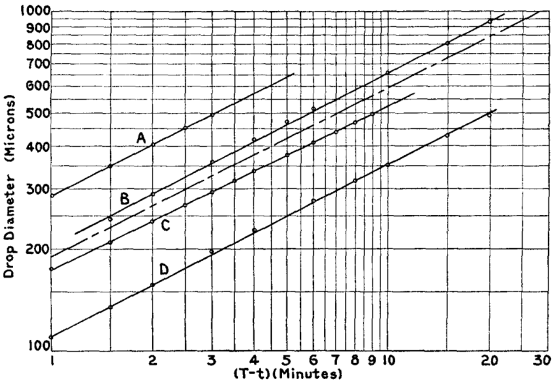

Figure 1.1: Temporal evolution of water drops evaporating in air; the straight lines have a slope of 0.5 as required from the D^2 law. Line A is water evaporating in air at $21.7°C, 0\%$ relative humidity (RH); B $20.3°C, 42\%$ RH; C $19.6°C, 53\%$ RH; D $20.8°C, 89\%$ RH. From Ref.[2].

Integrating over the drop surface one gets the rate of volume change

$$\frac{dV}{dt} = -4\pi R D \frac{c_s - c_\infty}{\rho_d} \tag{1.12}$$

from which one can derive the temporal evolution of R

$$R^2(t) = 2D\frac{c_s - c_\infty}{\rho_d}(t_{ev} - t) \tag{1.13}$$

which is the so-called “D^2 law”[1].

The diffusion-limited model of evaporation has been fully validated experimentally[2,42]. Figure 1.1 shows one of the earliest measurements of water drops evaporating in air compared with theoretical predictions and the D^2 law is clearly observed.

---

[1] The D in the “D^2 law” should not to be confused with the D in Eq. 1.13, which is a diffusion constant. The name “D^2 law” indicates the temporal evolution of the droplet diameter, while in Eq. 1.13 we use the droplet radius R. We keep the term “D^2 law” because it is the standard nomenclature used in the field.

1.2 Surface droplets

The interaction of droplets with solid surfaces depends both on the liquid substance forming the droplet and the solid. If a droplet is in contact with a solid it has an associated surface tension γ_{SL}; there is also a surface tension between the solid and the gas phase, indicated as γ_{SG}. At the three-phase contact line these three surface tensions are in equilibrium and determine the contact angle of the droplet sitting on the solid surface.

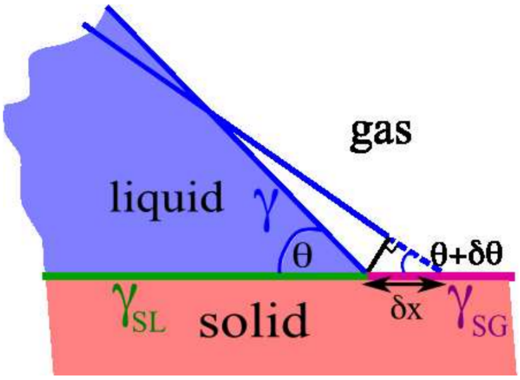

Figure 1.2: Illustration of the three-phase contact line with the three surface tensions described in the text. θ is the droplet's contact angle. From Ref.[3].

Figure 1.2 shows the balance of the three surface tensions. If we move the contact line by an amount δx we have an increase in the system's energy δE per unit area given by

$$\delta E = (\gamma_{SL} - \gamma_{SG} + \gamma \cos\theta)\delta x. \tag{1.14}$$

The condition for equilibrium, $\delta E/\delta x = 0$, leads us to the Young contact angle equation[43]

$$\cos\theta = \frac{\gamma_{SG} - \gamma_{SL}}{\gamma}. \tag{1.15}$$

Considering surface water droplets, if a solid has $\theta < 90^\circ$ it is called hydrophilic; if $\theta > 90^\circ$ it is called hydrophobic. A pictorial illustration of different wetting properties

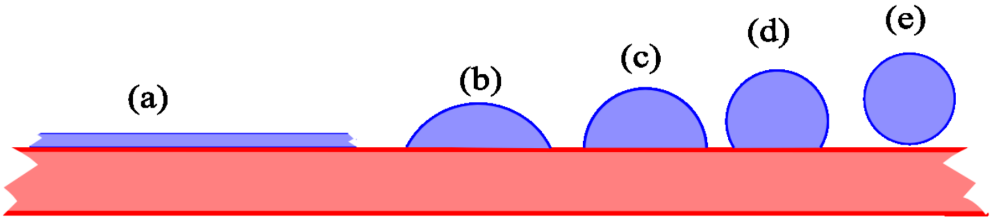

Figure 1.3: Illustration of drops with different contact angles. θ increases going from the left to the right. (a) illustrates complete wetting ($\theta = 0$); (b) hydrophilic ($\theta < 90°$), (c) neutrally wetting ($\theta = 90°$), (d) hydrophobic ($\theta > 90°$) and (e) perfectly hydrophobic surface ($\theta = 180°$). From Ref.[3].

is given in Fig. 1.3.

1.2.1 Evaporation

The mathematical treatment of surface droplet evaporation is the same as the one described in Sec. 1.1.1; however an additional boundary condition should be added to the ones used in Sec. 1.1.1, since the presence of the solid surface poses a no-flux boundary condition. If we assume the surface to be located at $z = 0$ the no-flux boundary condition is

$$\boldsymbol{J}(z = 0) = -D\nabla c = 0. \tag{1.16}$$

From a mathematical point of view, this problem has an electrostatic analogous of a charged conductor of the same shape as the droplet where $c(r)$ plays the role of the electrostatic potential and J of the electric field. Because of the no-flux boundary condition at the solid surface, we can use the method of the images, thus reducing the boundary conditions to the two described in Sec. 1.1.1: we fix solute concentration at infinity, $c(r \to \infty) = c_\infty$, and at the drop interface we have $c = c_s$.

This analogy has been used to analytically solve the problem[11,14]. Following Popov[11], we can write the time variation of the droplet volume V as

$$\frac{dV}{dt} = -\frac{\pi L D(c_s - c_\infty)}{2\rho_d} f(\theta) \tag{1.17}$$

where L is the drop footprint diameter, θ the contact angle and

$$f(\theta) = \frac{\sin\theta}{1+\cos\theta} + 4\int_0^\infty \frac{1+\cosh 2\theta\tau}{\sinh 2\pi\tau}\tanh[(\pi-\theta)\tau]\mathrm{d}\tau \tag{1.18}$$

is a factor that takes into account the effect of the contact angle on the dissolution dynamics.

The volume of a drop can vary in (at least) two ways during evaporation: either L varies and θ remains constant, or the opposite happens. The first mode of evaporation is called constant contact angle (CA) and the second one constant contact radius (CR). We can express the volume of a drop as the volume of a spherical cap

$$V = \frac{\pi L^3}{24}\frac{\sin\theta(2+\cos\theta)}{(1+\cos\theta)^2} \tag{1.19}$$

and by substituing this equation in Eq. 1.17 we can obtain the droplet's lifetime. In the CA mode we have $\dot{\theta} = 0$, while in the CR mode $\dot{L} = 0$. The resulting lifetime in the CR mode is

$$\tau_{CR} = \left(\frac{2(1+\cos\theta_0)^2}{\sin\theta_0(2+\cos\theta_0)}\right)^{2/3}\int_0^{\theta_0}\frac{2\mathrm{d}\theta}{f(\theta)(1+\cos\theta)^2} \tag{1.20}$$

while in the CA mode it is

$$\tau_{CA} = \left(\frac{2(1+\cos\theta_0)^2}{\sin\theta_0(2+\cos\theta_0)}\right)^{2/3}\frac{\sin\theta_0(2+\cos\theta_0)}{f(\theta_0)(1+\cos\theta_0)^2} \tag{1.21}$$

where θ_0 is the initial contact angle and the time has been non-dimensionalized by

$$T = \left(\frac{3V_0}{2\pi}\right)^{2/3}\frac{\rho_d}{2D(c_s-c_\infty)} \tag{1.22}$$

i.e. $\tau = t/T$.

Eqs. 1.20-1.22 indicate that the "D^2 law" is valid for surface droplets too, and the effect of different contact angles is to scale the droplet lifetime by a constant factor, but the functional dependence dictated by the D^2 law remains intact. These results will be used throughout the thesis.

1.2.2 Experimental observations

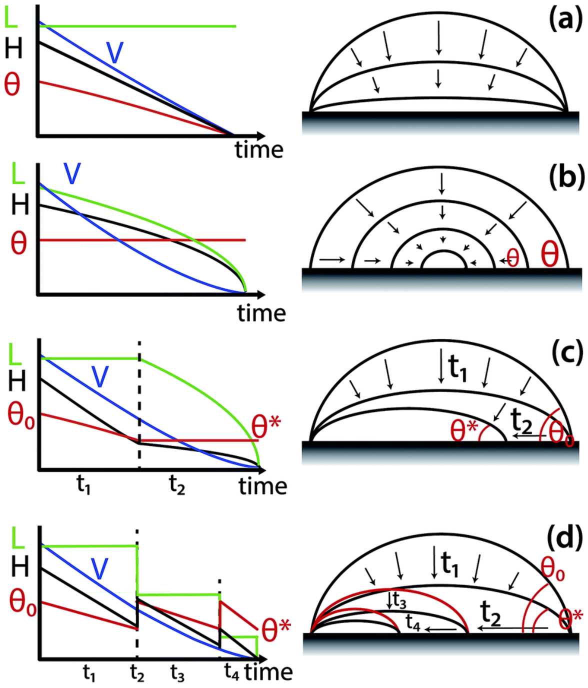

Figure 1.4: The four different evaporation modes of a sessile droplet: (a) CR mode, (b) CA mode, (c) stick-slide mode, (d) stick-jump mode. L is the droplet contact footprint, H its height and θ its contact angle. The left figures show the temporal evolution of H, L, θ while the right figures are pictorial illustrations of each dissolution mode. From Ref.[4].

As described in the previous section, surface droplets also follow the D^2 law, although their interaction with surfaces leads to a richer behaviour in their evaporation. In recent years technological advances have allowed us to study droplet and bubble behaviour down to the nanometer scale[4,44–63].

Four different evaporation modes have been identified: in addition to the constant contact angle and constant contact radius described in the previous section there are two other evaporation mechanisms. The first one is the stick-slide mode: in this mode the drop begins to evaporate in the CR mode, and when the contact angle reaches a critical value θ^*, switches to the CA mode until it dries completely.

The other one is called stick-jump mode: the droplet first dissolves in the CR mode but when its contact angle reaches a critical value θ_{crit} the droplet's contact radius jumps to a smaller value; due to mass conservation its contact angle jumps to a higher value than θ_{crit} and then the dissolution is again in a CR mode. Usually there is more than one jump during the evaporation process. The four modes of evaporation are summarized in Fig. 1.4.

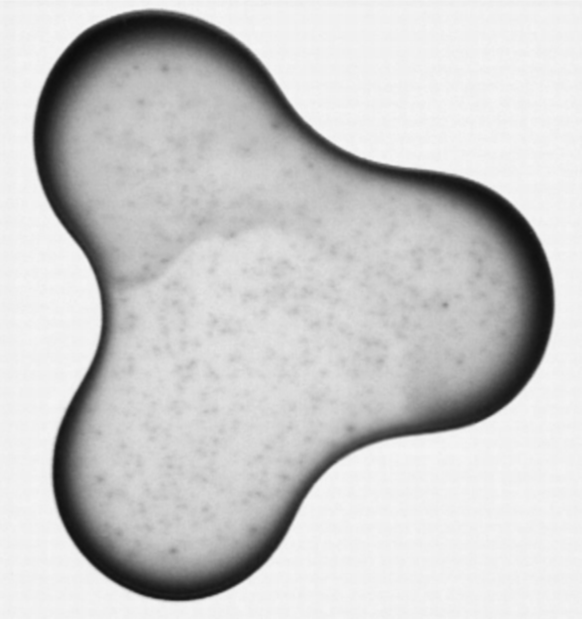

Figure 1.5: Particles deposited by an evaporating coffee droplet containing 1 wt% solids. From Ref.[5].

These different behaviours are caused by the fact that every surface always has some roughness that causes pinning of the droplet. For the CR mode the whole contact line is pinned throughout the whole evaporation process. This is the cause of the so-called coffee ring effect. If the drop contains some particles and its contact line is pinned, then during evaporation the particles will migrate towards the contact line due to flows inside the droplet and they will deposit there (see Fig. 1.5).

Stick-slide and stick-jump modes are also caused by the pinning of droplets but only at some points: the mechanism is illustrated in Fig. 1.6.

1.3 Buoyancy and flow effects on evaporation

In the previous analysis of evaporation we did not take into account buoyancy or flows. Buoyancy can have an effect on evaporation if the droplet's vapour has a different

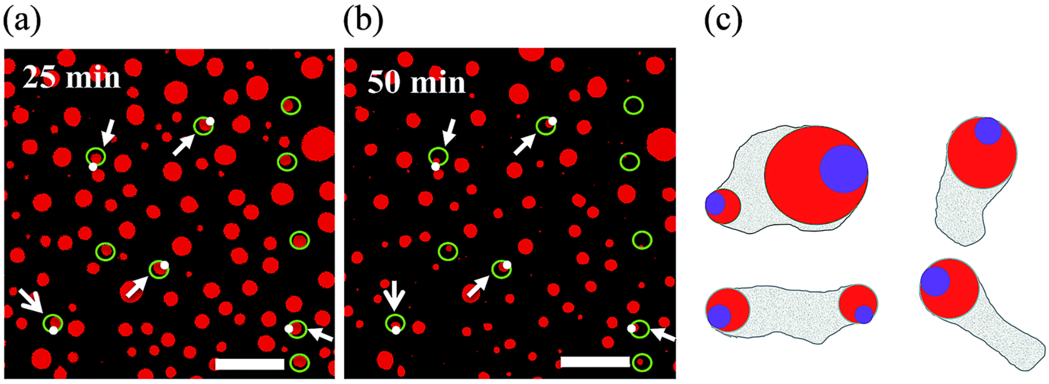

Figure 1.6: MMA (methyl methacrylate) nanodroplets on coated silicon wafers dissolving in water. (a) and (b) show the same region at subsequent times; green circles and white dots are in the same position in both figures (scale bar $40\mu m$). White dots indicate the pinning sites of some droplets. (c) shows the evaporation mechanism of the droplets: the pinning sites remain fixed for each droplet throughout evaporation, thus causing the stick-jump behaviour. From Ref.[4].

density than the surrounding fluid. For example water vapour is lighter than air, so it tends to move away from the droplet faster than by pure diffusion alone. In Ref.[6] it was shown that millimeter sized droplets evaporate faster than predicted for the pure diffusive case. Fig. 1.7 shows a log-log plot of the temporal evolution of an evaporating water droplet's radius in air. According the D^2 law this should scale as $R \propto (t - t_{ev})^a$ with $a = 0.5$ while, as the plot shows, the exponent in this case is $a = 0.6$.

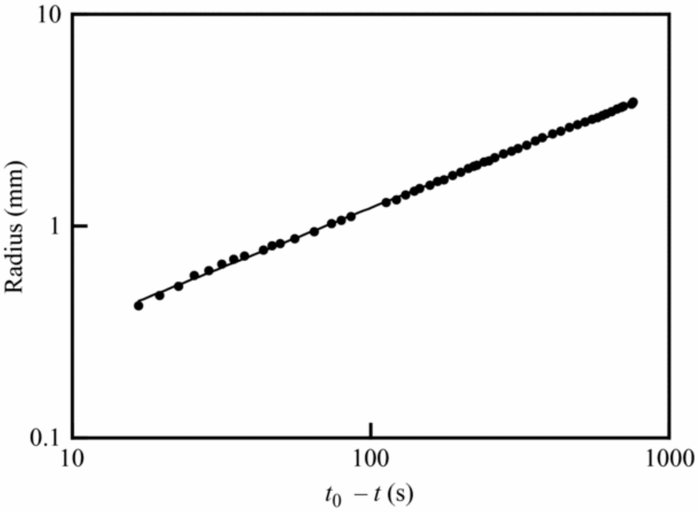

Figure 1.7: Log-log plot of droplet radius over time of a water droplet evaporating in air. The fitting line has a slope $a = 0.6$, thus indicating a departure from the D^2 law which dictates the temporal evolution of the radius to be $R \propto (t - t_{ev})^{0.5}$. From Ref.[6].

In order to quantify the effect of buoyancy forces or flows it is useful to introduce the Rayleigh number[64] which is the ratio of buoyancy forces to viscosity forces and diffusion. Consider a system like the one shown in Fig. 1.8: there is a fluid A evaporating (or dissolving) in a second fluid B, thus producing a concentration gradient along the vertical direction.

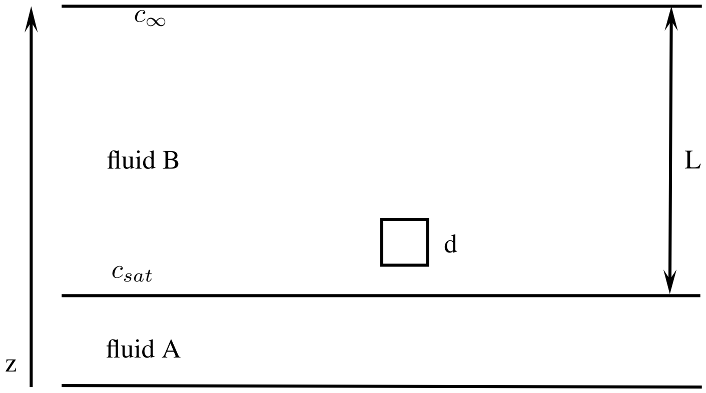

Figure 1.8: Sketch of a fluid A, dissolving in a second fluid B, and subject to buoyant forces. The concentration of fluid A vapour varies from c_{sat} at the interface of the two fluids to c_∞ at a distance L from the fluid interface.

Evaporation is driven by fixing the concentration of fluid A to a value $c_\infty \neq c_{sat}$ at a distance L from the fluid interface. Consider a volume of linear size d as in Fig. 1.8. Because of evaporation of fluid A, the volume has an initial density difference $\Delta\rho_0$ with the surrounding fluid; we can write $\Delta\rho_0$ as

$$\Delta\rho_0 = \rho_B \beta_c \Delta c_L \tag{1.23}$$

with $\beta_c = 1/\rho \quad \partial\rho/\partial c$, the solutal expansion coefficient, and $\Delta c_L = c_{sat} - c_\infty$ is the difference in concentration of fluid A between the fluids interface and the boundary at distance L from the fluid interface were the concentration of the vapour of A is fixed. This density difference will in general evolve in time and we denote it by $\Delta\rho(t)$. Due to this density difference the fluid volume experiences a buoyancy force given by

$$g\Delta\rho(t)d^3 \tag{1.24}$$

with g being gravitational acceleration. Acting against the buoyancy is the viscous force

$$\eta d\frac{dz_v}{dt} \tag{1.25}$$

where z_v is the vertical spatial coordinate of the volume considered and η the fluid viscosity. Balancing the two forces gives

$$g\Delta\rho(t)d^3 = \eta d\frac{dz_v}{dt}. \tag{1.26}$$

We have also to remember that due to diffusion, $\Delta\rho(t)$ will vary in time according to

$$\frac{d\Delta\rho(t)}{dt} = -\frac{D\Delta\rho(t)}{d^2} \rightarrow \Delta\rho(t) = \Delta\rho_0 \exp\left(-\frac{Dt}{d^2}\right) \tag{1.27}$$

Combining Eqs. 1.23-1.26-1.27 together we obtain the upward velocity of the volume of fluid considered

$$\frac{dz_v}{dt} = \frac{g\rho_B\beta_c d^2\Delta c_L}{\eta}\exp\left(-\frac{Dt}{d^2}\right). \tag{1.28}$$

By integrating this equation over time one obtains the total distance travelled by the fluid element

$$\int_0^\infty \frac{dz_v}{dt}\mathrm{dt} = \int_0^\infty \frac{g\rho\beta_c d^2\Delta c_L}{\eta}\exp\left(-\frac{Dt}{d^2}\right)\mathrm{dt} \tag{1.29}$$

which gives

$$z_v = \frac{g\rho\beta_c d^4\Delta c_L}{\eta D}. \tag{1.30}$$

Since we are interested in situations where this upward motion is non-negligible, the value of z_v is always greater than the length scale L (since the volume will reach the top of the system in a finite time)

$$\frac{g\rho\beta_c d^4 \Delta c_L}{\eta D} > L. \tag{1.31}$$

In order to express this equation in a dimensionless form we introduce the dimensionless factor f as $f = L/d$; this gives

$$\frac{g\rho\beta_c L^3 \Delta c_L}{\eta D} > f^4. \tag{1.32}$$

The left hand side of the previous equation is the dimensionless Rayleigh number

$$Ra = \frac{g\beta_c L^3 \Delta c_L}{\nu D} \tag{1.33}$$

where we have used the kinematic viscosity $\nu = \eta/\rho_B$. As explained in the beginning of the section it is the ratio of buoyancy forces over viscosity and diffusion.

Another useful dimensionless number is the Sherwood number which is the ratio of the measured mass dissolution rate to the one predicted assuming pure diffusion

$$Sh = \frac{\dot{m}_{measured}}{\dot{m}_{theory}}. \tag{1.34}$$

A recent experiment[7] has studied the dissolution behaviour of sessile droplets over a wide range of the Rayleigh numbers; the results are shown in Fig. 1.9.

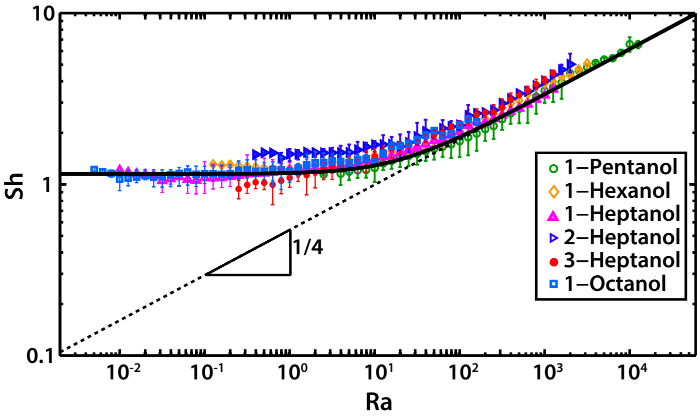

Figure 1.9: Sh-Ra plot of different alcohols dissolving in water. From Ref.[7]

The figure is a plot of the Sherwood number as a function of the Rayleigh number for several droplets of different alcohols dissolving in water. A Sherwood number equal to 1 means that the dissolution rate is the one expected by diffusion theory, while $Sh > 1$ indicates a dissolution faster than the one due only to diffusion. The main result of the plot is that for small Rayleigh numbers (which means either small droplets, small density differences or large values of the diffusion constant D) the dissolution is dominated by diffusion, while for high Rayleigh numbers buoyancy effects become important. A more detailed analysis of these results is carried out in Chapter 6.

1.4 Outline of the thesis

The thesis is organized as follows: after the introduction made in this chapter, Chapters 2 and 3 describe the Lattice Boltzmann method and how to implement evaporation in this numerical method in detail. We first describe the Boltzmann equation and its relation with the Navier-Stokes equation. We then introduce the Lattice Boltzmann method as a discretization of the Boltzmann equation. We describe the Cahn-Hilliard model used to describe multiphase flow and the implementation of evaporation in this model; we also validate results obtained by a Lattice Boltzmann method coupled with the Cahn-Hilliard model against analytical prediction for the evaporation dynamics of simple systems.

In most situations of practical interest, an analytical approach to the evaporation dynamics like the one developed in this chapter is not possible, making numerical simulations essential in order to predict the behaviour of these systems. The next three chapters discuss different applications of the simulation methods developed for evaporation. Chapter 4 describes collective effects that arise from the presence of multiple droplets evaporating. We analyse the evaporation dynamics of several complex systems, and we compare simulation results with experimental measurements.

Chapter 5 studies the role of evaporation and condensation on the stability of thin films in microchannels. First we develop a 2D theory to analyze the effect of evaporation and condensation on the stability of flows in confined geometries and we show that these phase changes play an active role in the instability of these systems. We then use numerical simulations to explore the effect of the third dimension that cannot be taken into account in an analytical approach to the problem.

As described in Sec. 1.3, flows have an important effect on the evaporation dynamics of droplets and the effect of buoyancy and external flows on evaporation dynamics is studied in Chapter 6. We perform numerical simulations both in the case of buoyancy induced flows and external flows, and we confirm that, even at small Rayleigh numbers, flows have a very large effect on evaporation.

Finally we summarize our findings in the conclusions. More technical details are presented in the appendices.

CHAPTER 2

Lattice Boltzmann methods

The Lattice Boltzmann algorithm is a relatively new computational technique used for the study of fluid dynamics. It was developed in the late 80's in the wake of a previous numerical method, the so-called lattice-gas cellular automata[65–70] and during the last decades has gained a growing popularity in the community of fluid simulations. As the name suggests, the method starts from the Boltzmann equation in order to simulate fluids. By comparison, more traditional computational fluid dynamics (CFD) techniques are, loosely speaking, direct discretizations of the equations governing fluid motion, the Navier-Stokes equations. The main advantages of the Lattice Boltzmann method lie in its intrisic parallel nature and in the possibility to include microscopic physical features.

2.1 Physical description of fluids

Let us consider a macroscopic system formed by N molecules. If quantum effects are negligible, the dynamics of the system is determined entirely by Newton classical equations

$$\begin{aligned}\frac{d\boldsymbol{x}_i}{dt} &= \frac{\boldsymbol{p}_i}{m}, \\ \frac{d\boldsymbol{p}_i}{dt} &= \boldsymbol{F}_i\end{aligned} \tag{2.1}$$

where $i = 1 \ldots N$ denotes the i-th particle, $\boldsymbol{x}_i$ is its position, $\boldsymbol{p}_i$ its linear momentum and $\boldsymbol{F}_i$ the force on it. Given initial and boundary conditions, Eqs. 2.1 determine exactly the behaviour of each particle. However, for macroscopic systems the number of particles is of the order of the Avogadro number $N_a \approx 10^{23}$ which makes this analytical description impossible. Moreover, for all practical purposes, in order to describe a macroscopic fluid we need a far less detailed knowledge than the one given by Newton equations.

If we have a fluid we usually describe it with few variables, such as the velocity field, density, pressure, etc. instead of the $6N$ variables that we would need with Newton equations. The dynamics of the entire system is then given by the continuity and Navier-Stokes equations

$$\begin{aligned}\frac{\partial n}{\partial t} + \nabla \cdot (n\boldsymbol{u}) &= 0 \\ n\left(\frac{\partial \boldsymbol{u}}{\partial t} + \boldsymbol{u} \cdot \nabla \boldsymbol{u}\right) &= -\nabla P + \nabla \cdot \left(\eta(\nabla \boldsymbol{u} + (\nabla \boldsymbol{u})^T)\right) + n\boldsymbol{F}\end{aligned} \tag{2.2}$$

where $\boldsymbol{u}$ is the velocity field, P the pressure, n the fluid's density, η the viscosity and $\boldsymbol{F}$ the external forces on the fluid (for simplicity we considered the fluid as incompressible).

2.1.1 The Boltzmann equation

A description which lies between the Navier-Stokes and Newton's equations is given by the Boltzmann equation. In this framework we describe the particles' motion in a probabilistic way; instead of calculating the exact position and velocity of each particle at each time we calculate the probability of a particle being at some position and having a certain velocity at a definite time. If we introduce a probability density $f(\boldsymbol{x}, \boldsymbol{v}, t)$

then the quantity

$$\delta n = f(\boldsymbol{x}, \boldsymbol{v}, t)\delta\boldsymbol{x}\delta\boldsymbol{v}$$

is the average number of particles that at time t have their position in the interval$[\boldsymbol{x}, \boldsymbol{x}+\delta\boldsymbol{x}]$ and velocity in the interval $[\boldsymbol{v}, \boldsymbol{v}+\delta\boldsymbol{v}]$. The temporal evolution of f is given by the Boltzmann equation[71,72]

$$\frac{\partial f}{\partial t} + \boldsymbol{v}\cdot\nabla f + \boldsymbol{F}\cdot\frac{\partial f}{\partial \boldsymbol{v}} = \left(\frac{df}{dt}\right)_{coll} \tag{2.3}$$

where $\boldsymbol{F}$ is the force on each particle. Eq. 2.3 describes how the distribution function f can vary in time: either because of the streaming of the particles due to the force field $\boldsymbol{F}$ (left-hand side of Eq. 2.3) or because of collisions (right-hand side). The term on the right-hand side of Eq. 2.3 is called collision integral; it can be solved exactly in very few cases. However, the equilibrium properties of f can be derived with some assumptions which simplify the form of the collision integral.

Since collisions involve (at least) two particles, if we consider only binary collisions, the collision integral depends on the two-body distribution function $f(\boldsymbol{x}_1, \boldsymbol{v}_1, \boldsymbol{x}_2, \boldsymbol{v}_2, t)$ (shortened to f_{12}), i.e. the probability of having the particle 1 at position $\boldsymbol{x}_1$ with velocity $\boldsymbol{v}_1$ and particle 2 at position $\boldsymbol{x}_2$ with velocity $\boldsymbol{v}_2$. It is possible to write an evolution equation for f_{12} but it depends on the 3-particle distribution function f_{123}, and so on (this is the so-called BBGKY hierarchy[73–76]). In order to have a closed equation for f Boltzmann considered a dilute gas of point-like particles interacting only via a short-range two-body potential. Under these conditions the collision integral takes a simple form; if we consider a pair of particles having positions and velocities $\boldsymbol{x}_1, \boldsymbol{v}_1, \boldsymbol{x}_2, \boldsymbol{v}_2$ (shortened as 12), then all the collisions of the type $1'2' \rightarrow 12$ will increase the particle population in the state 12, while the collisions of the type $12 \rightarrow 1'2'$ will decrease the 12 population. The collision integral can then be written as[71]

$$\left(\frac{df}{dt}\right)_{coll} = \int (f_{1'2'} - f_{12})|\boldsymbol{v}_1 - \boldsymbol{v}_2|\sigma(|\boldsymbol{v}_1 - \boldsymbol{v}_2|, \Omega)\mathrm{d}\Omega\mathrm{d}^3\boldsymbol{v}_1\mathrm{d}^3\boldsymbol{v}_2 \tag{2.4}$$

where σ is the differential cross section of the collision and Ω is the solid angle of scattering. The final assumption is to assume that the particles entering a collision are uncorrelated; this is the famous "molecular chaos" or "Stosszahlansatz" assumption which leads to the result

$$f_{12} = f_1 f_2. \tag{2.5}$$

With this assumption it is possible to write the Boltzmann equation with only the one particle distribution function f

$$\frac{\partial f}{\partial t} + \boldsymbol{v} \cdot \nabla f + \boldsymbol{F} \cdot \frac{\partial f}{\partial \boldsymbol{v}} = \int (f_{1'} f_{2'} - f_1 f_2) |\boldsymbol{v}_1 - \boldsymbol{v}_2| \sigma(|\boldsymbol{v}_1 - \boldsymbol{v}_2|, \Omega) \mathrm{d}\Omega \mathrm{d}^3\boldsymbol{v}_1 \mathrm{d}^3\boldsymbol{v}_2. \tag{2.6}$$

2.1.2 The Maxwell-Boltzmann distribution

Although is not possible to solve the Boltzmann equation in the general case, it is relatively easy to obtain information about the distribution function f at equilibrium. We define the equilibrium distribution function f_e as the one that satisfies the identity

$$\left(\frac{df_e}{dt}\right)_{coll} = 0. \tag{2.7}$$

By applying the definition to Eq. 2.6 we get

$$f_1 f_2 = f_{1'} f_{2'} \tag{2.8}$$

(the subscript e is omitted) and by taking the log of both sides

$$\ln(f_1) + \ln(f_2) = \ln(f_{1'}) + \ln(f_{2'}). \tag{2.9}$$

Thus $\ln f_e$ has to conserve during collisions and since there are three collision invariants (number of particles, linear momentum and kinetic energy) $\ln f_e$ has to be a function of them. We can therefore write $\ln(f_e)$ as

$$\ln(f_e) = a + b_i v_i + c v^2 \tag{2.10}$$

and calculate the values of the parameters a, b_i, c by imposing the conservation of the number of particles, momentum and energy

$$\begin{aligned}\int f \mathrm{d}\boldsymbol{v} &= n,\\ \int f v_i \mathrm{d}\boldsymbol{v} &= n u_i,\\ \int f v^2 \mathrm{d}\boldsymbol{v} &= n u^2 + 3n\theta\end{aligned} \tag{2.11}$$

where $\theta = k_b T$. The resulting expression for f is the famous Maxwell-Boltzmann distribution

$$f_e(v) = \frac{n}{(2\pi\theta)^{3/2}} \exp\left(-\frac{(v-u)^2}{2\theta}\right). \tag{2.12}$$

2.1.3 From Boltzmann to Navier-Stokes equation

It is possible to show that the Navier-Stokes equation can be derived from the Boltzmann equation. The most used method is the Chapman-Enskog expansion[77], although other methods exist[78]. The Chapman-Enskog method is essentially a perturbation expansion of the Boltzmann equation; first we write the distribution function as

$$f = f_0 + \epsilon f_1 + \ldots$$

where $f_0 = f_e$ and f_1 is the non equilibrium contribution. The perturbation parameter ϵ is assumed to be the Knudsen number

$$Kn = \frac{\text{mean free path}}{\text{macroscopic length scale}}.$$

If $Kn << 1$ the mean free path of the fluid molecules is very small compared to the typical length scale of the system, and continuum fluid mechanics is valid. By using a multiscale expansion it is possible to derive the Navier-Stokes equation.

Since the original Chapman-Enskog analysis is quite long, here we present a simplified derivation of the Navier-Stokes equation from the Boltzmann equation. We first introduce the BGK approximation[79], which is an approximation for the collision integral. From a physical point of view the main role of the collision integral is to drive the distribution function towards the equilibrium one. Thus the simplest expression we can assume for the collision integral is that of a relaxation of f towards f_e

$$\left(\frac{df}{dt}\right)_{coll} = \frac{f_e - f}{\tau} \tag{2.13}$$

where τ is the relaxation time. With this assumption the Boltzmann equation takes a much simpler form:

$$\partial_t f + v_\alpha \partial_\alpha f + F_\alpha \partial_{v_\alpha} f = \frac{f_e - f}{\tau} \tag{2.14}$$

where we have used Einstein summation convention ($\alpha = x, y, z$); we can then write f as

$$f = f_e - \tau(\partial_t f + v_\alpha \partial_\alpha f + F_\alpha \partial_{v_\alpha} f). \tag{2.15}$$

Knowing the equilibrium distribution (Eq 2.12) we can calculate several moments of f_e that we will need later

$$\begin{aligned}
\int f_e \mathrm{d}\boldsymbol{v} &= n, \\
\int f_e(u_\alpha - v_\alpha)\mathrm{d}\boldsymbol{v} &= 0, \\
\int f_e(u_\alpha - v_\alpha)(u_\beta - v_\beta)\mathrm{d}\boldsymbol{v} &= n\theta\delta_{\alpha\beta}, \\
\int f_e(u_\alpha - v_\alpha)(u_\beta - v_\beta)(u_\gamma - v_\gamma)\mathrm{d}\boldsymbol{v} &= 0, \\
\int f_e(u_\alpha - v_\alpha)(u_\beta - v_\beta)(\boldsymbol{u}^2 - \boldsymbol{v}^2)\mathrm{d}\boldsymbol{v} &= 5n\theta^2\delta_{\alpha\beta}.
\end{aligned} \tag{2.16}$$

We also demand the moments of F to satisfy

$$\begin{aligned}\int F_\alpha \partial_{v_\alpha} f \mathrm{d}\boldsymbol{v} &= 0,\\ \int F_\beta \partial_{v_\beta} f v_\alpha \mathrm{d}\boldsymbol{v} &= -nF_\alpha,\\ \int F_\gamma \partial_{v_\gamma} f v_\alpha v_\beta \mathrm{d}\boldsymbol{v} &= -n(F_\alpha u_\beta + F_\beta u_\alpha),\\ \int F_\delta \partial_{v_\delta} f v_\alpha v_\beta v_\gamma \mathrm{d}\boldsymbol{v} &= -n[(F_\alpha(\theta\delta_{\beta\gamma} + u_\beta u_\gamma) + (F_\beta(\theta\delta_{\alpha\gamma} + u_\alpha u_\gamma)(F_\gamma(\theta\delta_{\alpha\beta} + u_\alpha u_\beta)].\end{aligned} \tag{2.17}$$

To get the continuity equation we integrate Eq. 2.14 and use Eqs. 2.11-2.16-2.17 (to first order in derivatives)

$$\begin{aligned}&\partial_t \int f \mathrm{d}\boldsymbol{v} + \partial_\alpha \int f v_\alpha \mathrm{d}\boldsymbol{v} + \int F_\alpha \partial_{v_\alpha} f \mathrm{d}\boldsymbol{v} = \frac{1}{\tau}\int (f_e - f)\mathrm{d}\boldsymbol{v}\\ &\Rightarrow \partial_t n + \partial_\alpha(n u_\alpha) = 0.\end{aligned} \tag{2.18}$$

To obtain the Navier-Stokes equation we first multiply Eq. 2.14 by v_α and integrate

$$\begin{aligned}&\partial_t \int f v_\alpha \mathrm{d}\boldsymbol{v} + \partial_\beta \int f v_\alpha v_\beta \mathrm{d}\boldsymbol{v} + F_\beta \int \partial_{v_\beta}(f v_\alpha)\mathrm{d}\boldsymbol{v} = \frac{1}{\tau}\int (f_e - f) v_\alpha \mathrm{d}\boldsymbol{v}\\ &\Rightarrow \partial_t(n u_\alpha) + \partial_\beta \int f v_\alpha v_\beta \mathrm{d}\boldsymbol{v} = nF_\alpha.\end{aligned} \tag{2.19}$$

Using Eq. 2.15 we have for the integral term (to first order in derivatives)

$$\begin{aligned}\int f v_\alpha v_\beta \mathrm{d}\boldsymbol{v} = \int f_e v_\alpha v_\beta \mathrm{d}\boldsymbol{v} - \tau \Big(\partial_t \int f_e v_\alpha v_\beta \mathrm{d}\boldsymbol{v}\\ + \partial_\gamma \int f_e v_\alpha v_\beta v_\gamma \mathrm{d}\boldsymbol{v} + nF_\alpha u_\beta + n u_\alpha F_\beta\Big) + O(\partial^2)\end{aligned} \tag{2.20}$$

which leads to

$$\partial_t(n u_\alpha) + \partial_\beta(n u_\alpha u_\beta) = -\partial_\alpha(n\theta) + nF_\alpha \tag{2.21}$$

which is known as the Euler equation. Using Eq. 2.18 we can rewrite it as

$$\partial_t u_\alpha + u_\beta \partial_\beta u_\alpha = -\frac{1}{n}\partial_\alpha(n\theta) + F_\alpha. \tag{2.22}$$

We need now to calculate the term

$$\begin{aligned}\partial_t\left(\int f_e v_\alpha v_\beta \mathrm{d}\boldsymbol{v}\right) &= \partial_t(n u_\alpha u_\beta + n\theta\delta_{\alpha\beta}) \\ &= \partial_t(n u_\alpha)u_\beta + n u_\alpha \partial_t u_\beta + \partial_t n\theta\delta_{\alpha\beta} + n\partial_t\theta\delta_{\alpha\beta} \\ &= -\partial_\gamma(n u_\alpha u_\gamma)u_\beta - \partial_\alpha(n\theta)u_\beta - nF_\alpha u_\beta - n u_\alpha u_\gamma \partial_\gamma u_\beta \\ &- u_\alpha\partial_\beta(n\theta) - n u_\alpha F_\beta - \partial_\gamma(n u_\gamma)\theta\delta_{\alpha\beta} - n u_\gamma \partial_\gamma(\theta\delta_{\alpha\beta}) - \frac{2}{3}\partial_\gamma u_\gamma \theta \\ &= -\partial_\gamma(n u_\alpha u_\beta u_\gamma) - \partial_\beta(n\theta)u_\alpha - \partial_\alpha(n\theta)u_\beta - n(F_\alpha u_\beta + F_\beta u_\alpha) \\ &- \partial_\gamma(n\theta u_\gamma)\delta_{\alpha\beta} - \frac{2}{3}n\theta\partial_\gamma u_\gamma\end{aligned} \tag{2.23}$$

where we have used the energy conservation equation to first order (it can be derived by multiplying the Boltzmann equation by $(v-u)^2$ and integrating)

$$\partial_t\theta + u_\alpha\partial_\alpha\theta = -\frac{2}{3}\partial_\alpha u_\alpha \theta + O(\partial^2). \tag{2.24}$$

We also need the term

$$\partial_\gamma \int f_e v_\alpha v_\beta v_\gamma \mathrm{d}\boldsymbol{v} = \partial_\beta(n\theta u_\alpha) + \partial_\alpha(n\theta u_\beta) + \partial_\gamma(n\theta u_\gamma)\delta_{\alpha\beta} + \partial_\gamma(n u_\alpha u_\beta u_\gamma). \tag{2.25}$$

Adding Eqs. 2.23-2.25 we have

$$\partial_t \int f_e v_\alpha v_\beta \mathrm{d}\boldsymbol{v} + \partial_\gamma \int f_e v_\alpha v_\beta v_\gamma \mathrm{d}\boldsymbol{v} = n\theta(\partial_\alpha u_\beta + \partial_\beta u_\alpha) - \frac{2}{3}n\theta\partial_\gamma u_\gamma. \tag{2.26}$$

Substituting this expression in Eq. 2.20 we finally get the Navier-Stokes equation

$$n\partial_t u_\alpha + n u_\beta \partial_\beta u_\alpha = -\partial_\alpha(n\theta) + nF_\alpha + \partial_\beta\left(\eta(\partial_\beta u_\alpha + \partial_\alpha u_\beta - \frac{2}{3}\partial_\gamma u_\gamma \delta_{\alpha\beta})\right) \tag{2.27}$$

where $\eta = n\theta\tau$ is the viscosity. The previous equation reduces to Eq. 2.2 for incompressible fluids if $P = n\theta = \rho k_B T$, which is the equation of state for ideal fluids.

2.2 The Lattice Boltzmann equation

As the title suggests, the lattice Boltzmann algorithm is a discretization of the Boltzmann equation on a lattice. This means that we have to dicretise both space and velocity variables (and time). We define δx as the lattice spacing, δt as the timestep and $c = \delta x/\delta t$ as the lattice velocity. If we choose a set of N discrete velocities we can write a discrete version of Eq. 2.14 as

$$f(x + v_i, v_i, t + \delta t) - f(x, v_i, t) + F(v_i) = \frac{1}{\tau}(f_e(x, v_i, t) - f(x, v_i, t)) \tag{2.28}$$

where $i = 1, \ldots, N$ and $F(v_i)$ is the discretization of the term $F_\alpha \partial_{v_\alpha} f$. In order to have a consistent scheme we have to choose the set of discrete velocities such that, for each i, $x + v_i$ is a lattice position. In the following we set $\delta t = 1$, unless otherwise stated. We also shorten the notation as $f(x, v_i, t) = f_i(x, t)$ and $F(v_i) = F_i$. All the previous constraints must hold in their discrete version, in particular for the F_i we have

$$\begin{aligned}
\sum_i F_i &= 0, \\
\sum_i F_i v_{i\alpha} &= -nF_\alpha, \\
\sum_i F_i v_{i\alpha} v_{i\beta} &= -n(F_\alpha u_\beta + u_\alpha F_\beta), \\
\sum_i F_i v_{i\alpha} v_{i\beta} v_{i\gamma} &= -n(F_\alpha(\theta\delta_{\beta\gamma} + u_\beta u_\gamma) + F_\beta(\theta\delta_{\alpha\gamma} + u_\alpha u_\gamma) + F_\gamma(\theta\delta_{\alpha\beta} + u_\alpha u_\beta)).
\end{aligned} \tag{2.29}$$

For the equilibrium distribution

$$\begin{aligned}
\sum_i f_{ie} &= n, \\
\sum_i f_{ie}(u_{i\alpha} - v_{i\alpha}) &= 0, \\
\sum_i f_{ie}(u_{i\alpha} - v_{i\alpha})(u_{i\beta} - v_{i\beta}) &= n\theta\delta_{\alpha\beta}, \\
\sum_i f_{ie}(u_{i\alpha} - v_{i\alpha})(u_{i\beta} - v_{i\beta})(u_\gamma - v_\gamma) &= 0, \\
\sum_i f_{ie}(u_{i\alpha} - v_{i\alpha})(u_{i\beta} - v_{i\beta})(\boldsymbol{u}^2 - \boldsymbol{v}^2) &= 5n\theta^2\delta_{\alpha\beta}.
\end{aligned} \tag{2.30}$$

The same sums applied to the non-equilibrium distribution functions f_i are used to define the macroscopic fields. It is possible to show that also in the discrete case Eq. 2.28 leads to the continuity and Navier-Stokes equations (also the heat conduction equation[80], but in most cases we work with a constant temperature); the derivation is the same as the one in the previous section. The dynamic viscosity ν is linked to the relaxation time τ (in 3D) via

$$\nu = \frac{c^2\delta t}{3}\left(\tau - \frac{1}{2}\right). \tag{2.31}$$

In order to implement the method we have to choose the dimension of the system and the set of velocities to use; the standard way to indicate these two variables is to use the abbreviation $DnQm$ where the first part refers to the dimension of the system and the second to the number of velocities. As an example, in the $D1Q3$ case, we are in one dimension and we have three velocities $v_i = (-1, 0, 1)$ (shown in Fig. 2.2). In this case a set of f_{ie} that satisfies the constraints of Eq. 2.30 is

$$\begin{aligned}
f_{-1e} &= \frac{1}{2}n(-u + \theta + u^2) \\
f_{0e} &= n(1 - \theta - u^2) \\
f_{1e} &= \frac{1}{2}n(u + \theta + u^2)
\end{aligned} \tag{2.32}$$

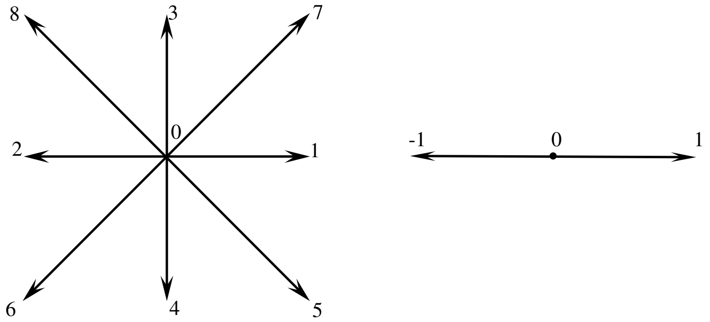

Figure 2.1: Velocities for the $D2Q9$ model (left) and the $D1Q3$ model (right).

model	i	w_i
D2Q9	0	$4/9$
	1-4	$1/9$
	5-8	$1/36$
D3Q15	0	$2/9$
	1-6	$1/9$
	7-14	$1/72$
D3Q19	0	$1/3$
	1-6	$1/18$
	7-18	$1/36$
D3Q27	0	$8/27$
	1-6	$2/27$
	7-14	$1/216$
	15-26	$1/54$

Table 2.1: Weights w_i for the most commonly used LB models.

In general, equilibrium distributions are written as

$$f_{ie} = n w_i \left[1 + \frac{3}{c^2} \boldsymbol{u} \cdot \boldsymbol{v}_i + \frac{9}{2c^4} (\boldsymbol{u} \cdot \boldsymbol{v}_i)^2 - \frac{3}{2c^2} \boldsymbol{u} \cdot \boldsymbol{u} \right] \tag{2.33}$$

where w_i are weights dependent on the particular set of velocities used. The weights for the most commonly used models are listed in Table 2.1.

It must be stressed that there is a reason for Eq. 2.33; one would expect the usual Maxwell-Boltzmann distribution for the f_{ie}. Eq. 2.33 is a series expansion of the MB distribution for small values of velocities, more precisely it is an expansion in the parameter u/c. As a result the LB algorithm can be used for velocities much smaller than the fluid's speed of sound, or equivalently for small Mach numbers $Ma \ll 1$; for the LB method the speed of sound is given by the lattice velocity c. The physical reason for this limitation is that compressiblility effects are not included in the method, thus we are limited in the range of Mach numbers attainable in simulations.

It is also worth mentioning that the LB method is not unconditionally stable for any choice of parameters; however in most situations instabilities occur quite early in simulations and a suitable set of parameters can be easily found. The implementation of the LB method is quite easy and this is one of its main advantages. In almost any implementation Eq. 2.28 is split in two steps: the collision step

$$f_i'(x,t) = f_i(x,t) + F_i - \frac{1}{\tau}(f_i(x,t) - f_{ie}(x,t)) \tag{2.34}$$

and the propagation step

$$f_i(x + v_i, t + 1) = f_i'(x,t). \tag{2.35}$$

One main advantage of the LB method over conventional CFD method is its locality; in fact, as Eqs. 2.34-2.35 show the evolution of the f_i is completely local. This feature gives the opportunity of an easy parallelization of the LB algorithm.

2.2.1 Boundaries

In most cases of interest there are some solid boundaries in the fluid. The usual boundary conditions implemented in fluid dynamics problems are no-slip boundary conditions, i.e. the velocity of the fluid at the boundary is the same as the velocity of the boundary itself (usually zero).

The most usual technique to implement no-slip boundary-conditions in the LB method is the so-called bounce-back method[81,82]. The method is illustrated in Fig. 2.2. For fluid lattice sites near solid lattice sites, the distribution functions simply bounce back on the boundary like a solid particle hitting a wall:

$$f_i(x, t + 1) = f_{-i}(x,t) \tag{2.36}$$

where the term f_{-i} denotes the distribution function relative to the velocity $v_{-i} = -v_i$, for example in the $D2Q9$ case $v_{-2} = v_1, v_{-3} = v_4$, etc. The physical boundary lies halfway between the two lattice sites. Other boundary conditions can be implemented, for a review see Ref.[83].

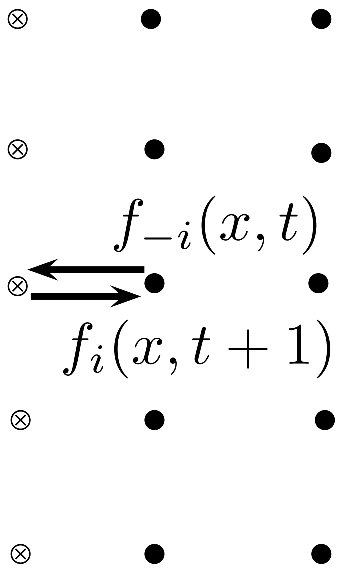

Figure 2.2: Illustration of bounce-back boundary conditions. The full points are fluid lattice sites, the crossed points are solid sites. The distribution functions are bounced back from the solid nodes.

2.3 Multiphase flows

Some of the most difficult systems to study with conventional CFD methods are multiphase systems, because of the presence of moving and deformable interfaces. Furthermore, the interaction between different fluids is difficult to implement into the Navier-Stokes equations given their macroscopic nature. The microscopic nature of the Boltzmann equation instead allows a simpler implementation of these interactions, thus enabling the study of fluid mixtures.

Several different implementations of multiphase systems have been proposed and used for the LB method[84–102]; in the following we describe a free-energy approach[86], using a binary fluid model known as the Cahn-Hilliard model. Within the Cahn-Hilliard approach, we model the liquid and gas phases as a binary fluid, where each phase is labelled using a phase field, $\phi(x, y, z, t)$, which varies continuously between two bulk phases separated by a diffuse interface. In the same spirit, all other hydrodynamic variables, namely the density ρ, viscosity η, chemical potential μ, pressure p, and velocity $\mathbf{v}$, vary smoothly across the interface.

In equilibrium, the configuration of the system is determined by the Helmholtz free-energy functional [103,104]

$$\mathcal{F} = \int_V \left(F_\mathrm{b} + \frac{\kappa}{2} |\boldsymbol{\nabla}\phi|^2 \right) \mathrm{d}V + \int_S (h\phi_\mathrm{s}) \mathrm{d}S, \tag{2.37}$$

where V is the total volume of the binary fluid and S is the surface of the confining solid walls. The first term in the volume integral corresponds to the bulk free-energy density

$$F_\mathrm{b} = \frac{\rho}{3} \log \rho + \frac{a}{2}\phi^2 + \frac{b}{4}\phi^4, \tag{2.38}$$

which contains an ideal gas term to ensure incompressibility, and a double-well potential where a and b are model parameters. With this choice of F_b, phase separation occurs if $a < 0$ and $b > 0$ leading to the formation of two equilibrium phases where $\phi_\mathrm{b} = \pm\sqrt{-a/b}$. Here we fix $b = -a$ and take $\phi_\mathrm{b} = -1$ to be the gas phase and $\phi_\mathrm{b} = +1$ to represent the liquid.

The square-gradient term in equation (2.37) represents the energy cost of spatial variations of ϕ across the system. In equilibrium, it leads to the formation of a diffuse interface of width $\xi = \sqrt{-2\kappa/a}$ and surface tension $\gamma = \sqrt{-8\kappa a/9}$.

The surface integral in equation (2.37) models the wetting properties of the binary fluid, where ϕ_s represents the value of the phase field at the solid surfaces. In equilibrium, this term leads to the boundary condition

$$\partial_n \phi_\mathrm{s} = -\frac{h}{\kappa}, \tag{2.39}$$

where n indicates the coordinate normal to the solid surface. The parameter h can be tuned to control the contact angle of the fluid-fluid interface with the solid, θ_{e}, through the relation

$$\cos\theta_{\mathrm{e}} = \frac{(1+\Omega)^{3/2} - (1-\Omega)^{3/2}}{2}, \tag{2.40}$$

where $\Omega = h\sqrt{2/\kappa a}$.

The Cahn-Hilliard approach can be used to model a phase change by introducing an imbalance in the chemical potential of the binary fluid, defined as

$$\mu \equiv \frac{\delta\mathcal{F}}{\delta\phi} = a\phi + b\phi^3 - \kappa\nabla^2\phi. \tag{2.41}$$

An inhomogeneity in the chemical potential of local amplitude $\boldsymbol{\nabla}\mu$ will give rise to a diffusive flux, leading to the growth or depletion of the bulk phases[105]. To model the diffusive flux, we use the constitutive equation

$$\mathbf{j} = -M\boldsymbol{\nabla}\mu, \tag{2.42}$$

where M, called the mobility, plays the role of a diffusion constant. Imposing local conservation of the phase field ϕ leads to the convection-diffusion equation

$$\frac{\partial\phi}{\partial t} + \mathbf{v}\cdot\boldsymbol{\nabla}\phi = M\nabla^2\mu. \tag{2.43}$$

Apart from diffusive transport of the phase field, inhomogeneities in the chemical potential give rise to a force per unit volume $-\phi\boldsymbol{\nabla}\mu$ acting on the fluid[106]. This term amounts to capillary stresses originating from distortions of the interface, and gives rise to the Laplace pressure of a curved interface in the sharp-interface limit. Therefore, the mass and momentum balance equations are

$$\frac{\partial\rho}{\partial t} + \boldsymbol{\nabla}\cdot(\rho\mathbf{v}) = 0, \tag{2.44}$$

and

$$\rho\left(\frac{\partial \mathbf{v}}{\partial t}+\mathbf{v}\cdot\boldsymbol{\nabla}\mathbf{v}\right)=-\boldsymbol{\nabla}p+\boldsymbol{\nabla}\cdot(\eta(\boldsymbol{\nabla}\mathbf{v}+\boldsymbol{\nabla}\mathbf{v}^{\mathrm{T}}))-\phi\boldsymbol{\nabla}\mu. \tag{2.45}$$

An important aspect of the diffuse-interface approach is the ability to model contact-line dynamics. In sharp-interface approximations, imposing the no-slip boundary condition at the contact line leads to a diverging viscous stress[107], commonly known as the Huh-Scriven paradox[108]. To regularise the diverging viscous stress one needs to introduce a mechanism that allows the contact line to move. A widespread approach is to replace the no-slip boundary condition by the so-called Navier slip boundary condition, where the tangential velocity to the wall is set according to $v_{\mathrm{s}}=-l_{\mathrm{s}}\partial_n v_s$. This introduces the slip length l_{s}, as an additional length scale in the problem, encoding the microscopic physics that lead to the observed macroscopic slip. As a consequence, the dynamics of the contact line becomes dependent on the ratio of the slip length to the characteristic macroscopic length scale of the flow. In the Cahn-Hilliard model, contact-line slip arises by virtue of mass diffusion over a characteristic length scale $l_{\mathrm{D}}=\sqrt{M\eta}$[109]. The emergent slip length is set by l_{D} and shows the limiting scalings $l_{\mathrm{s}}\sim\sqrt{l_{\mathrm{D}}\xi}$[110] for $l_{\mathrm{D}}\ll\xi$ and $l_{\mathrm{s}}\sim l_{\mathrm{D}}$[109,111] for $l_{\mathrm{D}}\gg\xi$ with a cross over between the two regimes occurring at $l_{\mathrm{D}}/\xi\approx 0.4$[112]. Therefore, the contact-line slip can be controlled in the Cahn-Hilliard model by choosing l_{D}.

2.3.1 Numerical implementation

The binary fluid model described in the previous section can be solved using an extension of the original LB algorithm described in Sec. 2.2. Since there is an additional field ϕ we need to introduce an additional set of distribution functions g_i which evolve according to

$$g_i(x+v_i,t+1)-g_i(x,t)+F_i=\frac{1}{\tau_g}(g_{ie}(x,t)-g_i(x,t)). \tag{2.46}$$

Their sum defines the macroscopic ϕ field

$$\sum_i g_i = \phi. \tag{2.47}$$

We also have constraints on the moments of the g_{ie}

$$\begin{gathered} \sum_i g_{ie} = \phi, \\ \sum_i g_{ie}(u_{i\alpha} - v_{i\alpha})(u_{i\beta} - v_{i\beta}) = n\hat{M}\mu\delta_{\alpha\beta}. \end{gathered} \tag{2.48}$$

The additional relaxation time τ_g and $\hat{M}$ are related to the diffusivity M by

$$M = \frac{\tau_g - 1}{2}\hat{M}. \tag{2.49}$$

CHAPTER 3

Modeling evaporation

In this chapter we show how it is possible to model evaporation in the Cahn-Hilliard model. The implementation of evaporation in this model was first presented in Ref.[105]. Here we review the theoretical foundations and the numerical implementation of evaporation in the Cahn-Hilliard model using the multiphase Lattice Boltzmann algorithm presented in the previous chapter. We also present simulation results for evaporation in simple systems.

3.1 Evaporation in the Cahn-Hilliard model

The Cahn-Hilliard model allows us to model evaporation and condensation phenomena. Let us consider Eq. 2.43; if convection is negligible and the diffusion timescale is small compared to the evaporation timescale we are left with

$$\nabla^2 \mu = 0 \tag{3.1}$$

which is the same equation as Eq. 1.8 that we have used to describe evaporation, with the only difference being the presence of the chemical potential instead of the concentration field. We have seen in Chapter 1 that evaporation or condensation happens if the concentration of one fluid is different from its equilibrium value; from a thermodynamic point of view the same effect can arise if the chemical potential of one phase is out of equilibrium. This observation has been used in Ref.[105] to show that it is possible to induce the evaporation of one phase by fixing the value of μ to a non-equilibrium value.

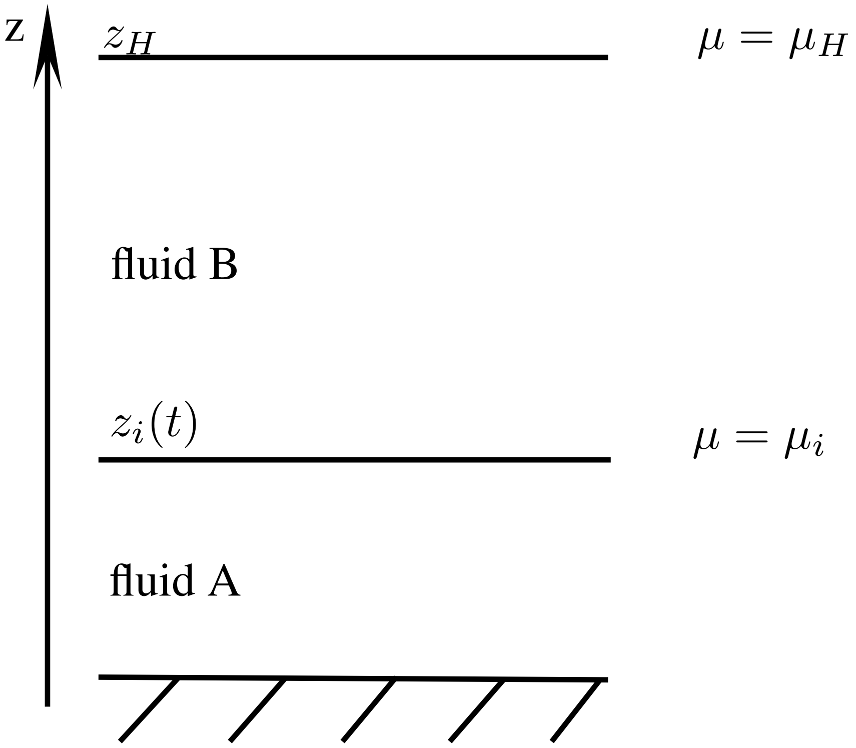

Figure 3.1: Sketch of a 1D film of fluid subject to evaporation. Description of the system is in the text.

Let us consider a one dimensional liquid film as shown in Fig. 3.1. Let us indicate with $z_i(t)$ the position of the fluid interface at time t, and with $z_0 = z(t = t_0)$. If we fix the chemical potential at the top of the system ($z = z_H$) to a value $\mu_H \neq \mu_{eq}$ (or equivalently we can fix ϕ to a value $\phi_H \neq \phi_{eq}$), the liquid interface will move. Let us assume that the ϕ field has a travelling wave form $\phi = \phi(z - vt)$ with v being the propagation velocity. We can then rewrite Eq. 2.43 (in the limit of negligible convection) as

$$-v\frac{d\phi}{dz} = M\frac{d^2\mu}{dz^2}. \tag{3.2}$$

Integrating the last equation across the interface over an interval $[-\delta z, \delta z]$ we have

$$-v[\phi(\delta z) - \phi(-\delta z)] = M \left(\left.\frac{d\mu}{dz}\right|_{\delta z} - \left.\frac{d\mu}{dz}\right|_{-\delta z} \right). \tag{3.3}$$

Since the chemical potential is fixed only on the top of the system the term $d\mu/dz|_{-\delta z}$ is zero because the fluid's interface is in local equilibrium at $-\delta z$. This leads to

$$v = \frac{M}{\Delta\phi} \left.\frac{d\mu}{dz}\right|_{\delta z} \tag{3.4}$$

where $\Delta\phi = \phi(-\delta z) - \phi(\delta z)$. This equation determines the velocity of the film interface once the chemical potential profile is known. In order to calculate the latter let us use Eq. 3.1; in this system it reduces to

$$\frac{d^2\mu}{dz^2} = 0 \tag{3.5}$$

which can be easily solved given the two boundary conditions $\mu = \mu_H$ at $z = z_H$ and $\mu = \mu_i$ at $z = z_i(t)$. The chemical potential profile is then

$$\mu(z) = \mu_H + \frac{\mu_H - \mu_i}{z_H - z_i(t)}(z - z_i(t)) \tag{3.6}$$

where μ_i is the value of the chemical potential at the interface. We can insert this equation in Eq. 3.4 to get the velocity of the interface; with an integration we get the temporal evolution of the interface position

$$z_i(t) = z_H - \left((z_H - z_0)^2 - M(\mu_H - \mu_i)t\right)^{1/2} \tag{3.7}$$

which has the typical "D^2 law" dependence of diffusion-limited evaporation. This derivation proves that is possible to model evaporation in the Cahn-Hilliard model and it also gives a recipe to implement it in LB simulations.

3.2 Evaporation of 1D films

We have seen in the previous section how it is possible to model evaporation within the Cahn-Hilliard model. The implementation of evaporation with a LB algorithm has been first presented in[105], using Ludwig[113], a LB code for complex fluids. Here we review the main results.

We simulated the 1D system described in the previous section and illustrated in Fig. 3.1. The system dimensions were $(N_x, N_y, N_z) = (1, 1, 150)$ in lattice units. Periodic boundary conditions were applied in the x and y directions with a wall located at $z = 1$. The initial height of the film was $z_0 = 100$. The model parameters used are listed in Table 3.1.

ρ	τ	τ_g	a	b	κ	M
1	1	1	-0.00305	0.00305	0.0078	5

Table 3.1: LB simulation parameters.

In relation to Fig. 3.1 we refer to the fluid A(B) as the one with $\phi_b = +1(-1)$. We fixed the order parameter at the top of the simulation domain to the values $\phi_H = -1.1, -1.2, -1.3, -1.4, -1.5$; since we are in the bulk phase this is equivalent to fixing the chemical potential to a value $\mu_H = a\phi_H + b\phi_H^3$. The results of the simulations are shown in Fig. 3.2.

The plot shows that for small departures from equilibrium the LB algorithm is in perfect agreement with the theoretical analysis. However the agreement deteriorates as the value of ϕ_H get farther away from the equilibrium value. This behaviour is due to the fact that the farther the system is from equilibrium, the bigger the diffusion timescale becomes, thus invalidating the assumption used in the theory of a diffusion timescale much smaller than the evaporation timescale.

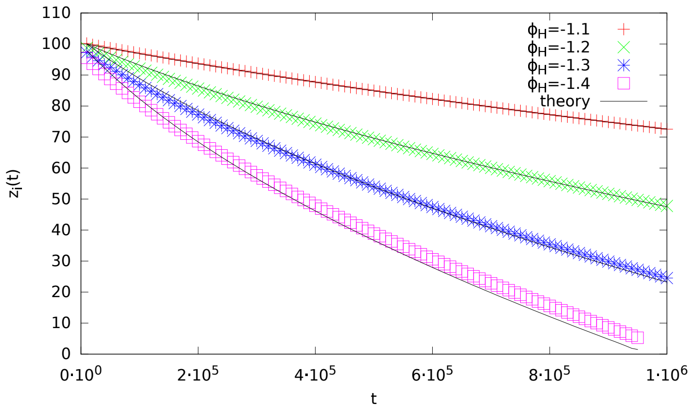

Figure 3.2: LB simulations of the evaporation of a 1D film. Time and interface position are in simulation units. The coloured points are simulation results, the black lines are theoretical predictions from Eq. 3.7.

3.3 Evaporation of two and three dimensional droplets

The theoretical analysis carried out in Sec. 3.1 can be extended in two and three dimensions. Analytical results can be obtained for a spherical drop sitting on a surface with the ϕ field fixed on a hemispherical shell over the drop as sketched in Fig. 3.3 (a) (we will denote this as shell BC).

shell B.C
(a)

top B.C.
(b)

Figure 3.3: Sketch of different boundary conditions used to implement evaporation in two and three dimensions. The dashed lines indicate where ϕ is fixed to a non-equilibrium value.

If we have a two-dimensional droplet with radius R, a contact angle of $\theta_e = 90°$, and ϕ is fixed on a hemispherical shell of radius R_H, we can calculate the rate of change of the droplet area $A = \pi R^2/2$. The calculation is the same as the 1D case and it leads to

$$\frac{dA}{dt} = \frac{\pi M}{\Delta\phi}\frac{\mu_H - \mu_i}{\ln(R_H/R)}. \tag{3.8}$$

For a three-dimensional droplet with volume $V = 2\pi R^3/3$ and the other parameters as in the 2D case we have instead

$$\frac{dV}{dt} = \frac{2\pi M}{\Delta\phi}\frac{(\mu_H - \mu_i)R}{1 - R/R_H}. \tag{3.9}$$

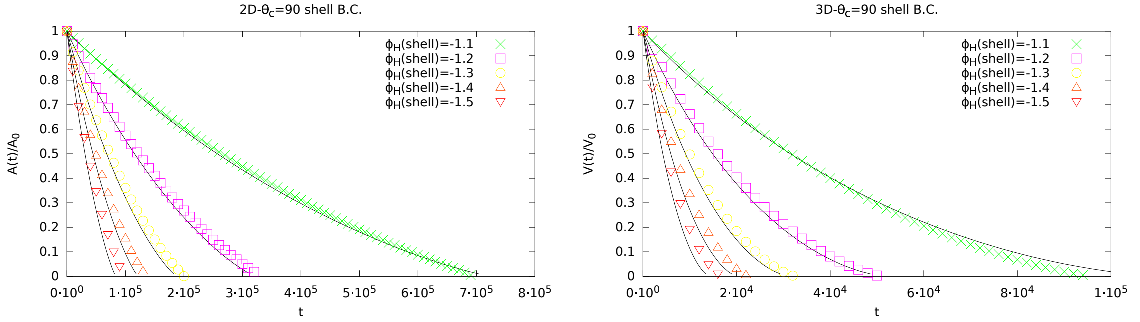

Figure 3.4: Time evolution of evaporating droplets in two (left) and three (right) dimensions subject to shell BC. Black lines are the theoretical predictions.

It is worth noting this equation is the same as Eq. 1.17, although there is an additional term $1 - R/R_H$ because the ϕ field is fixed at a finite distance R_H from the drop. However this term tends to one as $R_H \to \infty$ thus restoring the result of Eq. 1.17 (which is obtained by fixing the concentration at infinity).

Fig. 3.4 shows results of simulations of two and three dimensional droplets with shell BC. The parameters used are listed in Table 3.1. For the 2D droplet a system of size $(N_x, N_y, N_z) = (200, 1, 100)$ and a droplet initial radius $R_0 = 50$ were used. For the 3d droplet a system of size $(N_x, N_y, N_z) = (100, 100, 50)$ and a droplet initial radius $R_0 = 30$ were used. The order parameter ϕ was fixed on a shell of radius $R_H = 98$ in the 2D case and $R_H = 48$ in the 3d case. As for the 1D simulations the agreement with theory is excellent for values of ϕ_H near to equilibrium values and it deteriorates for larger values of ϕ_H.

The shell BC illustrated in Fig. 3.3 can model the evaporation of an isolated drop; other boundary conditions can be implemented to model different physical situations. For example Fig. 3.3 (b) shows a configuration that we will refer to as top BC; if periodic boundary conditions are applied on the sides of such a system, the resulting

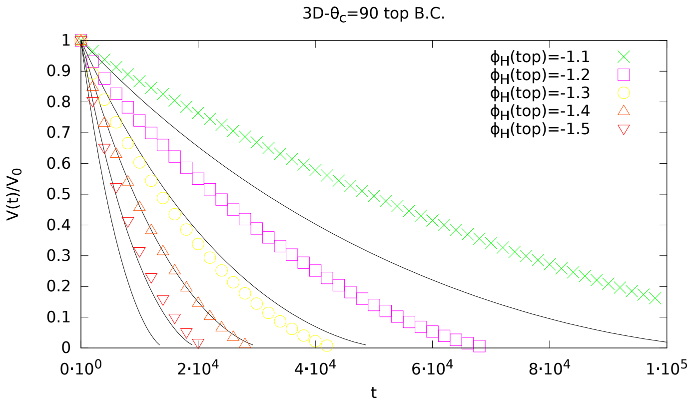

Figure 3.5: Time evolution of 3d droplets with top BC. Black lines are theoretical predictions for shell BC.

configuration can model an infinite array of droplets evaporating together. Fig. 3.5 shows simulations of 3d droplet evaporation with top BC.

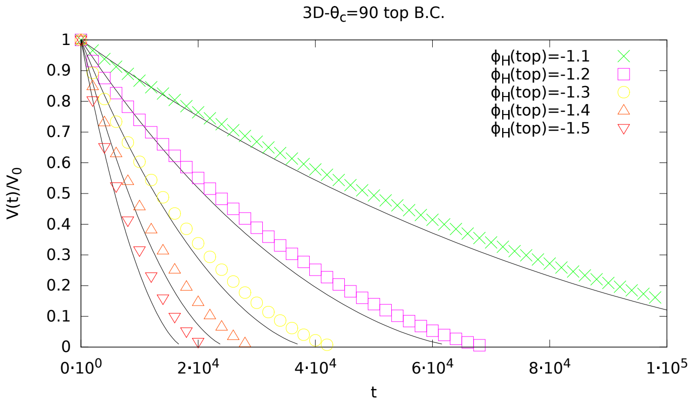

Figure 3.6: Time evolution of droplets with top boundary conditions. Now the black lines are the theory predictions with the correction of Eq. 3.10.

The results show that with this different choice of boundary conditions the evaporation is slower compared to the theoretical prediction for an isolated droplet. This result makes sense from a physical point of view because the presence of other droplets slows down the evaporation because of higher vapour concentration (this behaviour is discussed in detail in the next chapter).

For a generic choice of boundary conditions it is not possible to derive an analytical result for the evaporation rate. For top boundary conditions however we can get an approximate prediction for the evaporation rate. As explained in Chapter 1, it is known that the calculation of the evaporation rate of a drop of a certain shape and subject to given boundary conditions is equivalent to the calculation of the electrostatic capacitance of a conductor of the same shape as the drop and subject to the same boundary conditions[14]. For the top BC and a hemispherical drop this means calculating the capacitance of a sphere of radius R distant L_z from a plane at a constant potential (we do not take into account the periodic boundary conditions used in the top BC configuration). Using the method of images, if $R \ll L_z$ one can approximate the image sphere with a point charge at a distance $2L_z$ from the sphere's centre. The capacitance of such a system is then

$$C = \frac{1}{\frac{1}{R} - \frac{1}{2L_z - R}}. \tag{3.10}$$

Fig. 3.6 shows the comparison between the simulation results and the prediction of evaporation rate derived from Eq. 3.10. Although Eq. 3.10 has no pretence of rigour in its derivation, it still has a fairly good predictive power. Other boundary conditions are introduced in the next three chapters for the study of different problems. Throughout all the thesis a a contact angle of $\theta_e = 90°$ is used and evaporation is always in constant contact angle (CA) mode.

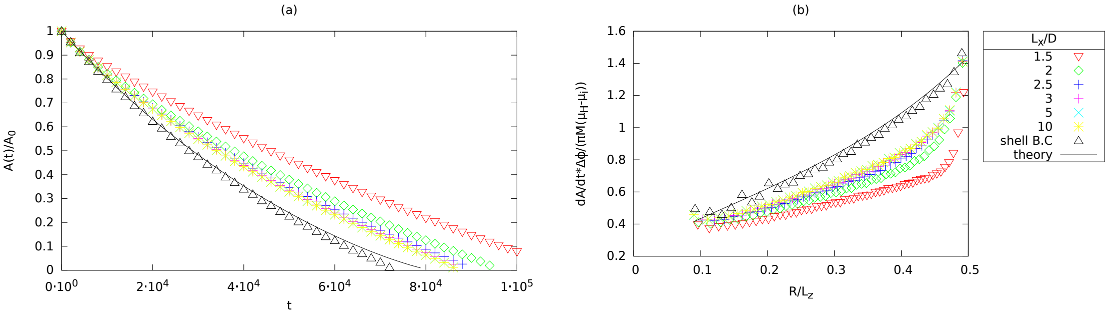

Figure 3.7: Temporal evolution of a 2D evaporating drop for different values of L_x. The black line is the theoretical prediction for the evaporation of an isolated drop. The data indicated as "shell" refer to a simulation of the same drop with shell B.C. (a) is the temporal evolution of the droplet area, (b) is the normalised evaporation rate.

3.4 Effect of boundary conditions

As shown in the previous section, the evaporation rate of a droplet is strongly dependent on the boundary condition used. However, as already shown for the shell BC, if the size of the drop is much smaller than the simulation box size, we recover the evaporation rate of a single drop which is independent of the details of the simulation configuration. For example, by using the top B.C. with larger and larger simulation boxes, one expects

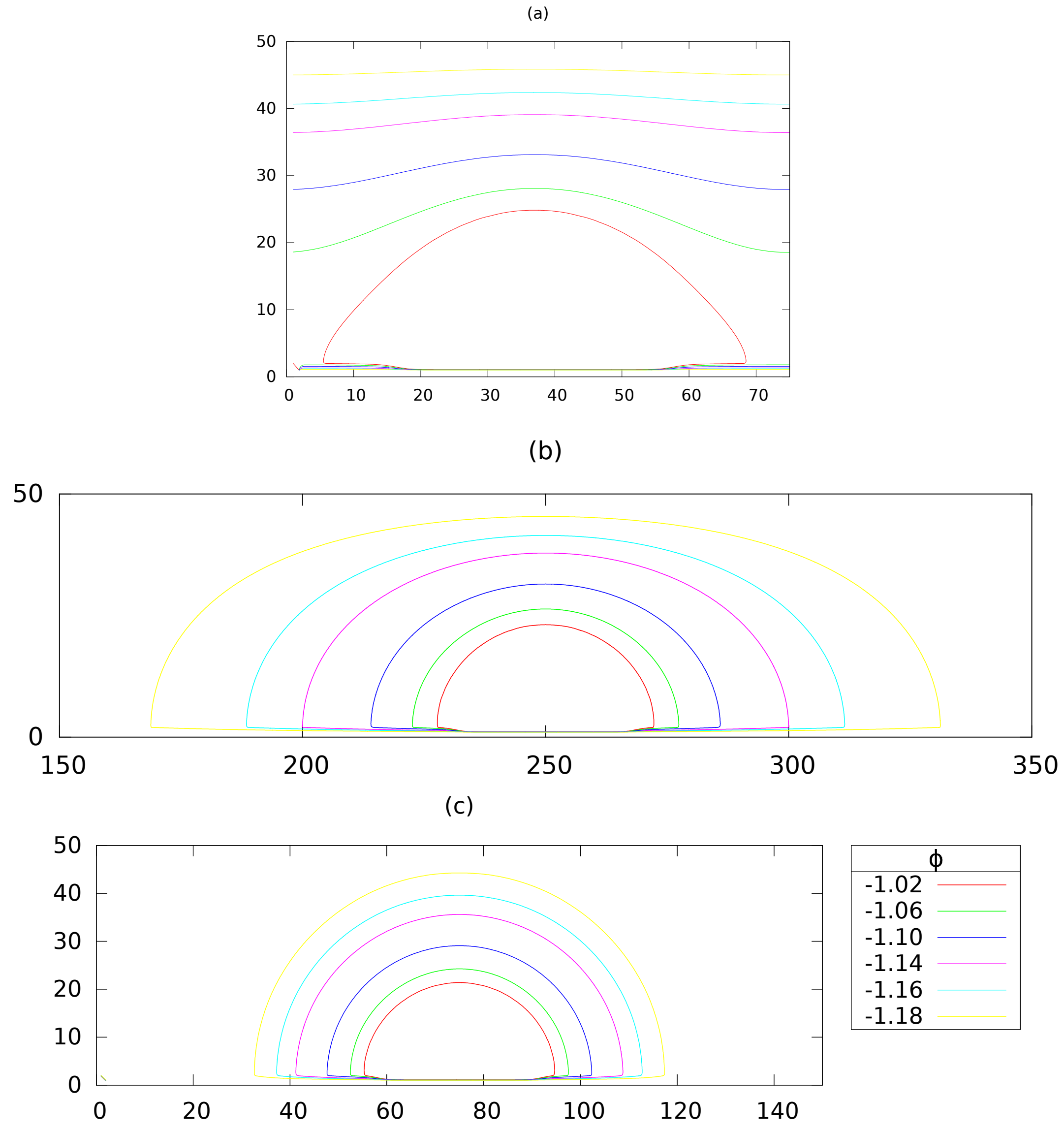

Figure 3.8: Contour curves of the order parameter of a 2D evaporating drop for different box sizes $L_x = 1.5D$(a), $10D$(b), shell B.C(c), where $D = 50$ is the initial footprint diameter of the drop. The data are taken after $4 \cdot 10^4$ timesteps.

to approach the limit of an isolated evaporating drop. To test this hypothesis we have simulated a 2D drop of fixed size in simulation boxes of different sizes. We kept L_z constant and we have varied L_x. The contact angle was fixed at $\theta_c = 90\,°$; the initial radius of the drop was $R_0 = 25$ and $L_z = 2R_0$ (unless otherwise stated). We measured L_x in terms of the initial footprint diameter of the droplet D. The temporal evolution of the drop area for different box sizes is shown in Fig. 3.7-(a).

The results confirm that by increasing the simulation box size compared the droplet size, the drop evaporation rate converges to the value predicted for an isolated drop. This result is more evident if one looks at the normalised evaporation rate, shown in Fig. 3.7-(b). The evaporation rate has been normalised using Eq. 3.8. The convergence towards the isolated drop behaviour can be explained by looking at the contour curves of the order parameter in Fig. 3.8. If $L_x \approx D$ the gradient in the order parameter is almost only in the vertical direction, while if $L_x \gg D$ the order parameter profile is more similar to the single drop case. This makes sense from a physical point of view, because the configuration with $L_x \approx D$ corresponds to an array of densely packed droplets. In this case we expect the concentration gradient to be almost only in the vertical direction, as observed in the simulations, because the space between the droplets will have a high vapour concentration. For the case $L_x \gg D$, we expect the single droplet behaviour instead.

We have also investigated the effects of drop spacings in the 3d case. In Fig. 3.9 the evaporation rate for 3d drops is plotted for different values of L_x while keeping L_z fixed. It can be seen that also in this case, as L_x grows, the simulation curves converges to the theoretical one for an isolated droplet. For large values of R/L_z the simulation results depart from the theoretical curve because we use the expected evaporation rate for the shell BC in the case of an infinitely distant boundary shell, while in the simulations the boundary where the chemical potential is fixed is at a finite distance.

We have also analyzed the effect of the distance of the drop from the top wall. The results are in Fig. 3.10. Also in this case there is convergence toward the single droplet case. It should be noted that also during each simulations the numerical results

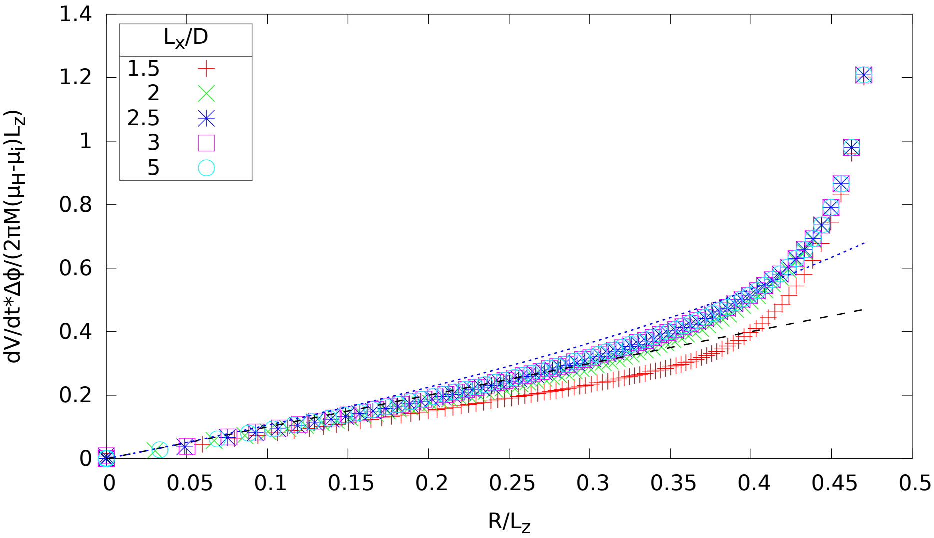

Figure 3.9: Evaporation rate of 3d drops with top BC and different drop spacing. In all the simulations $R_0 = L_z/2$. The blue dashed line is the theory curve relative to Eq. 3.10. The black dashed line is the expected evaporation rate for the shell BC in the case of an infinitely distant boundary shell.

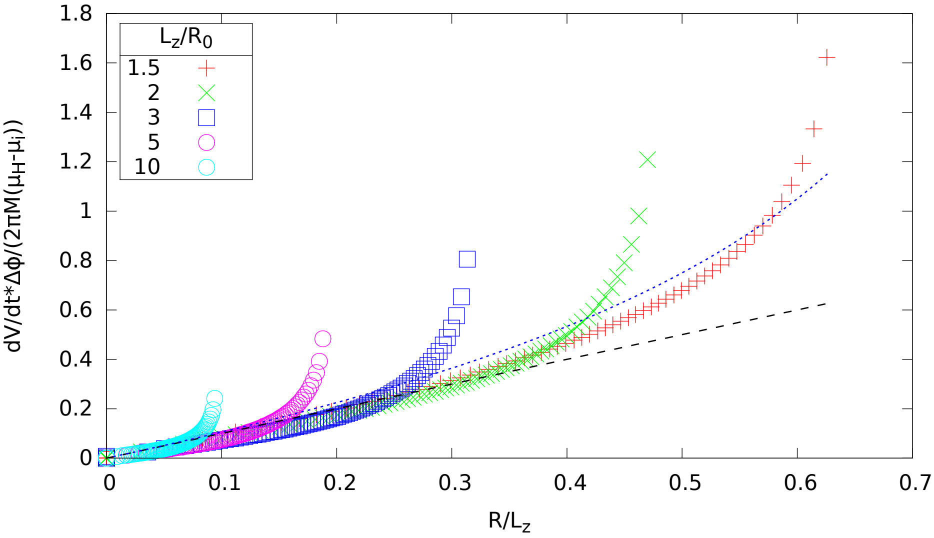

Figure 3.10: Evaporation rate of 3d drops with top BC and different ratio R_0/L_z . In all the simulations $2R_0 = L_x = L_y$. The blue dashed line is the theory curve relative to Eq. 3.10. The black dashed line is the expected evaporation rate for the shell BC in the case of an infinitely distant boundary shell.

converge towards the single droplet case as the drop gets smaller. This is consistent with the fact that as long as the linear dimensions of the simulation system are much bigger than the droplet size $L \gg R$, the evaporation rate tends to the theoretical value of an isolated drop.

CHAPTER 4

Collective effects in droplet evaporation

The effect of neighboring droplets on the dissolution of a sessile droplet, i.e. collective effects, are investigated numerically and compared to experimental results obtained by Erik Dietrich and co-workers[1]. On the experimental side small, 20 nL approximately, mono-disperse surface droplets arranged in an ordered pattern were dissolved and their size evolution was studied optically. The droplet dissolution time was studied for various droplet patterns. On the numerical side, Lattice-Boltzmann simulations were performed. Both simulations and experiments show that the dissolution time of a droplet placed in the center of a pattern can increase by as much as 60% as compared to a single, isolated droplet, due to the shielding effect of the neighboring droplets. However, the experiments also show that neighboring droplets enhance the buoyancy driven convective flow of the bulk, increasing the mass exchange and counteracting collective effects. This enhanced convection can reduce the dissolution time of droplets at the edges of the pattern to values below that of a single, isolated droplet.

4.1 Introduction

The evaporation or dissolution of a single surface droplet is a well-studied topic due to its high importance in various applications, for example in the field of coating, and the deposition of particles[15,16,114]. Even more relevant but far less studied is the evaporation or dissolution of surface droplets surrounded by other droplets. This situation for example occurs whenever a spray is applied to a surface, or in inkjet printing. The presence of neighboring droplets makes the analytical approach more challenging compared to a single droplet, and in general no analytical solution for the collective dissolution problem, on which we will focus here, exists. The addition of neighbouring droplets, like in the pattern sketched in Fig. 4.1, is expected to change the concentration gradient by saturating the water in between the droplets, which in turn leads to a decrease in the mass loss rate.

The mutual effect that neighboring droplets have on one another, referred to as the 'collective effect', has been studied in detail for spherical droplets inside sprays[115–118], due to its importance in, for example, spray cooling and fuel vaporization. In contrast to this, collective effects in the context of surface droplets are as of yet relatively unexplored. Available work describes one-dimensional diffusion above an infinitely dense packed pattern where the effect of individual droplets is irrelevant[119,120], or the collective effects are believed to be originated by the delayed dissolution of polydisperse, randomly placed droplets. Only very recently, a first step was taken by Carrier et al[121] to assess the effect of a finite sized pattern of dissolving droplets, and compare the experimental results to a theoretical model. The latter work focussed on evaporation from an ordered pattern of ten droplets, or a random pattern of many polydisperse droplets. Moreover, an approximation was derived for the reduction in evaporating flux, based on the number and number density of the droplets, predicting reductions in the order of tens of percent.

In this chapter, we further investigate the collective effect in patterns of dissolving surface droplets. The diffuse interface numerical scheme described in Chapter 2 is used to simulate this system, and the numerical results are compared to experiments. Simulations and experiments on single droplets, finite, and infinite patterns are compared. In particular, we will discuss the competition between, on the one hand, the slowed dissolution due to the enhanced surrounding concentration thanks to the neighboring droplets, and, on the other hand, enhanced dissolution due to convective effects.

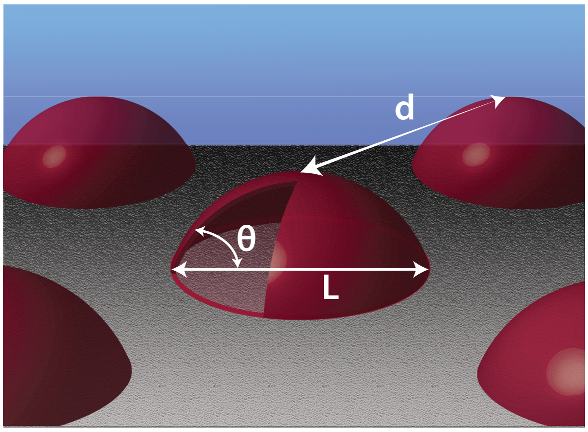

Figure 4.1: Schematic drawing of a pattern of surface droplets with footprint diameter L and contact angle θ, placed in a hexagonal pattern with center-to-center distances d.

4.2 Methods

4.2.1 Experimental procedure

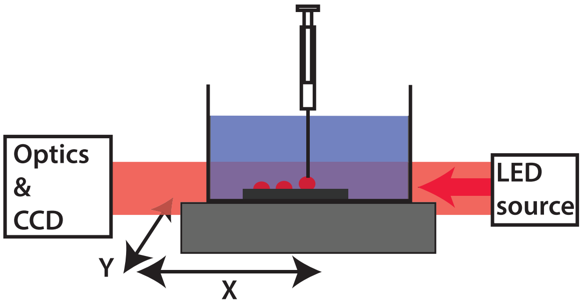

Figure 4.2: Sketch (not to scale) of the experimental setup, showing the glass tank with the substrate placed under water. The syringe is connected to a syringe pump (not drawn) to dispense droplets of 1-heptanol. Using the X-Y translation stage, the tank is moved with respect to the syringe. A LED illuminates the middle droplet of the pattern, and projects the side view image of this droplet onto a long-distance microscope and CCD-camera.

Disclaimer: the experimental work described in this chapter was performed by Erik Dietrich and collaborators.

The experimental setup is sketched in Fig. 4.2. Droplets of 1-heptanol, a long-chain alcohol, were placed through a syringe on top of a hydrophobized silicon wafer. Details of the experimental procedure are give in Ref.[1]. Droplets were placed in a hexagonal arrangement, as sketched in Fig. 4.1, with the exception of the outermost droplets in the largest pattern. The patterns were formed by $n = 5, 19, 41$, or 127 droplets as shown in Figs. 4.3 A-D. The dissolution of the central droplet in each matrix was then recorded with a CCD camera.

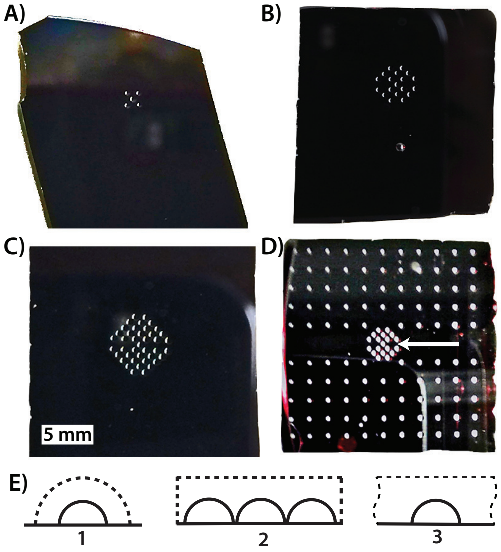

Figure 4.3: A-D: Top view photographs of the water-immersed silicon substrate with the droplet patterns. The photographs show patterns with 5 (A), 19 (B), 41 (C), and 127 (D) 20 nL sized droplets of 1-heptanol. Panel E is a schematic side view of the numerical set-up showing the shell (E1), side (E2), top (E3) boundary condition used to simulate a single drop, multiple drops and an infinite array of drops respectively. The dashed lines in E indicate the surfaces, where the chemical potential is fixed at a non-equilibrium value to drive dissolution. The wavy dashed lines in Fig. (E3) represent periodic boundary conditions.

4.2.2 Numerical procedure

We performed three-dimensional simulations of evaporation using the techniques described in Chapters 2 and 3. The droplet-bulk system is considered as a binary liquid and by setting the chemical potential of the model at a value away from equilibrium, one phase is favored over the other. This physically corresponds to the situation that dissolution takes place if the solute concentration is lower than its saturation value (which is the equilibrium value). Three-dimensional surface droplets were simulated.

We adopted the following boundary conditions (see Fig. 4.3E):

1. For a single droplet, we use the shell BC described in Chapter 3;
2. For a finite pattern of droplets, the chemical potential is fixed at the top and the sides of the computational domain ("side BC");
3. For an infinite pattern of droplets, we use the top BC described in Chapter 3.

4.3 Results

4.3.1 Single droplet

To provide a simple test case and a basis to compare further measurements, we start with the dissolution of a single surface droplet, which has been well described in the context of the analogous processes of dissolving bubbles or evaporating droplets. In the case of steady-state, diffusion-limited dissolution, the dissolution rate of a droplet is given by Eq. 1.17.

By inserting the values for a 1-heptanol droplet with initial volume $V_0 = 20$ nL, and numerical integration of Eq. 1.17, we obtain the black dashed line in Fig. 4.4 which represents the droplet volume as function of the time to dissolution $t - \tau$, where τ is the dissolution time: the time needed to completely dissolve the droplet.

Comparison of the experiments on single droplets of different initial volumes (plotted as the coloured solid lines in Fig. 4.4) to the diffusion-limited model of a single droplet reveals a considerable discrepancy: the experiments are characterized by a higher rate of mass loss and therefore shorter dissolution time τ for a given initial volume. It has been shown[8] that the increased mass transport is caused by a convective contribution to the dissolution process, driven by solute-induced density gradients in the bulk.

The experimental results from Fig. 4.4 will be used in the next section, as they allow us to account for the variation in the initial droplet volumes: Despite the fact that great care is taken to create equally sized droplets, small differences in the initial droplet volume cannot be avoided. To allow for easy comparison between experiments

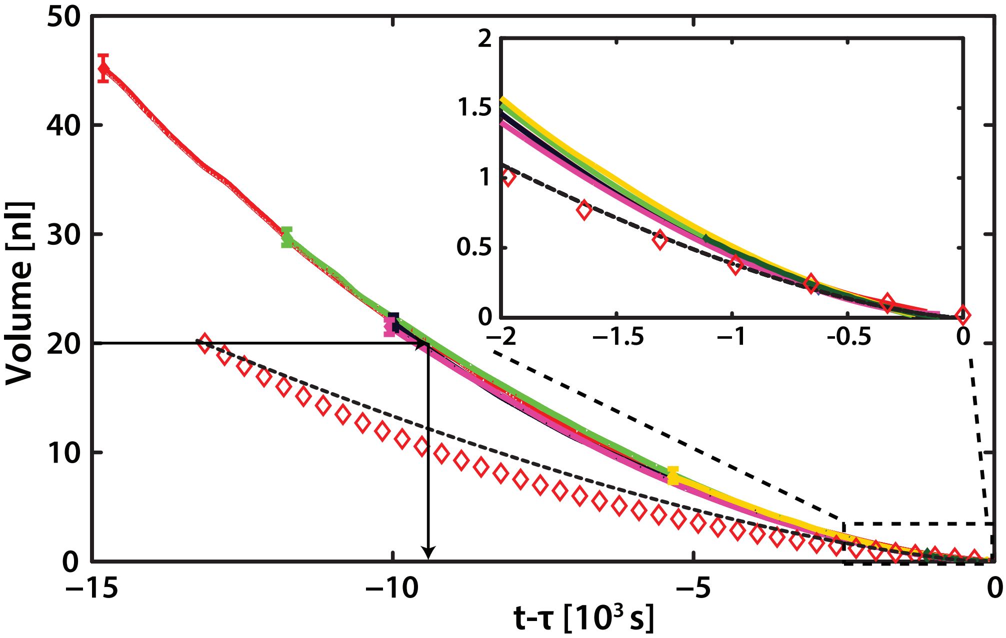

Figure 4.4: Volume of single dissolving droplets as function of time until dissolution $t - \tau$. The black dashed line represents the expected diffusion-limited dissolution of a 20 nL 1-heptanol droplet (Eq. 1.17), to which the (purely diffusive) simulations (plotted as the open red diamonds) are compared. The experiments on individual droplets of 1-heptanol and various initial volumes (solid lines of different colours) reveal an increased dissolution rate, due to a convective contribution to the dissolution[8]. We shift the x-axis by the droplet life time τ to overlap the individual measurements for comparison. The black arrows illustrate how the experiments can be used to find an empirical relation between the droplets initial volume and its dissolution time.

with slight variations in the initial droplet volume, we correct for these deviations and compare the droplet volume to the desired initial volume of the droplets in the experiments (20 nL), by correcting the droplet volume V in each experiment according to

$$\tilde{V} = \frac{V}{V_0} \times 20\text{nL}, \tag{4.1}$$

where $\tilde{V}$ is the corrected droplet volume (in nL), and V and V_0 are the volume and the initial volume of the droplet, respectively. The differences in the initial droplet volumes (even though only a few nL) significantly affect the total droplet dissolution time, thus obscuring the possible influence of collective effects. Therefore we must also correct the (dissolution) time based on the initial volume, which in diffusive problems is usually achieved by scaling with the appropriate time scale, namely the diffusive time scale $\tau_\mathrm{d} = R_0^2\rho/(\Delta c D)$, where R_0 is the initial droplet radius, and $\Delta c = c_s - c_\infty$. Scaling the time in such a way allows to compare purely diffusive droplet dissolution behavior, independent of the initial droplet size or the material[4,122]. Unfortunately, on the one hand, the diffusive time scale τ_d cannot be used in the current system as the mass transport is not purely diffusive. On the other hand, purely convective dissolution with the associated convective time scale[8]

$$\tau_c = \frac{4}{5a}\left(\frac{\nu\rho_\mathrm{d}^4 R_0^5}{g\beta_c \Delta c^5 D^3}\right)^{1/4}. \tag{4.2}$$

where β_c is the bulk expansion coefficient, g the acceleration of gravity, and a a prefactor of order 1. Eq. (4.2) was shown to hold when the Rayleigh number

$$\mathrm{Ra} \equiv \frac{g\beta_c \Delta c R^3}{\nu D} > 12. \tag{4.3}$$

The Rayleigh number expresses the ratio of the buoyant force to the damping force, and for the current 1-heptanol droplets with volumes ≤ 20 nL, we find $0.5 <\mathrm{Ra}< 35$. This indicates droplet dissolution with contributions to mass transport from both convection and diffusion. This does neither allow for the use of the purely convective model, nor the purely diffusive model. Instead, both diffusion and convection play a role in the dissolution process.

Therefore we exploit the single-droplet experiments to give an empirical relation between the initial volume of a single droplet and its dissolution time $\tau_\mathrm{single}(V_0)$. Using this relation, we correct time in each experiment according to

$$\tilde{t} = \frac{t}{\tau_\mathrm{single}(V_0)} \times 9100\ \mathrm{s}, \tag{4.4}$$

where $\tilde{t}$ is the corrected time (in seconds), and $\tau_\mathrm{single}(V_0)$ is the dissolution time of a single, isolated droplet, based on the droplets' initial volume $16\ \mathrm{nL} \leq V_0 \leq 24$ nL. $\tau_\mathrm{single}(V_0)$ is obtained from the single-droplet experiments, as illustrated by the black arrows in Fig. 4.4 for the case where $V_0 = 20$ nL. In Eq. (4.4), 9100 s represents the dissolution time of a single, isolated droplet with an initial volume of 20 nL, which is the desired initial droplet volume [1].

To obtain a reference time scale for the simulations we map the simulation units to physical units by fixing the initial drop volume to 20 nL and then choose a time scale by matching the diffusive dissolution time scale $\pi LD(c_s - c_\infty)/2\rho_d$, the coefficient in Eq. (1.17), to its physical value. This corresponds to a dissolution time for a single drop of 13125 seconds. The scaled simulation results are shown as diamonds in Fig. 4.4. The details of these simulations have been discussed in Sec. 3.2.

The use of a time scale in seconds, rather than a dimensionless time is preferred as it emphasizes that the simulations and experiments are subject to different physical processes: purely diffusive dissolution in the simulations versus a combination of diffusive and convective dissolution in the experiments. Therefore this comparison must be interpreted as qualitative, and not quantitative. The absence of convection in the simulations is due to the fact that the two phases have equal densities, so no buoyancy is present. The effect of buoyancy forces is analysed in Chapter 6.

4.3.2 Droplet patterns: shielding mechanism

It has been proposed[120] that the enhanced dissolution time for collective droplets is caused by a larger solute concentration in the (liquid) environment in between the droplets, due to their dissolving neighbors, thus reducing the concentration gradient and thus the mass transport. We confirm this by simulating a pattern with $n = 5$ droplets, and measuring the concentration along a diagonal cross-section through this pattern as shown in Figs. 4.5A and 4.5B. The solid coloured lines, shown in panel A, represent five iso-concentration lines measured at $t_1 = 1900$ s along the cross-section indicated by the dashed line in Fig. 4.5B. They illustrate how the middle droplet primarily responds to a concentration gradient in the vertical direction, whereas the droplets at the perimeter

---

[1] Note that one cannot simply wait for a droplet with $V_0 > 20$ nL to dissolve down to $V = 20$ nL, as this would result in different waiting times, and with that in variations of the volumes of the neighboring droplets.

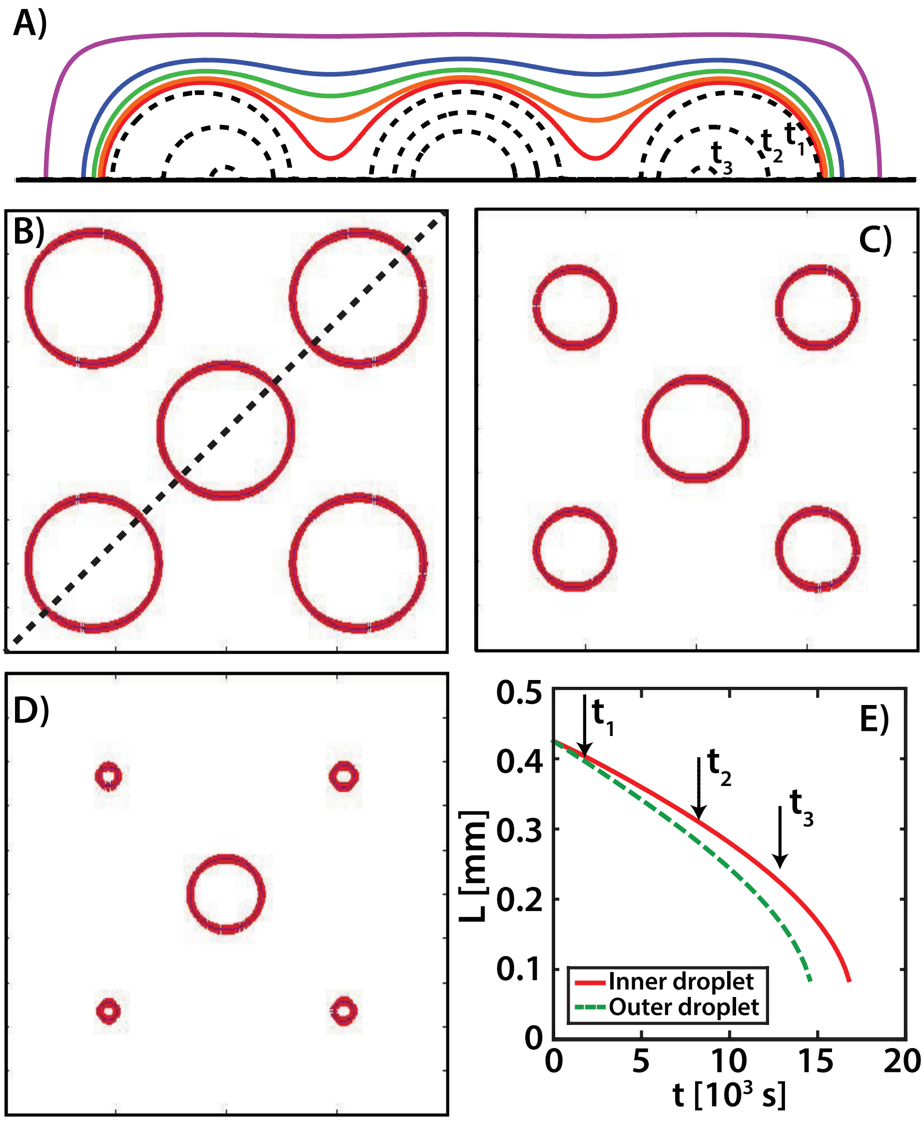

Figure 4.5: A) The iso-concentration profiles (coloured lines, measured at $t_1 = 1900$ s) show how the concentration in between the droplets is increased due to the neighboring droplets. The profile is measured diagonally through a pattern with $n = 5$ droplets, as indicated by the dashed line in panel B. The (dashed) contours of the droplets correspond to times $t_1 = 1900$ s (outermost contours), $t_2 = 8500$ s, and $t_3 = 13000$ s (innermost contours). Panels B-D show the droplet footprints at simulation times $t_1 = 1900$ s (B), $t_2 = 8500$ s (C), and $t_3 = 13200$ s (D). The footprint diameters L are plotted as function of time in (E); the evolution of L cannot be analysed for $L < 0.1$ due to the diffuse interface nature of the numerical model. The times at which panels B-D are taken are indicated by the black arrows in panel (E).

of the pattern also experience a gradient in the lateral directions. This should result in a reduced mass loss rate for the center droplet, as compared to the outer ones, and thus a relatively faster dissolution of the outer droplets. This is indeed the case, as shown by the droplet cross-sections (plotted at subsequent times $t_1 = 1900$ s, $t_2 = 8500$ s, and

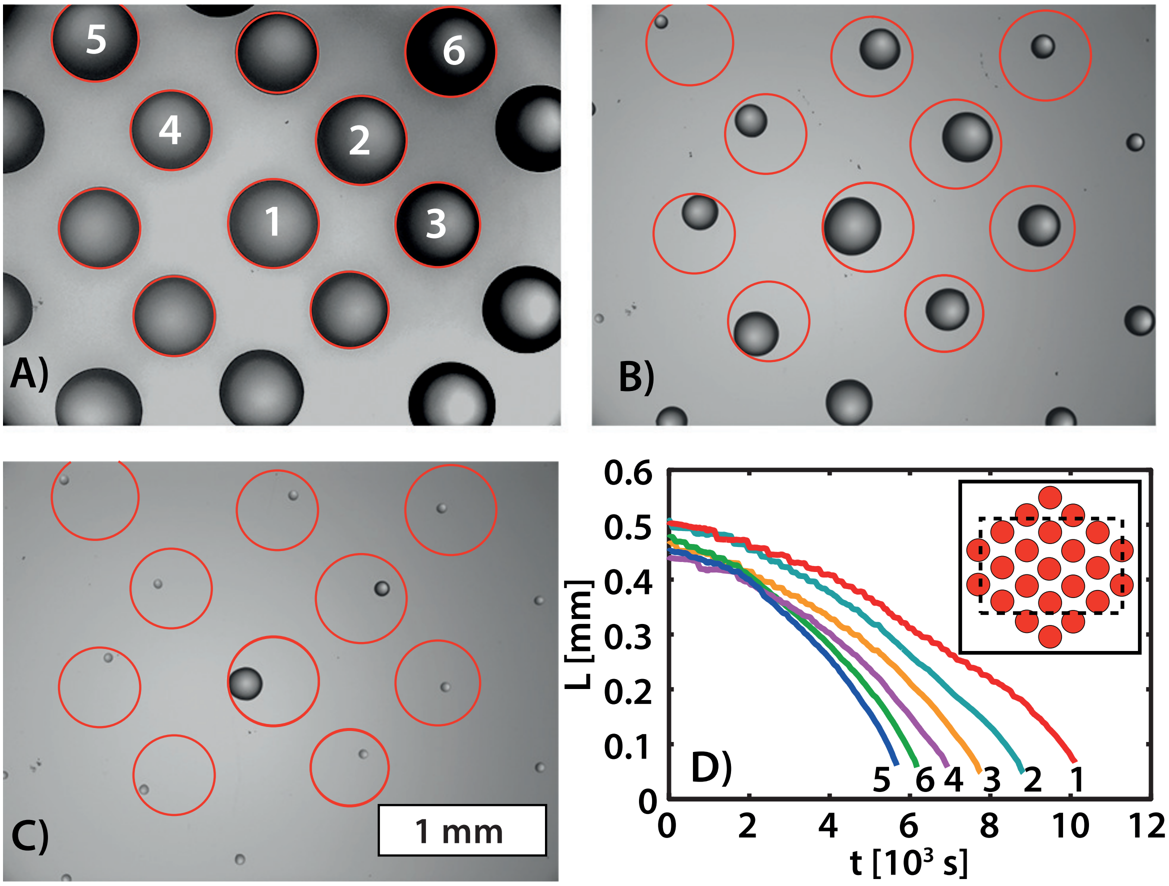

Figure 4.6: Top view of a 23-droplet pattern ≈ 2 minutes after deposition (A), after 120 minutes (B), and after 170 minutes (C). The inset in (D) shows the original droplet pattern, the dashed box indicates the field of view. In (D) the footprint diameter is plotted as function of time, showing that the outer most droplets dissolve more quickly than the inner ones, and even more quickly than a single droplet ($\tau_{\text{single}}(20\,\text{nL}) = 9100$ s). The red circles outline the droplets original footprint, revealing that the droplets are pinned by surface defects, as their centers of mass move during the dissolution. The correction scheme for volume and time as described in section 4.3.1 (Eqs. (4.1) and (4.4)) has not been applied here, in order to show the raw data.

$t_3 = 13200$ s by the black dashed lines in Fig. 4.5A), by the top view images of the droplets (panels B-D), as well as by the evolution of the droplet footprint diameters in time (panel E). The cross sections in panel A also show that in the absence of pinning, the outer droplets dissolve asymmetrically, due to the higher mass loss rate at their exposed sides, i.e. fully consistent with recent findings[123].

Comparable behavior is observed in experiments on patterns of droplets, as shown in Fig. 4.6. The droplets at the perimeter of the analyzed $n = 23$ pattern dissolve more quickly than the inner droplets. The outermost droplets (numbers 5 and 6) disappear first, followed by the droplets placed in the middle row (numbers 2, 3, and

4). The dissolution time of the center droplet (number 1) is extended by ≈ 20% as compared to an equally sized, single droplet. However, it is surprising to see that the dissolution times of the outermost droplets (5 and 6) are in fact much shorter ($\tau < 9100$ s) when compared to a single droplet. In absence of an accurate measurement of the droplet height, one should keep in mind that the shorter dissolution time of the outermost droplets (< 8000 s) cannot be explained by a smaller-than-expected initial volume, which has a minimum of $V_0 = 16$ nL, corresponding to $\tau_{\text{single}}(16\text{nL}) = 8000$ s. Analogously, the longer dissolution time of the central droplet (> 10000 s) cannot be explained by an initial volume of 24 nL ($\tau_{\text{single}}(24\text{nL}) = 10000$ s). Hence, something else must be responsible for the accelerated dissolution of the outermost droplets. We interpret that this is most likely caused by the increased convection over this droplet pattern, caused by the larger amount of droplets, and hence the larger volume of (lighter) alcohol-saturated water. This stronger convection subjects the outermost droplets to an enhanced flow of clean water, increasing the dissolution rate and shortening the life time of the outermost droplets. Further inward in the pattern, the flow of water becomes progressively saturated by the dissolving droplets, reducing the dissolution rate from the innermost droplets and extending their dissolution time.

The initial footprints of the six droplets are indicated in red in panels A-C, illustrating that in contrast to the simulations, the droplet contact lines in the experiments are pinned by unavoidable local surface defects. This is especially visible for droplets 1 and 5, which are pinned to a point on their initial contact line throughout the entire dissolution process.

4.3.3 Droplet patterns: collective behavior

We now proceed by changing the number of droplets in the system and experimentally study the dissolution behavior in patterns of $n = 5, 19, 41$, and 127 droplets, placed at distances $d = 700$ µm ±100 µm apart (see Fig. 4.1), such that $d/L_0 = 1.4 \pm 0.2$. The same spacing to diameter ratio is adopted in the simulations of patterns containing either 5, or an infinite number of droplets; shell boundary conditions (BC) are used for

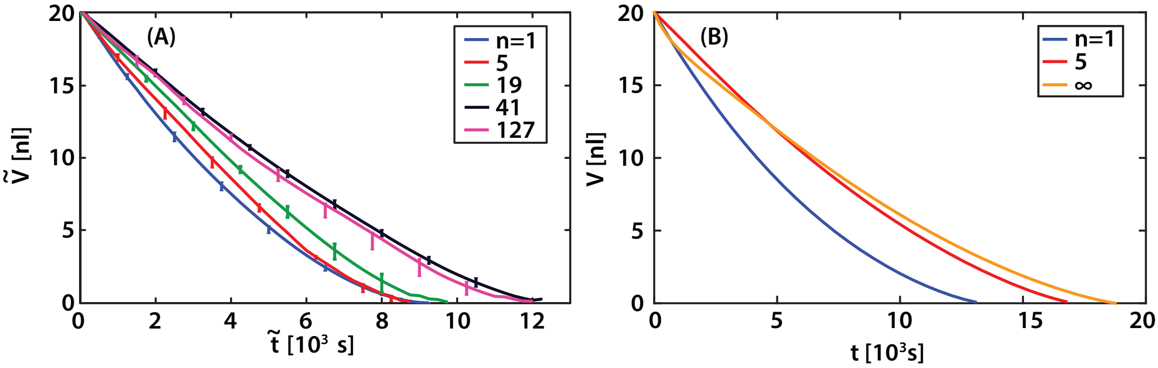

Figure 4.7: Volume of the center droplet as function of time, as obtained from experiments (A) and numerics (B), for individual dissolving droplets and droplet patterns of various sizes. Volume and time in panel A have been rescaled (as described in section 4.3.1, see Eqs. (4.1) and (4.4)) to correct for small differences in the initial droplet volumes. Lines in (A) represent the mean of multiple experiments. The error bars indicate the spreading between different repetitions of the experiment.

the single droplet, top BC for the infinite matrix and side BC for the 5 droplet matrix. As the camera used for these experiments (as discussed in section 4.2.1) could only produce a sharp image of a single droplet, the following sections discuss and present only the behavior of the center droplet in each pattern (as indicated in Fig. 4.3). The volumes of the center droplets are plotted as function of time in Figs. 4.7A and B for the experiments and simulations, respectively. Note that the tildes ($\tilde{V}$) and time ($\tilde{t}$) in Fig. 4.7A indicate the rescaled parameters, which are corrected for variations in initial droplet sizes between the measurements. V and t in Fig. 4.7B are obtained using the conversion factors, obtained as discussed in subsection 4.3.1. No rescaling was required in the simulations, as all droplets have exactly identical initial volumes. The dissolution of a single droplet is plotted as a reference in both figures and illustrates that the addition of extra droplets has a strong effect on the dissolution dynamics. More specifically, the slopes of the $V(t)$ curves (i.e., the volume loss rate) decreases upon the addition of more droplets, thus extending the droplet dissolution time.

To better appreciate the collective effect on the dissolution time, the experimentally and numerically measured dissolution times τ of the center droplets are plotted as function of $\log_{10}(n)$ in Fig. 4.8. The competition between the collective convective effect (increasing the dissolution rate and reducing the life time) and the collective

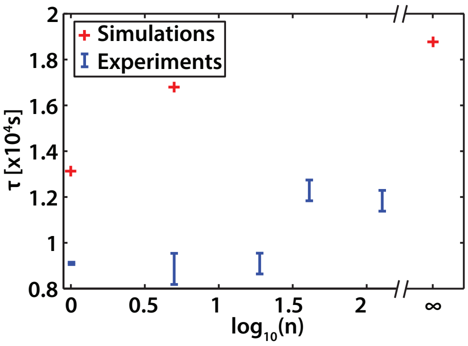

Figure 4.8: Dissolution time τ of the center droplet vs $\log_{10}(n)$, where n is the number of droplets in the pattern. The experimental dissolution times are for the center droplet, and are corrected for variations of the initial volumes, as explained in subsection 4.3.1. Note that in the experiment the dissolution time for $n = 5$ droplets, is smaller than for a single one, due to convective effects.

diffusive effect (leading to an extended life time) is nicely visible in the experiments on small patterns ($n = 5, 19$): no significant increase of the life time as compared to a single droplet can be observed. In these small patterns, the effect of the convective flow is such that it counteract the shielding effect of the neighboring droplets. This shielding effect only becomes strong enough to counteract the effect of the collective convection in the larger patterns ($n = 41, 127$), where the dissolution time of the center droplet is extended significantly as compared to a single droplet ($\tau = 9100$ s). The effect of buoyancy driven convection is absent in the simulations, and hence a considerable increase of the droplet life time is already observed in the 5 droplet pattern.

4.3.4 Droplet patterns: effect of droplet spacing

So far, the droplets in all patterns, both in experiments and in numerics, were placed at a spacing to diameter ratio $d/L_0 = 1.4$. Still, for a given number of droplets in the experiments, the dissolution time of the center droplet is found to vary between experiments and we hypothesize that this is due to an unintentional variation in the positioning of the droplets, possibly resulting in $d/L_0 \neq 1.4$. To test the influence of the (relative) droplet spacing on the dissolution process, we maintain the same droplet size ($V_0 = 20$ nL, $L_0 = 500$ µm), but construct patterns with different droplet spacing: the droplets were placed in a $n = 41$ pattern at ratios $d/L_0 = 1.1, 1.4, 2$, and 2.8 which we

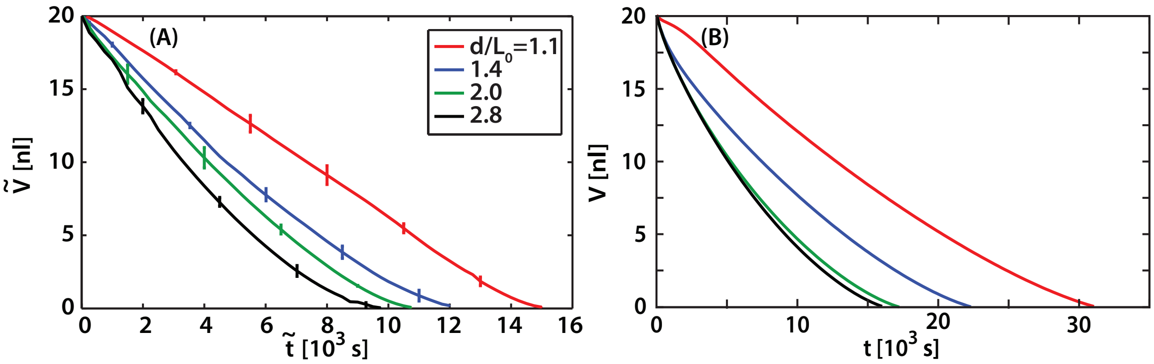

Figure 4.9: Volume of the center droplet as function of time for experiments (A) and numerics (B) on patterns with different ratios between the droplet-droplet distance d and the initial droplet diameter L_0. Lines in (A) represent the mean of multiple experiments. The error bars indicate the spreading between different realizations of the experiments.

compared to simulations on infinite patterns with identical ratios d/L_0. Top boundary conditions were used in these simulations (Fig. 4.3-E3).

The resulting droplet volumes are plotted as function of time in Fig. 4.9, revealing that both in the experiments and in the simulations the dissolution time is considerably enhanced when the droplets are more densely packed. The dissolution time τ is plotted as function of d/L_0 in Fig. 4.10 for both the experiments and simulations for direct comparison. It should be noted that in the limit $d/L_0 \to \infty$ (i.e., a single droplet), the simulations are not expected to result into the same behavior as the single droplet treated in section 4.3.1, due to the different boundary conditions used.

4.4 Conclusion

A three-dimensional diffuse interface numerical scheme was used to study collective effects in patterns of dissolving droplets and compared to experimental measures. A single droplet was used as a test case for comparison of the dissolution time of droplets placed at the center of finite and infinite patterns of mono-disperse droplets. For patterns comprising many droplets simulations and experiments were in good qualitative agreement, both measuring dissolution times of the center droplet typically tens of percent longer than for a single droplet, with highest dissolution times measured

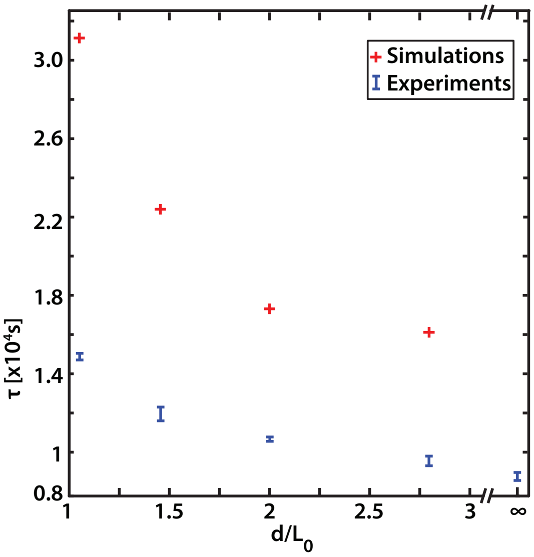

Figure 4.10: Droplet dissolution time τ as function of the relative droplet spacing. Both experiments and simulations show that the droplet dissolution time is increased in a denser packing.

for large, densely packed patterns.

Surprisingly, the experiments revealed a competition between an increased dissolution due to enhanced convection, and the inhibition of dissolution due to shielding by the neighboring drops. The influence of the convective flow was noticeable at the outermost droplets of the pattern, which exhibited dissolution times shorter as compared to an equally sized, single isolated droplet. Also for the center droplet in small ($n = 5, 19$) patterns, the enhanced convection was found to inhibit the shielding mechanism, leading to no clear increase in the dissolution time. Only for larger patterns of droplets, the collective effect was such that it counteracted the enhanced convection, and resulted in an extended dissolution time of the center droplet.

Our simulations confirmed the earlier hypothesis[120] that the reduced dissolution rate is caused by an increased concentration in between the droplets, lowering the concentration gradient and thus the dissolution rate. This effect was weaker at the edge of the pattern, causing the outermost droplets to dissolve more quickly than the inner droplets, an effect found in both the simulations and experiments.

Comparison between simulations and experiments showed that, even at low values of Rayleigh numbers, convective effects are not negligible and have to be considered in order to have an accurate description of dissolution phenomena. Convective effects are introduced in simulations in Chapter 6.

Future experimental work could eliminate convection, for example by reducing droplet sizes, or conducting the dissolution experiments in a micro-gravity environment[124]. Also, the current experimental system was limited by the fact that it could only measure the center droplet of the pattern. Future work could be improved by simultaneous volumetric measurements of all droplets in the pattern, for example through top view imaging combined with interferometry to obtain height profiles of the dissolving droplets[125].

CHAPTER 5

Phase change driven instabilities

5.1 Introduction

In this chapter we explore the interactions between evaporation, surface tension and capillary flows in confined geometries. During a phase change, a liquid surface can explore different configurations due to the interaction with solid boundaries. The surface tension of the liquid tends to minimise the exposed surface area, which can trigger large-scale capillary flows.

When the solid boundaries are flexible, the effect of surface tension is to drive the bending of solid structures[126]. This effect is responsible for the familiar observation of eyelash clumping by tears[127], which can be exploited to drive the self-assembly of elastic sheets as exemplified by the concept of capillary origami[128]. In microfluidics, capillary bending is responsible for the failure of micro-etched structures, which collapse upon evaporation of a solvent[129]. When the boundaries are rigid, the tendency of the interface to minimise its surface area leads to a readjustment of the interface configuration, subject to the constraint of the solid walls. Evaporating pinned drops, for example, drive capillary flows to their edges, leading to the familiar ring stains left behind by coffee droplets[5]. In the absence of pinning, the interaction with a solid surface can lead to a net translational motion, as illustrated by the migration of condensing droplets on cone-shaped cacti leaves[130].

Surface wettability is a key ingredient in the interaction of liquid fronts undergoing a phase change in contact with solid surfaces. A notable example in nature is the Namib desert beetle, which uses a hydrophilic-hydrophobic pattern on its back to assist the condensation of water droplets[131]. Subject to a wettability gradient, liquids tend to cover regions of higher wettability to minimise their surface energy, an effect that can be exploited to drive the unidirectional spreading[132].

Whilst evaporation and condensation of sessile droplets have received significant attention over the last years[15], the theoretical description of a liquid front in confinement subject to a phase change remains relatively unexplored. Here we study the isothermal phase change of a confined liquid-gas interface. We focus on a channel geometry, and explore the the stability of the interface focusing on the coupling between a phase change and the effects of the geometry and wettability of the solid boundaries. We develop a two-dimensional model of the stability of the front which adds the effect of a phase change and a wettability gradient to previous linear theories of front stability subject to a gradient in confinement[133,134]. We extend our study and explore the stability of the interface using full three-dimensional lattice-Boltzmann simulations[105,113], identifying the effect of contact-line slip on the front dynamics. To illustrate the applicability of our results in a practical situation, we present simulation results of the evaporation of a liquid front from a cantilever structure, showing that the well-known pinching-off of droplets leading to the collapse of the structures can be rationalised in the context of our theoretical and numerical results.

5.2 2D Theory

To begin our discussion, we focus on a simple two-dimensional model that captures the main features of interfacial fluid dynamics in confinement subject to a phase change. The system, shown in Fig. 5.1, corresponds to a liquid front undergoing a phase change, either evaporation or condensation, in a channel of length L and infinite width. The

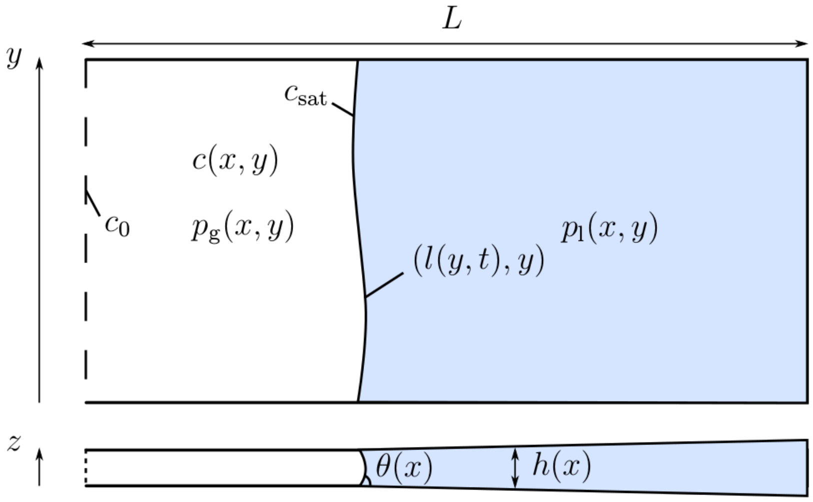

Figure 5.1: Sketch of a finite tapered channel containing a liquid (blue) that evaporates. The bottom image shows a cross section through the channel, the top image shows a top view.

liquid is confined by hard walls located at the top, bottom and right, and is exposed to a gas phase that is connected to an ambient reservoir through an open end at the left. The two fluids meet at an interface, whose xy coordinates, averaged over the gap of the channel in the z direction, are $(x = l(y,t), y)$.

The transverse structure of the liquid-gas interface (in the xz plane) is assumed to be a circular meniscus of local curvature

$$\kappa(y,t) = \frac{2\cos(\theta(l) - h'(l)/2)}{h(l)}. \tag{5.1}$$

Note, from (5.1), that we allow for spatial variations in the contact angle of the meniscus, $\theta(x)$, and the local thickness and inclination of the channel, $h(x)$, and $h'(x) \equiv \mathrm{d}h/\mathrm{d}x$, respectively. This will allow us to model the effect of wall wettability and confinement geometry on the stability of the liquid front. We consider the linear profiles

$$\theta(x) = \theta_0 + \alpha(x - x_0), \tag{5.2}$$

and

$$h(x) = h_0 + \beta(x - x_0), \tag{5.3}$$

where θ_0, h_0 and x_0 are reference values, and α and β are rates of change in the wetting angle and gap thickness.

The phase change is driven by an imbalance in the chemical potential between the liquid and gas. Here we consider the situation where the ambient concentration of vapour molecules in the gas, c_0, is different from the equilibrium saturation concentration, c_{sat}. An ambient concentration in excess of c_{sat} will result in the condensation of the liquid, while evaporation will occur if c_0 is short of c_{sat}. We consider the process to be isothermal.

In the absence of convective effects, and for slow evaporation rates relative to the typical diffusive timescale of the vapour in the gas, the gap-averaged concentration field of vapour molecules in the gas phase, $\langle c\rangle(x, y)$, obeys Laplace's equation, i.e.,

$$\frac{\partial^2\langle c\rangle}{\partial x^2}+\frac{\partial^2\langle c\rangle}{\partial y^2}=0. \tag{5.4}$$

The concentration field is subject to the boundary conditions

$$\langle c\rangle(x=0, y)=c_0, \tag{5.5}$$

and

$$\langle c\rangle(l, y)=c_{\mathrm{sat}}. \tag{5.6}$$

For a flat interface configuration, $l=l_0(t)$, the concentration profile varies linearly along the x coordinate. The interface position changes in time due to the volumetric flux caused by the phase change, E_0, i.e.,

$$\frac{\mathrm{d}l_0}{\mathrm{d}t}=-E_0, \tag{5.7}$$

where E_0 follows from Fick's Law,

$$E_0=-\frac{D}{\rho_{\mathrm{l}}}\frac{c_{\mathrm{sat}}-c_0}{l_0}, \tag{5.8}$$

where ρ_l is the liquid density and D is the diffusion coefficient of vapour molecules in the gas.

So long as the interface stays flat, the liquid and gas phases will remain at rest with respect to the channel walls. However, if the interface configuration is perturbed, at least three mechanisms can lead to a macroscopic flow in the volume of the fluid phases. First, mass diffusion will tend to increase the flux at points on the interface which lie closer to the open end of the channel. Secondly, local variations in the wall properties, caused by the spatial dependence of the contact angle and channel gap thickness, will result in differences in the Laplace's pressure along the interface. Finally, the in-plane curvature of the interface will lead to a relaxation of the front driven by surface tension.

To model the effect of such mechanisms on the interface dynamics, we focus on the limit of small channel aspect ratios, $h/L \ll 1$, and gentle gap variations, $h' \ll 1$. This allows us to study the fluid dynamics within the lubrication approximation. Here, the gap-averaged velocity field in each fluid obeys Darcy's Law:

$$\langle \mathbf{v}_i \rangle = -\frac{h^2}{12\eta_i}\boldsymbol{\nabla} p_i, \tag{5.9}$$

where $i = \{\mathrm{l}, \mathrm{g}\}$, $p_i(x, y)$ is the local pressure of the i-th phase, and η_i its viscosity. Imposing incompressibility, Eq. 5.9 reduces to a partial differential equation for the pressure field in each phase, i.e.,

$$h^3\left(\frac{\partial^2 p_i}{\partial x^2} + \frac{\partial^2 p_i}{\partial y^2}\right) + 3h^2 h' \frac{\partial p_i}{\partial x} = 0. \tag{5.10}$$

Adding to the kinematic effect of the evaporation rate, E_0, the underlying flow will contribute to the motion of the interface. The total interface speed thus reads

$$\frac{\partial l}{\partial t} = -E_0 + u_\mathrm{h}. \tag{5.11}$$

The hydrodynamic contribution, u_{h}, is given by Darcy's Law, i.e.,

$$u_{\mathrm{h}} = -\left.\frac{h^2}{12\eta_{\mathrm{l}}}\frac{\partial p_{\mathrm{l}}}{\partial x}\right|_{x=l,y} = -\left.\frac{h^2}{12\eta_{\mathrm{g}}}\frac{\partial p_{\mathrm{g}}}{\partial x}\right|_{x=l,y}. \tag{5.12}$$

The pressure jump at the interface is given by the Young-Laplace condition,

$$p_{\mathrm{l}}(l,y) = p_{\mathrm{g}}(l,y) + \gamma\left(\frac{\partial^2 l}{\partial y^2} - \kappa(l)\right), \tag{5.13}$$

where γ is the liquid-gas surface tension.

To analyse the stability of the front we consider the effect of a small sinusoidal perturbation to the interface shape

$$l(y,t) = l_0(t) + \epsilon\sin(ky)\exp(\sigma t), \tag{5.14}$$

where k is the mode of the perturbation, σ its growth rate and ϵ the amplitude. Following the standard linear-stability analysis approach described in Appendix A we obtain the growth rate of the perturbation,

$$\sigma(k) = \left[\frac{\gamma h_0^2}{12\eta_{\mathrm{t}}}\left(\frac{2\alpha\sin\theta_0}{h_0} + \frac{2\beta\cos\theta_0}{h_0^2} - k^2\right) - E_0\right]k, \tag{5.15}$$

where $\eta_{\mathrm{t}} \equiv \eta_{\mathrm{l}} + \eta_{\mathrm{g}}$. Using the capillary speed, $u_{\mathrm{cap}} \equiv \gamma/12\eta_{\mathrm{t}}$, and the channel thickness h_0 as the characteristic units for speed and length, we obtain the master curve

$$\hat{\sigma}(\hat{k}) = (\mathrm{Ch} + \mathrm{Ta} - \mathrm{E})\hat{k} - \hat{k}^3, \tag{5.16}$$

where we have defined $\hat{\sigma} \equiv h_0\sigma/u_{\mathrm{cap}}$ and $\hat{k} \equiv kh_0$.

The dispersion relation contains a purely stabilising term $\sim -\hat{k}^3$ arising from the relaxation of the in-plane curvature of the front. The remaining terms, all scaling as $\hat{k}$, can be either stabilising or destabilising. The effect of the phase change is controlled by the ratio $\mathrm{E} \equiv E_0/u_{\mathrm{cap}}$, which quantifies the competition between the diffusion-driven growth of the interface and the capillary speed. For $\mathrm{E} > 0$, corresponding to evaporation, the interface is stable, while the front tends to destabilise for $\mathrm{E} < 0$, corresponding to condensation.

The effect of variations in the channel wettability is quantified by the 'chemical' number $\mathrm{Ch} \equiv 2\alpha h_0 \sin\theta_0$. Positive α, corresponding to a situation where the liquid occupies the less wettable parts of the channel, favour unstable fronts. In such a case portions of the liquid exploring regions of lower contact angle experience a lower Laplace pressure relative to the rest of the interface, driving the growth of perturbations. The same capillary mechanism drives the invasion of the thinner end of the channel ($\beta > 0$) by wetting liquids ($\theta_0 < \pi/2$). This effect is quantified by the shape parameter, or 'tapering' number, $\mathrm{Ta} \equiv 2\beta\cos\theta_0$.

The combination of these effects leads to the onset condition for an unstable front,

$$\mathrm{Ch} + \mathrm{Ta} - \mathrm{E} > 0. \tag{5.17}$$

In such a regime, perturbations to the interface shape destabilise the front from the flat configuration provided they are below a critical wavenumber

$$\hat{k}_{\mathrm{c}} = (\mathrm{Ch} + \mathrm{Ta} - \mathrm{E})^{1/2}\,. \tag{5.18}$$

Perturbations with smaller modes than $\hat{k}_{\mathrm{c}}$ are always unstable, with a fastest growing mode $\hat{k}_{\mathrm{m}} = \hat{k}_{\mathrm{c}}/\sqrt{3}$.

5.3 3D Model and Lattice Boltzmann Simulations

The theory presented in Sec. 5.2 captures the main competing effects that govern the stability of a liquid front undergoing a phase change in a channel geometry. However, we expect that 3D effects arising from viscous forces linked to the structure of the meniscus, including the contact line, affect the interface dynamics. 3D simulations can be a valuable tool to explore these effects. Furthermore, they can be used to study more complicated geometries beyond the channel configuration studied in this thesis.

In this section we consider a diffuse interface model of the Cahn-Hilliard type and present Lattice-Boltzmann simulations of the dynamics of a confined front. We present simulation results where we focus on situations where the front is subject to a gradient in channel wettability (finite Ch) or a phase change (finite E), before addressing the situation where both effects come into play simultaneously.

5.3.1 Lattice-Boltzmann Simulations

We carried out Lattice Boltzmann simulations of the stability of a flat interface using the Cahn-Hilliard model described in Chapter 2.

We set up a rectangular simulation domain of dimensions $L_x = 100$ and $L_z = 16$ in lattice units, and a variable width L_y. We impose periodic boundary conditions in the y direction, and hard walls at the top, bottom, left and right faces. The resulting rectangular channel is filled with the gas phase ($\phi = -1$) up to a distance $l = l_0 + \epsilon \sin(ky)$ in the x direction, where $k = 2\pi/L_y$ is a single mode occupying the width of the simulation domain with amplitude ϵ. The rest of the channel is filled with the liquid phase, where $\phi = +1$. The density and viscosity of the fluid are set to $\rho = 1$ and $\eta = 1/6$ throughout the simulation domain. The bulk free-energy parameters are set to $-a = b = 3.05 \times 10^{-3}$ and $\kappa = 7.8 \times 10^{-3}$, giving a surface tension $\gamma = 4.6 \times 10^{-3}$ and an interface thickness $\xi = 1.13$.

The interaction with the top and bottom walls is prescribed by imposing a gradient $\Delta\theta/\Delta l$ in the wetting angle. This is done by locally fixing the surface energy parameter, κ_{s}, and enforcing the boundary condition (2.39). The gradient in the wetting properties is imposed over a region of length Δl about the initial position of the unperturbed interface, l_0. In this region, the wetting angle varies by an amount $\Delta\theta$. By choosing Δl and $\Delta\theta$ we adjust the parameter $\alpha \approx \Delta\theta/\Delta l$. The length scale Δl is fixed to be several times the interface width, ξ, i.e., $26\xi \le \Delta l \le 88\xi$. On the other hand, $\Delta\theta$ is restricted by the accuracy of the LB implementation of (2.39), and lies in the range $35° \le \Delta\theta \le 75°$.

To drive a phase change, we follow the procedure presented in Chapter 3 and fix the

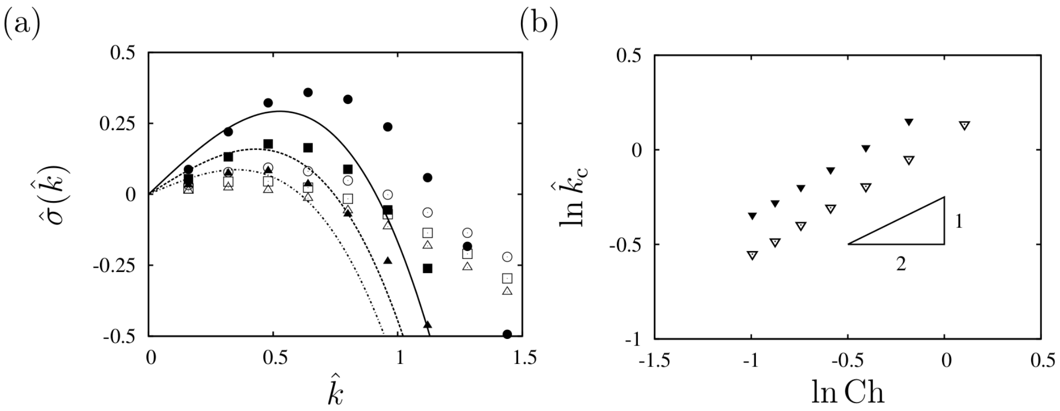

Figure 5.2: (a) Dispersion relations of a perturbed front subject to a wettability gradient in a straight channel. The strength of the variation in the wetting properties is quantified by Ch, which takes values 0.83 (circles; solid line), 0.56 (squares; dashed line) and 0.37 (triangles; dot-dashed line). The diffusive length scale, controlling the contact-line slip, is fixed to $l_D = 9.1 \times 10^{-2}$ (open symbols) and $l_D = 9.1 \times 10^{-1}$ (full symbols). Symbols correspond to LB simulations. Lines correspond to the 2D theoretical prediction. (b) Critical wavenumber as a function of Ch for $l_D = 9.1 \times 10^{-1}$ (full triangles) and $l_D = 9.1 \times 10^{-2}$ (open triangles). The triangle indicates the 2D scaling $\hat{k}_c \sim \mathrm{Ch}^{1/2}$.

value of the phase field at the left end of the simulation box to a prescribed value ϕ_0. From Eq. 2.41 the local chemical potential in the bulk is $\mu_0 \simeq a\phi_0 + b\phi_0^3$, while $\mu \approx 0$ at the interface, leading to a phase-change rate $E_0 = |\mathbf{j}|/\Delta\phi \simeq M\mu_0/\Delta\phi l_0$, where $\Delta\phi = 2$ is the difference between the bulk values of the phase field. We consider ϕ_0 values in the range $-1.4 \leq \phi_0 \leq -0.6$, which ensure that the timescale of mass diffusion is fast compared to the evaporation timescale of the front.

5.3.2 Effect of a gradient in the channel wettability

We first present results for the stability of the front in the presence of a gradient of the wetting angle and no phase change. We consider three values of the chemical number, Ch = 0.37, 0.56 and 0.83. We fix $\epsilon = 0.5$ and vary the wavelength of the perturbation in the range $90 \leq L_y \leq 1256$. For each wavelength we track the evolution of the perturbed interface over time and measure the corresponding exponential growth rate, σ.

Fig. 5.2(a) shows the dispersion relations obtained from the simulations, reported in the dimensionless variables $\hat{\sigma}$ and $\hat{k}$ defined in Sec. 5.2. We also plot the 2D prediction of Eq. 5.16. To explore the effect of the contact-line slip we present simulation results for two values of the diffusive length scale $l_{\mathrm{D}} = 9.1 \times 10^{-2}$ and 9.1×10^{-1}, obtained by fixing $M = 0.05$ and $M = 5$, respectively. The full symbols in the figure correspond to $l_{\mathrm{D}} = 9.1 \times 10^{-1}$, and show a reasonable agreement with the 2D theory at small $\hat{k}$. We do not expect a quantitative match at relatively larger modes, $\hat{k} \sim 1$, where the wavelength becomes comparable to the channel-gap thickness and the validity of the 2D theory ceases to hold. The open symbols correspond to the smaller diffusive length used, $l_{\mathrm{D}} = 9.1 \times 10^{-2}$, and give smaller growth rates relative to the 2D result. This supports that l_{D} controls the friction at the contact line, leading to an increased damping of the perturbed interface.

Qualitatively, the range of unstable modes becomes larger with increasing Ch for both values of l_{D}, reflecting the effect of a stronger driving due to the gradient in the channel wettability. To quantify this effect, we measured the critical mode, $\hat{k}_{\mathrm{c}}$, as a function of Ch (Fig. 5.2(b)). A fit of the data gives $\hat{k}_{\mathrm{c}} \approx (0.99\mathrm{Ch})^{1/2}$ for $l_{\mathrm{D}} = 9.1 \times 10^{-2}$ and $\hat{k}_{\mathrm{c}} \approx (1.46\mathrm{Ch})^{1/2}$ for $l_{\mathrm{D}} = 9.1 \times 10^{-1}$. These results are in good agreement with the 2D scaling $\sim \mathrm{Ch}^{1/2}$ predicted by Eq. 5.18 up to the numerical pre-factor, which is order unity and shows a weak dependence on l_{D}.

5.3.3 Effect of a phase change

We now move to investigate the effect of evaporation and condensation on the stability of the front. We consider a straight channel of uniform neutral wetting properties, i.e., $\theta_{\mathrm{e}} = 90^\circ$, and vary the rate of phase change, E. The diffusive length is fixed to $l_{\mathrm{D}} = 9.1 \times 10^{-1}$, while all other parameters are fixed as in the previous section.

Fig. 5.3(a) shows the dispersion relations obtained for several values of E along with the corresponding theoretical curves. As expected, positive values of E, corresponding to evaporation, always result in stable fronts. On the other hand, negative E, corresponding to condensation, can destabilise the interface, as can be seen in the inset of Fig. 5.3(a).

As we showed in the previous section, the growth rate of the perturbation depends

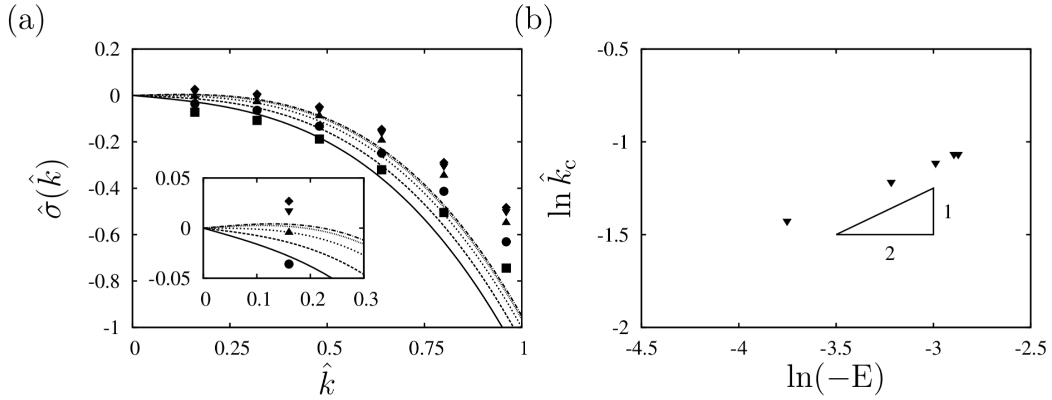

Figure 5.3: (a) Dispersion relation of a front subject to a phase change. The phase change is quantified by the dimensionless rate, E, which takes the values $+14.97\times10^{-2}$ (squares), $+6.38\times10^{-2}$ (circles), 0 (up triangles), -3.64×10^{-2} (down triangles) and -4.99×10^{-2} (diamonds). (b) Scaling of the critical wavenumber with E. The triangle indicates the 2D scaling $\hat{k}_\mathrm{c} \sim (-\mathrm{E})^{1/2}$.

on the diffusive length, $l_\mathrm{D} = \sqrt{M\eta}$, which controls the contact-line slip. Therefore, in order to obtain a better agreement with the 2D theory, one could reduce l_D. However, the diffusive transport in the bulk occurs over a timescale $\tau_\mathrm{D} \simeq l_0/|E_0| \sim 1/M$. As a consequence, l_D is restricted to relatively large values in order to keep τ_D small compared to the timescale of evaporation of the front[105]. Despite this limitation of the model, the qualitative agreement with the theory is preserved in the unstable regime. As shown in Fig. 5.3(b), the critical wave number follows the $\hat{k}_\mathrm{c} \sim (-\mathrm{E})^{1/2}$ scaling of Eq. 5.18, with a best fit to the data $\hat{k}_\mathrm{c} \approx (-2.2\mathrm{E})^{1/2}$.

5.3.4 Stability phase diagram

We explored the stability of the front subject to the combined effects of a wettability gradient and a phase change in the intervals $-0.4 < \mathrm{Ch} < 0.4$ and $-0.1 < \mathrm{E} < 0.2$. In the simulations, we fix the height and width of the channel to $L_z = 16$ and $L_y = 1256$, and impose a single-mode perturbation with $\hat{k}_0 = 2\pi L_z/L_y \approx 0.08$. For a fixed value of Ch, we carry out simulations decreasing E from an initial positive value until the interface destabilises.

Fig. 5.4 shows the resulting stability phase diagram. Full circles correspond to stable fronts, i.e., $\hat{\sigma}(\hat{k}_0) < 0$ for given E and Ch, while open squares correspond to

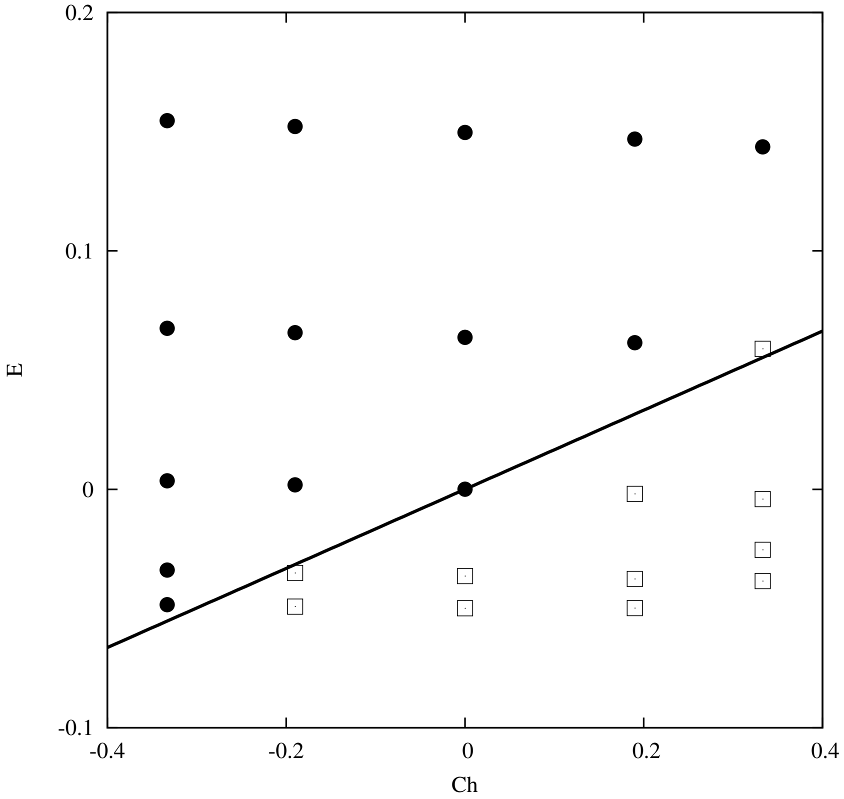

Figure 5.4: Stability phase diagram for a front subject to a single-mode perturbation under a phase change and a wettability gradient. Full circles correspond to stable fronts, open squares correspond to unstable fronts. The solid line indicates the linear marginal stability boundary.

unstable fronts. From (5.18) we expect that the front becomes unstable as $\hat{k}_0 \to \hat{k}_c$, where $\hat{k}_c = (\mathrm{Ch} - \mathrm{E})^{1/2}$. The marginal stability line in the $\mathrm{Ch} - \mathrm{E}$ diagram is given by $\mathrm{E} \sim \mathrm{Ch} - \hat{k}_0^2$. The simulation results confirm the linear scaling, with $\mathrm{E} \simeq 0.16\mathrm{Ch}$, shown as a solid line in Fig. 5.4.

5.3.5 Evaporation on etched structures

To illustrate the wider relevance of the interplay between a phase change and channel confinement on the stability of a liquid front, we consider the evaporation of a solvent from a chemically etched structure, which is a typical problem in microfluidics. The system in question is a rectangular microbeam fixed to the right wall of a microfluidic trench. The trench is formed by two vertical walls of height H and joined by a horizontal wall of length L. An open end at the top allows the evaporation of a solvent. The beam forms an overhanging cantilever, suspended from the floor of the trench at a

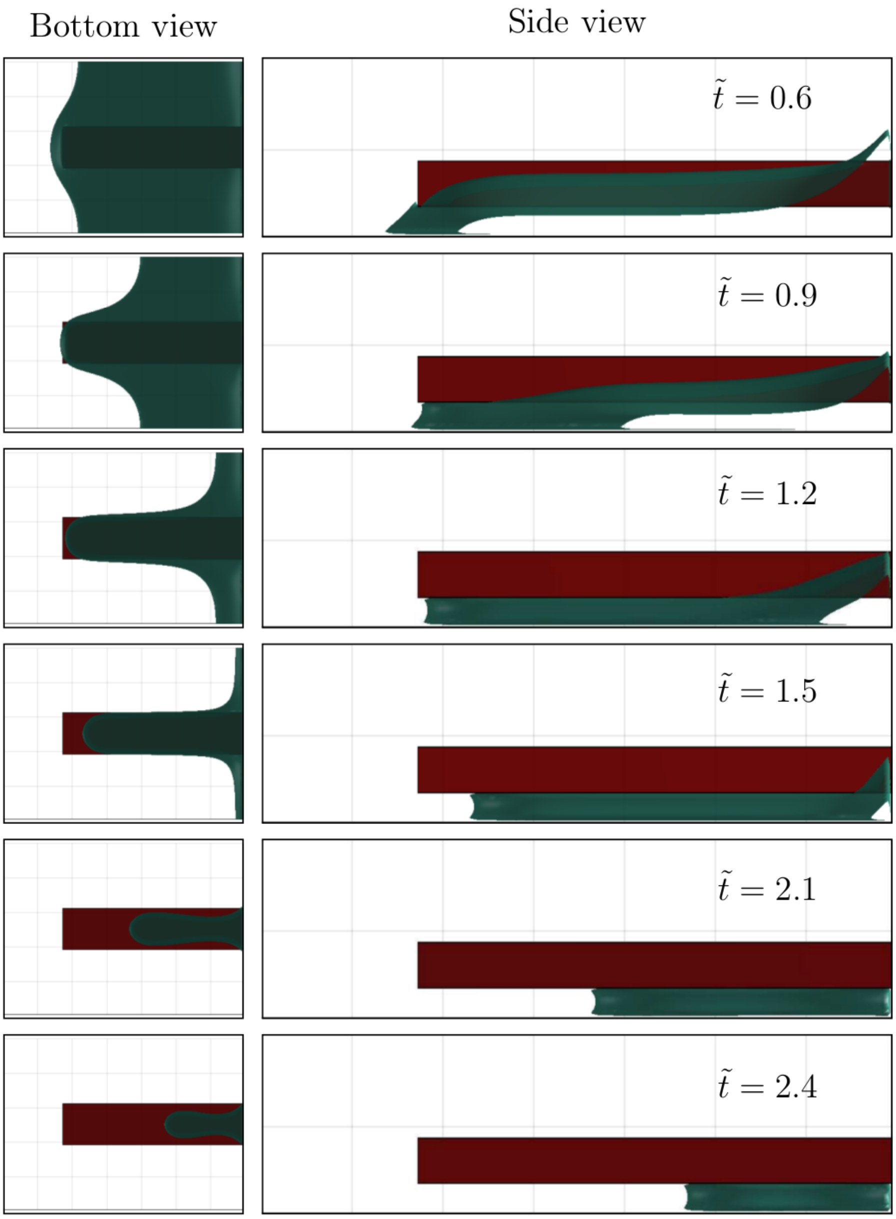

Figure 5.5: Simulation results of a front evaporating on a rigid straight cantilever. Upon evaporation, the interface forms a meniscus under the cantilever, and forms a receding finger-like meniscus. Times are measured in units of the evaporation timescale $(H-h)/E_0$.

local height h. The resulting structure is repeated in the transverse direction along the trench, with a separation distance between beams W.

We thank Rodrigo Ledesma-Aguilar[135] for providing the following LB simulations. We consider the evaporation of a liquid front which initially covers the top of the beam. The evaporation is driven by fixing the phase field to $\phi_0 = -1.2$ at the top end of the simulation domain. This leads to the retraction of the liquid front, which moves at a speed $E_0 \simeq M\mu_0/\Delta\phi(H-h)$. Fig. 5.5 shows a simulation sequence of the interface dynamics. We report simulation times in units of the evaporation timescale $(H-h)/E_0$, i.e., $\tilde{t} = tE_0/(H-h)$. As shown in the sequence, after the liquid front comes into contact with the cantilever, the covered portion recedes slower than the exposed surface. This effect is the result of a reduced surface area available for evaporation and an increased hydrodynamic resistance caused by contact with the cantilever. After some time, however, the front fully recedes until the liquid completely evaporates.

We repeated the simulation introducing a small step Δh in the thickness of the beam, so that the gap between the cantilever and the floor of the trench is $h + \Delta h$ at the right, and h at the left. The length of the thicker portion of the beam is Δl. As shown in Fig. 5.6, the evaporation process is essentially the same until a time $\tilde{t} \simeq 1.2$. At later times, the tip of the interface recedes at a significantly slower rate compared to the evaporation in contact with the straight cantilever. This is evident by comparing the panels corresponding to $\tilde{t} = 2.1$ in Fig. 5.5 and $\tilde{t} = 1.8$ in Fig. 5.6. Such an effect cannot be caused by evaporation alone, as one would expect that a larger exposed surface area at the right end of the cantilever would increase the total evaporation rate. Instead, the slower retraction of the tip suggests a hydrodynamic flow from the right to the left. Indeed, as viewed from the bottom, the interface develops a spoon shape, with a thinning neck which eventually collapses, leading to the formation of a capillary bridge trapped under the thicker end of the cantilever. As observed in the figure, this process occurs over a much faster timescale $\Delta\tilde{t} \simeq 2.1 - 1.9 = 0.1$, than that of evaporation, $\hat{t} \sim 1$. At time $\tilde{t} = 1.9$, just after pinch-off, the capillary bridge has a visible curvature difference between the left and right edges. The corresponding difference in the Laplace pressure results in a net force to the left. In fact, at time $\tilde{t} = 2.0$ both edges move to the left, as shown in the dashed box in the figure. This supports that the difference in Laplace pressure caused by the change in the beam thickness can induce the growth of the front.

In the context of microfluidics, the formation of the capillary bridge shown in Fig. 5.6 has been suggested as a potential cause of failure in the micro fabrication of

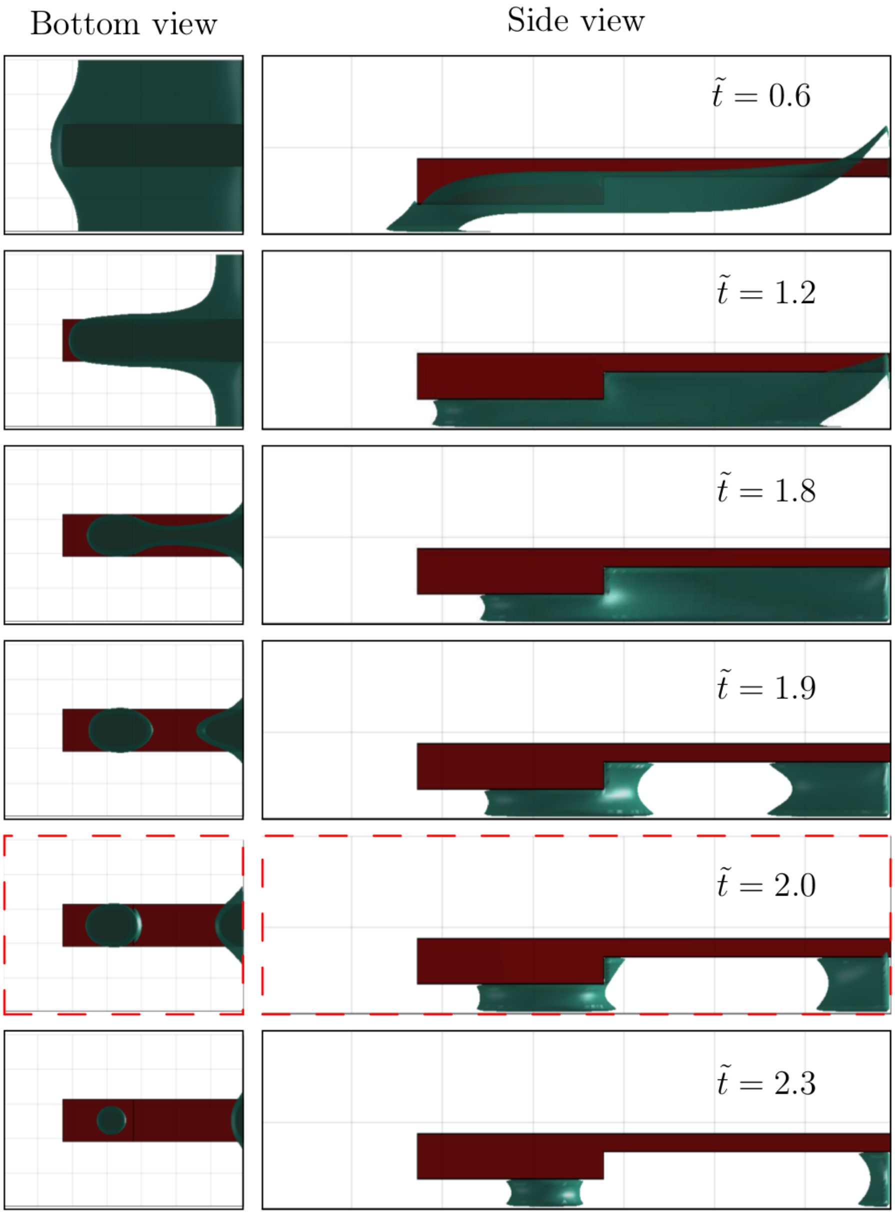

Figure 5.6: Simulation results of a front evaporating on a rigid step cantilever. Upon evaporation, the interface forms a meniscus under the cantilever. The difference in curvature between the tip and the body of the meniscus drives a capillary flow towards the tip. The interface develops a spoon-like shape and pinches-off to form a droplet. The dashed box shows that the flow drives the droplet forward to the left, against the effect of evaporation. Times are measured in units of the evaporation timescale $(H - h)/E_0$.

cantilever structures. This situation arises in the last steps of the fabrication process, where a solvent is used to wash out the residue left after chemical etching of the cantilevers. Beams whose length exceeds the elastocapillary length are prone to be deflected by the surface tension of an evaporating solvent. This has been reported to result in the formation of a liquid bridge at the free end of the beam, which, upon

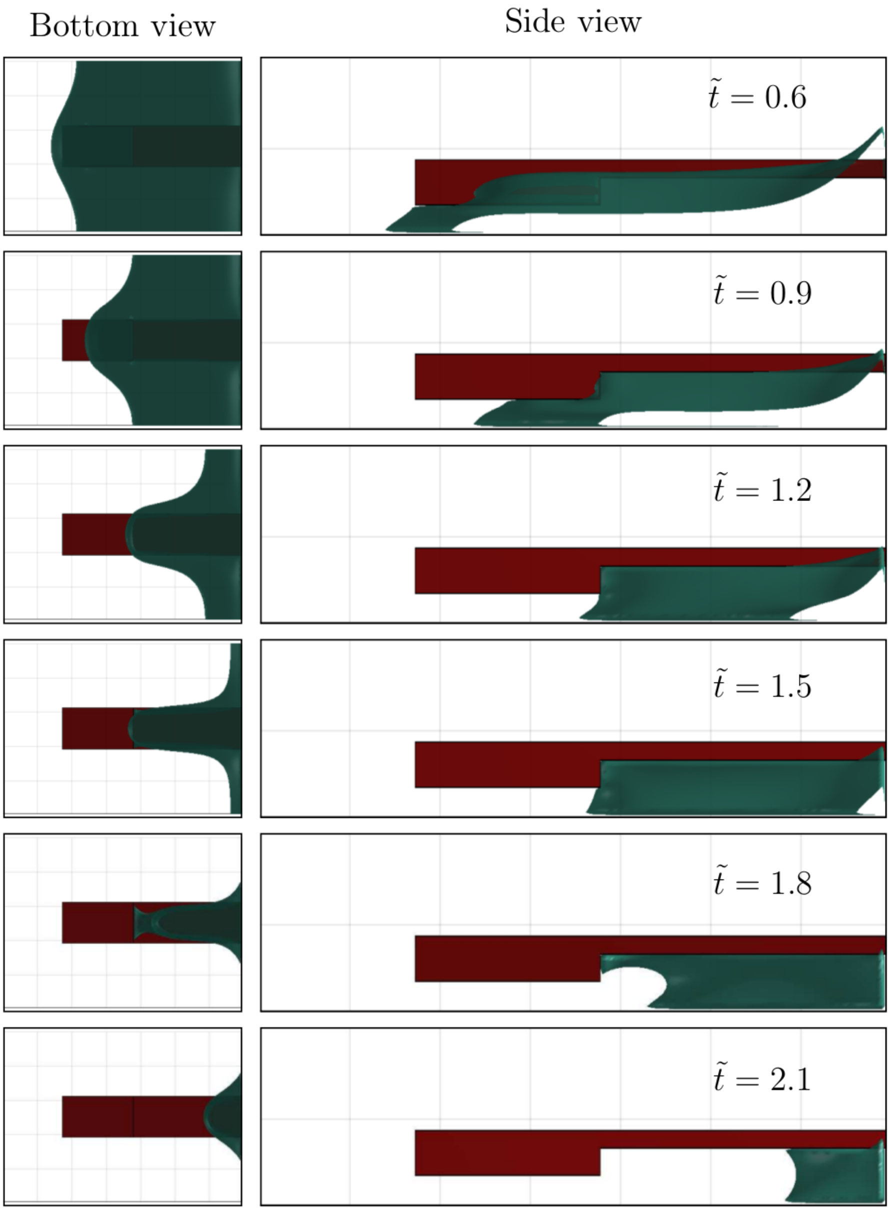

Figure 5.7: Simulation results of a front evaporating on a rigid step cantilever patterned with a hydrophobic patch. The chemical patterning induces a rise in the capillary pressure between the tip and the body of the meniscus, which counteracts the effect of the height change. As a result, the interface quickly recedes from the hydrophobic patch, preventing the formation of a droplet in the shallow region of the cantilever. Times are measured in units of the evaporation timescale $(H - h)/E_0$.

evaporation, causes the collapse of the cantilever structure.

Our simulations show that the mechanism leading to the formation of the capillary bridge is hydrodynamic, and can be rationalised in the context of the front stability presented in Sec. 5.2. For the straight cantilever simulations Ch and Ta vanish, whilst $\mathrm{E} = E_0/u_{\mathrm{cap}} \approx 0.09 > 0$, leading to the observed stable fronts. For the step cantilever, however, there is a gap thickness gradient $\beta \simeq \Delta h/\Delta l = 0.15$, which gives $\mathrm{Ta} = 2\cos\theta_0\beta \approx 0.26 > \mathrm{E}$. As a result, one expects an instability with a typical wavenumber $\hat{k}_\mathrm{m} = (\mathrm{Ta} - \mathrm{E})^{1/2} \approx 0.38$. This is consistent with the simulation results, where the wavelength of the pattern is determined by the width of the simulation domain, with a corresponding wave number $\hat{k} \approx 0.37$.

To suppress the instability one can resort to a chemical patterning of the substrate. To exemplify this idea we repeated the step-cantilever simulation, however, we now introduce a hydrophobic patch on the bottom surface of the narrow end of the cantilever. The contact angle on the patch is $\theta_1 = 150°$, while the rest of the solid surfaces have $\theta_0 = 30°$. The patch extends over the thicker portion of the beam, of length Δl, and thus creates a gradient in the wettability of the cantilever. The simulation results, shown in Fig. 5.7 show that the meniscus quickly retracts from the hydrophobic portion of the beam.

The contact angle used give an approximate value $\mathrm{Ta} = 0.15$. On the other hand, the step change in the wetting properties of the beam gives a gradient $\alpha \simeq \Delta\theta/\Delta l = -0.025$, and a corresponding dimensionless number $\mathrm{Ch} \simeq 2(h+\Delta h/2)\sin\langle\theta\rangle\alpha \approx -0.4$. Therefore, the instability is completely suppressed and the front recedes faster due to the capillary suction that results from the dominance of Ch over Ta.

5.4 Conclusions

Our analytical and numerical results illustrate general features governing the stability of liquid fronts undergoing a phase change in confinement. On the one hand, the growth of the front is affected by variations in the diffusive current along the interface due to the evaporation or condensation. The effect of confinement adds a hydrodynamic mechanism to this picture, where flow is driven by gradients in the Laplace pressure along the interface. Such a mechanism can arise either because of changes in the local length scale of confinement, or because of variations in the wettability of the solid walls. The net effect of each of these mechanisms relative to the stabilising surface tension can be quantified by the dimensionless numbers Ch, Ta, and E, which capture the effects of varying wetting properties, geometry and a phase change. The typical timescale of the front dynamics is controlled by the capillary speed u_{cap}, the confining length scale h_0 and the slip length arising from the friction at the contact line l_s.

These principles can be applied to understand the dynamics of fronts undergoing a phase change in more complicated geometries. This is particularly relevant in microfluidics applications.

CHAPTER 6

Effect of flows on evaporation

Although droplet evaporation is almost always considered to be a diffusion dominated process, there are cases when flows are important. Flows can arise either because of a difference in density between the evaporating fluid and the surrounding one, or because of an applied external flow field.

For example macroscopic water droplets evaporating in air have been observed to break the D^2 law[6] described in Chapter 1; it has been shown experimentally that the temporal evolution of the droplet radius is $R \approx (t - t_0)^\alpha$ with $\alpha \approx 0.6$, in contrast with the expected value $\alpha = 0.5$ predicted by diffusion theory. The reduction arises because water vapour is lighter than air, so it is subject to buoyancy forces that carry it away from the drop, thus modifying its concentration profile with respect to the diffusion limited process.

In order to quantify the effect of convection relative to diffusion, it is useful to use the Rayleigh number

$$Ra = \frac{g\beta_c \Delta c L^3}{\nu D} \tag{6.1}$$

which was introduced in Chapter 1.

It has been shown[7] that two different regimes exists for evaporation: for low Rayleigh numbers diffusion is the dominant mechanism driving evaporation and the predictions from diffusion theory holds; for high Rayleigh numbers convection dominates. At intermediate values of Ra there is a crossover between the two regimes. High Rayleigh numbers occur either because of big density differences or big droplet size.

In order to quantify the contributions to evaporation coming from diffusion and convection it is useful to use the Sherwood number, introduced in Chapter 1, which the ratio of the actual mass transfer rate to the diffusion rate,

$$Sh = \frac{\dot{m}L}{A\Delta c D}, \tag{6.2}$$

where $\dot{m}$ is the temporal change of the mass of the evaporating fluid, L a typical length scale of the system, A the surface area of the evaporating fluid, and Δc and D have already been defined. For an hemispherical sessile drop of radius R Sh is

$$Sh = \frac{\rho dV/dt}{\pi D \Delta c R} \tag{6.3}$$

where dV/dt is the measured evaporation rate. Thus in the diffusion dominated regime, we have $Sh = 1$, while in the convection-dominated regime $Sh \gg 1$. It can be shown[136] that for high Rayleigh numbers Sh scales as

$$Sh \sim Ra^{1/4}. \tag{6.4}$$

6.1 Lattice-Boltzmann simulations

We have simulated the evaporation of droplets subject to buoyant forces. We model the buoyant force by a gravity-type term of the form

$$F = a(\phi - \phi_h) \tag{6.5}$$

where a is a constant used to tune the intensity of the force and ϕ_h is the value of the order parameter fixed at specific boundaries of the system as explained in Sec. 3.3. This force is applied only on the fluid surrounding the droplet and not on the droplet. It is worth mentioning that we are not free in choosing the intensity of the body force in the simulations because of stability reasons and the fact that a big enough force can lift off the drop from the surface. This happens for values of the Rayleigh number $Ra > 0.1$. The main reason for this limitation is the density ratio used in the LB algorithm which is equal to one; a higher density ratio can give higher Rayleigh numbers.

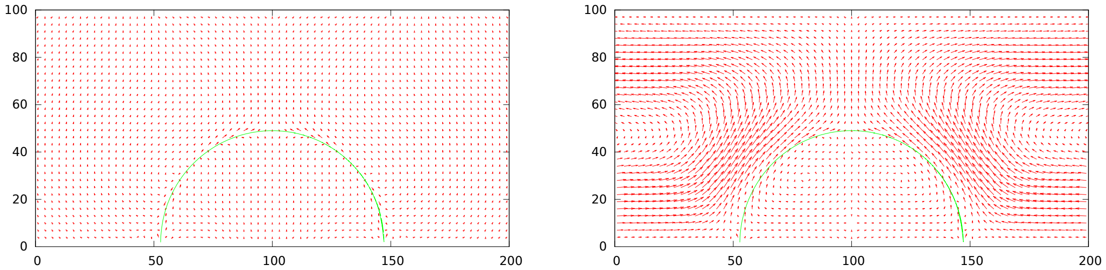

Figure 6.1: Flow field around an evaporating droplet not subject to buoyant forces (left) and subject to buoyant forces (right).Velocities are scaled by a factor of 10^4 in both figures.

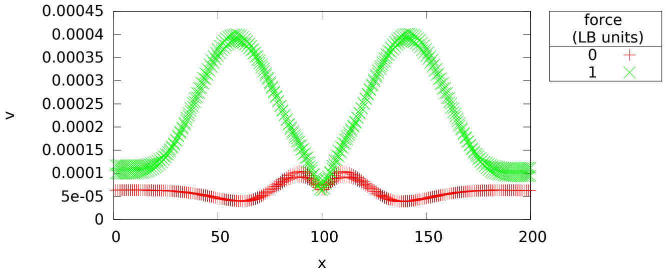

Figure 6.2: Magnitude of the velocity field at $z = N_z/2$ for an evaporating droplet with no buoyancy force and buoyancy force present.

We simulated 2D droplets in a system of size $(N_x, N_y, N_z) = (200, 1, 100)$ with a droplet initial radius $R_0 = 50$. Shell BC were used to fix the order parameter $\phi_H = -1.2$ to drive evaporation. We explored the region of Rayleigh numbers between $Ra \approx 10^{-4}$ and $Ra \approx 0.1$.

In Fig. 6.1 the flow field around the dissolving droplet is shown for the case of no buoyancy (left) and buoyancy (right); it is clear that buoyancy induces a non-negligible flow. Qualitatively buoyant forces induce the formation of two plumes at the sides of the drop as shown in Fig. 6.1 right. The flow pattern observed with buoyancy is also qualitatively similar to that observed in experiments[7]; Fig. 6.3 shows an alcohol drop dissolving in water and the relative flow field; the alcohol used is slightly lighter than water so it is subject to buoyancy.

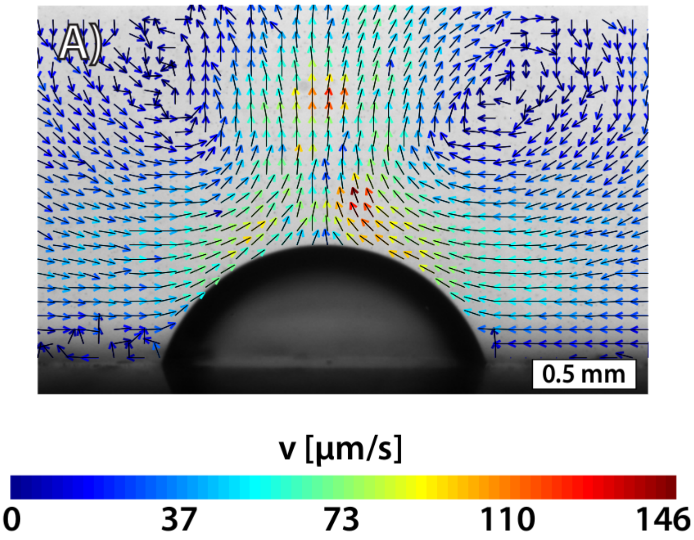

Figure 6.3: Flow field around a 1-pentanol droplet dissolving in water[7]. Courtesy of Erik Dietrich.

In order to quantify the change in the flow field Fig. 6.2 shows the magnitude of the velocity field on a line just over the drop at $z = N_z/2$. The graph shows a clear presence of a flow induced by buoyancy (it is worth mentioning that this graph corresponds to the lowest value of the parameter a used); the comparison with the no-buoyancy case shows that these velocities are physical and they are not spurious velocities coming from the LB algorithm.

Fig. 6.4 shows a graph of the Sherwood number as a function of the Rayleigh number for these simulations. Each curve corresponds to a different simulation where the buoyancy force is varied by varying the parameter a. For the shell BC the Sherwood number can be calculated exactly using the results presented in Chapter 2.

The results show that Sh is almost equal to 1 for each value of the force applied, although it increases as the buoyancy force increases.

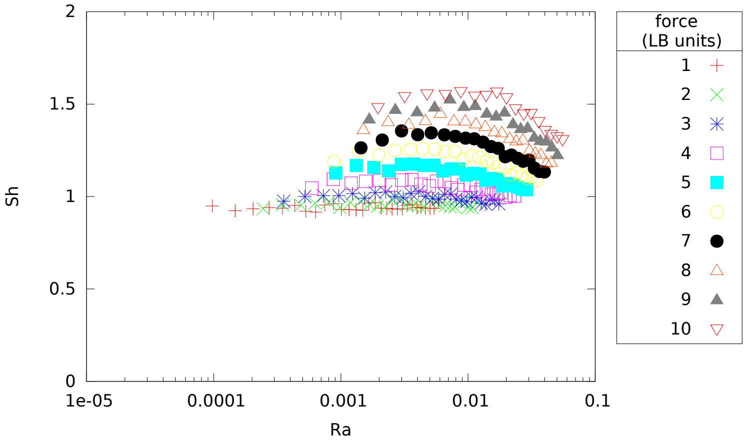

Figure 6.4: Sherwood number vs Rayleigh number for 2D hemispherical drops subject to shell boundary conditions. The initial radius is 50 lattice units.

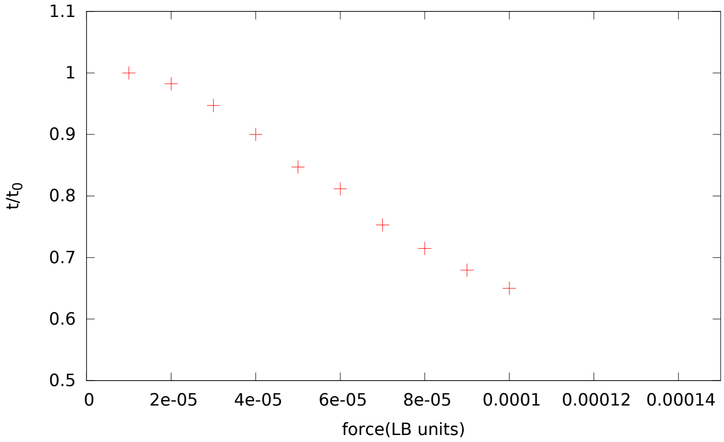

Figure 6.5: Lifetime of an evaporating droplet (with shell BC) subject to a buoyant force (compared to the lifetime of the same droplet subject to no buoyancy) as a function of the force applied.

Although we are in the diffusion dominated regime, the droplet lifetime depends on the magnitude of the buoyant force applied, as can be seen in Fig. 6.5. The graph shows that with LB simulations we can access values of the Rayleigh number where the effect of buoyancy can reduce a droplet lifetime up to 60% compared to the case where no buoyancy is present.

Using top boundary conditions instead of shell BC leads to the results presented in Figs. 6.6-6.9. Figs. 6.6-6.7 show the flow fields and the velocities magnitudes as in Fig. 6.1 but for the top BC case. The flows appear similar, although the different boundary conditions led to a slightly different flow pattern in the presence of buoyancy. In fact two full vortices appear in Fig. 6.6-(b), while the same system in Fig. 6.1 does not show full vortices due to the different boundary conditions used. The different behaviour is also illustrated in Fig. 6.7. Note that the velocity magnitude tends to zero at the system's boundaries when shell BC are used (see Fig. 6.2), while in this case it reaches its maximum value at the boundaries.

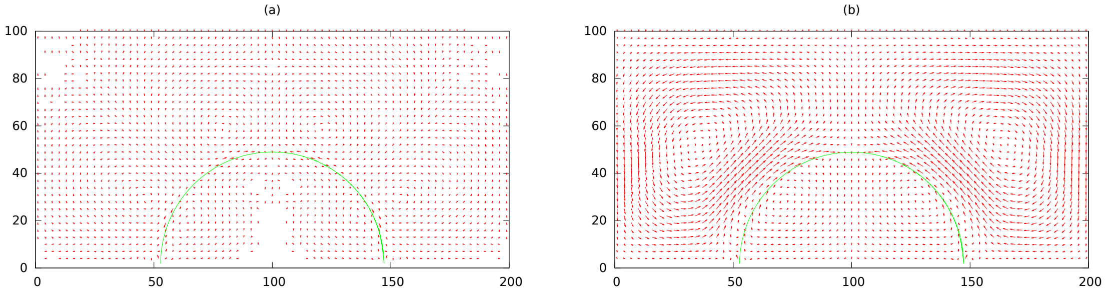

Figure 6.6: Flow field around an evaporating droplet (a) not subject to buoyant forces and (b) subject to buoyant forces. Velocities are scaled by a factor of 10^4 in both figures. Top BC are used.

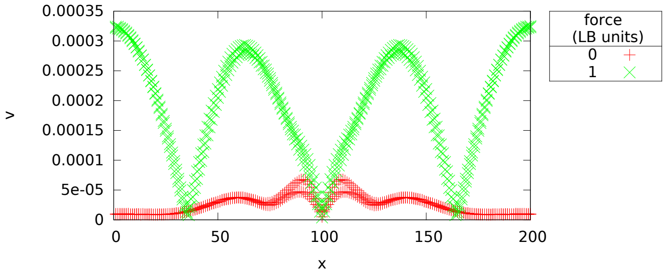

Figure 6.7: Magnitude of the velocity field at $z = N_z/2$ for an evaporating droplet with no buoyancy force and buoyancy force present. Top BC are used.

Fig. 6.8 shows the Sh-Ra plot for this case. The Sherwood number is less than one because we have used the formula for an isolated droplet for its theoretical value, while the use of the top BC physically corresponds to an infinite matrix of droplets; in this case we expect a lower dissolution rate due to the presence of neighbouring droplets.

The presence of other droplets has two effects however. Firstly it tends to slow down the dissolution because of the increased solute concentration due to neighbour droplets. Secondly it enhances it because of faster convection, also caused by the presence of a larger solute concentration. Thus there is a competition of these effects in the dissolution dynamics, which has been described in Chapter 4.

Results in Fig. 6.9 show that a droplet subject to buoyancy and surrounded by other droplets can decrease its lifetime up to almost 60% of its value when no buoyancy is present. By comparing the lifetimes using the shell and top BC it can be concluded that although the absolute droplet lifetime in an infinite matrix is bigger than an isolated one, the relative decrease due to convection is similar in the two cases.

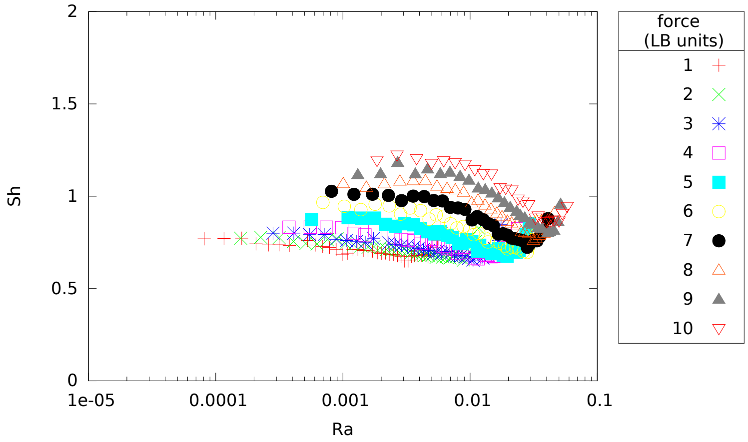

Figure 6.8: Sherwood number vs Rayleigh number for 2D hemispherical drops subject to top boundary conditions. The initial radius is 50 lattice units.

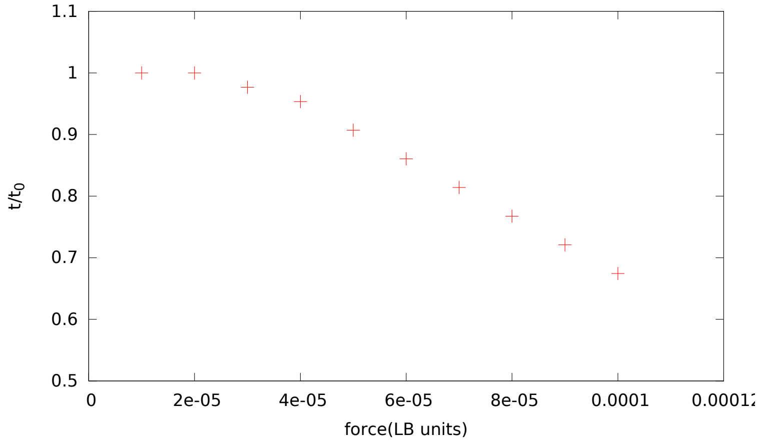

Figure 6.9: Lifetime of an evaporating droplet (with top BC) subject to a buoyant force (compared to the lifetime of the same droplet subject to no buoyancy) as a function of the force applied.

In order to further investigate the interplay between convection and the presence of multiple droplets we simulated a finite droplet matrix composed of three drops and subject to buoyancy. In this configuration we use side BC, *i.e.* the order parameter ϕ is fixed at the top and the sides of the domain (see Chapter 4 for a detailed explanation of these BC).

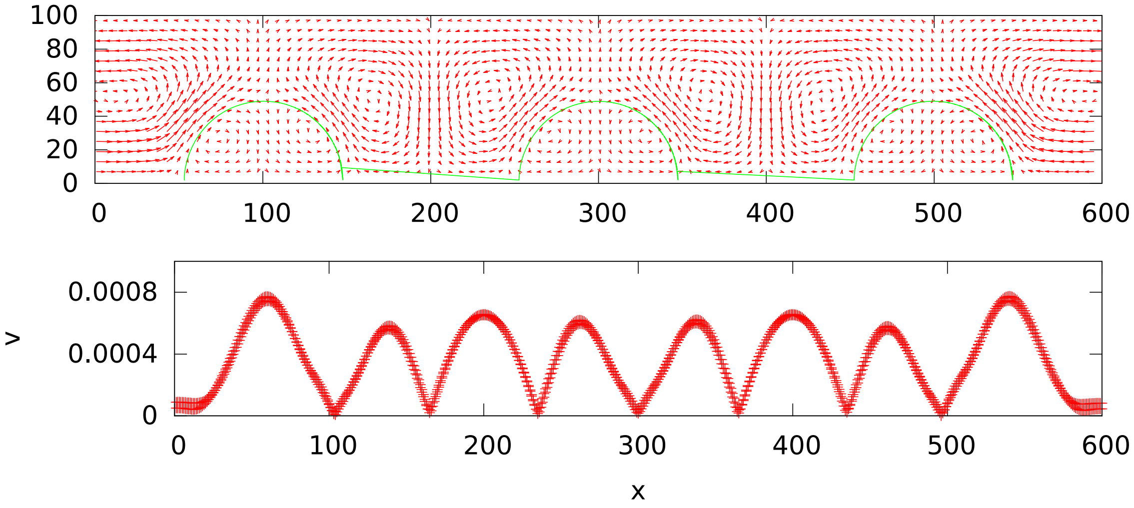

Figure 6.10: (top) Flow field of three evaporating droplets subject to buoyant forces and (bottom) magnitude of the velocity field at $z = N_z/2$.

Fig. 6.10 shows the flow field around the three droplets and its magnitude. The flow field near the central droplet is almost identical to the one observed for the infinite matrix case, while the external droplets are subject to an asymmetric flow. The magnitude of the flow field also indicates an almost identical flow field for the central droplet compared to the infinite matrix case and it also shows the bigger flow present on the outermost sides of the system.

Fig. 6.11 shows the Sh-Ra plot for such a configuration; it can be clearly seen that the external droplets dissolve quicker than the central one. Also in this case the Sherwood number is less than one because the theoretical value used is the one relative to a single drop.

The relative difference in lifetime between the external droplets and the central one is about 10%, in line with experimental observations of the dissolution of droplets matrices[1].

All the results presented show that buoyancy effects led to higher dissolution rates for droplets subject to evaporation. Even in the regime of low Rayleigh numbers, where

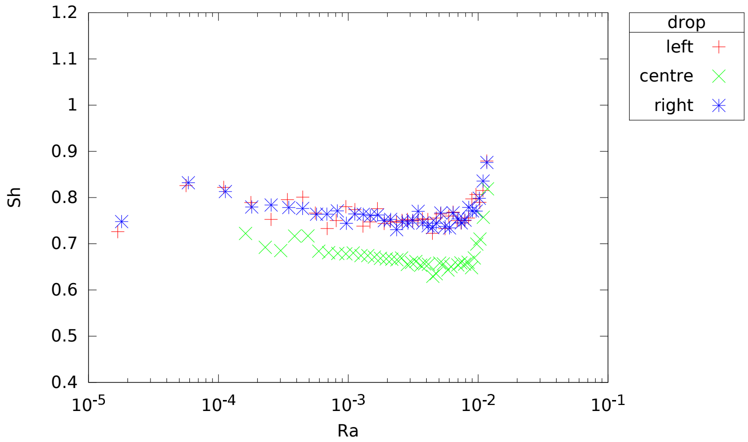

Figure 6.11: Sherwood number vs Rayleigh number for three hemispherical drops. The key refers to the drop's position.

diffusion is the dominant effect the resulting droplets' lifetimes can be reduced as much as 60%. These results are in broad qualitative agreement with the experimental measures shown in Fig. 1.9; for low values of the Rayleigh number different alcohols have a maximum variation of the Sherwood number of about a factor of two. However it is not possible to make any quantitative comparison due to statistical fluctuations in the experimental measurements.

6.1.1 3D droplets

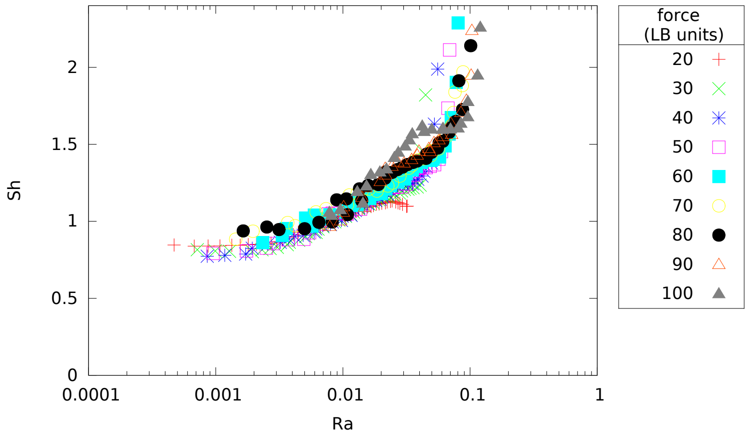

Figure 6.12: Sherwood number vs Rayleigh number for 3D hemispherical drops subject to shell boundary conditions. The initial radius is 30 lattice units.

We also simulated 3D evaporating droplets. For these simulations we used a system of size $(N_x, N_y, N_z) = (100, 100, 50)$ and an initial droplet radius $R_0 = 30$. Shell BC were used to fix the order parameter $\phi_H = -1.2$ to drive evaporation and buoyancy forces were implemented as in the 2D case. Fig. 6.12 shows the resulting Sh-Ra plot.

The results show that the Sherwood number increases for increasing Rayleigh numbers, although the Sh-Ra dependence is different than in the 2D case. However, the evaporation lifetime reduction, shown in Fig. 6.13 is very similar to the 2D case. It is worth mentioning that for the 3D case, since the droplet initial radius is about half the value of the 2D case, in order to achieve similar Rayleigh numbers we have to use a buoyancy force about one order of magnitude bigger than in the 2D case.

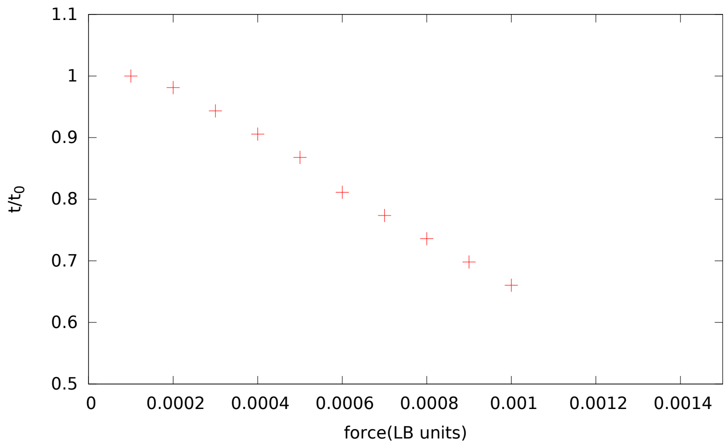

Figure 6.13: Lifetime of an evaporating 3D droplet (with shell BC) subject to a buoyant force (compared to the lifetime of the same droplet subject to no buoyancy) as a function of the force applied.

These results show that, apart from the different Sh-Ra dependence in 2D and 3D, the overall effect of buoyancy forces on evaporation is dependent only on the Rayleigh number. This is confirmed by the fact that the same Rayleigh number is obtained with different parameters in 2D and 3D as explained earlier, but as long as the Rayleigh number is the same, the evaporation lifetime reduction is essentially the same both in 2D and 3D.

6.2 External flows

Another mechanism that can affect evaporation is the presence of external flows. For example we can easily think of real world situations where external flows like winds can affect the evaporation of liquids. We simulated the effect of external flows on the evaporation on 2D droplets using the configuration sketched in Fig. 6.14. Buoyancy forces were not included in these simulations. We simulated a system of size $(N_x, N_z) = (200, 100)$ lattice units and an initial droplet radius of $R_0 = 50$. A body force is applied only in the upper part of the system, in the interval $z = [70, 100]$.

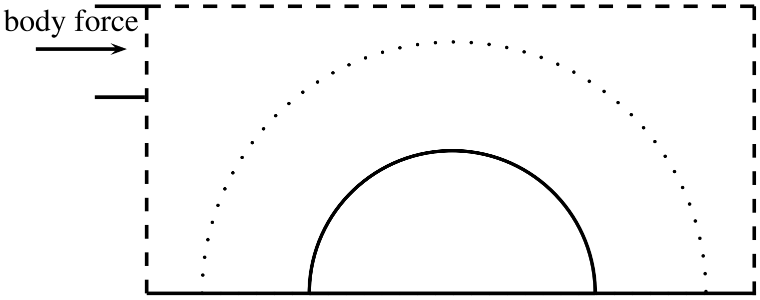

Figure 6.14: Simulation configuration for a 2D droplet subject to an external flow.

The resulting flow profile is shown in Fig. 6.15. In order to quantify the strength of the flow we still use the Rayleigh number, where the buoyancy force is now substituted by the body force applied.

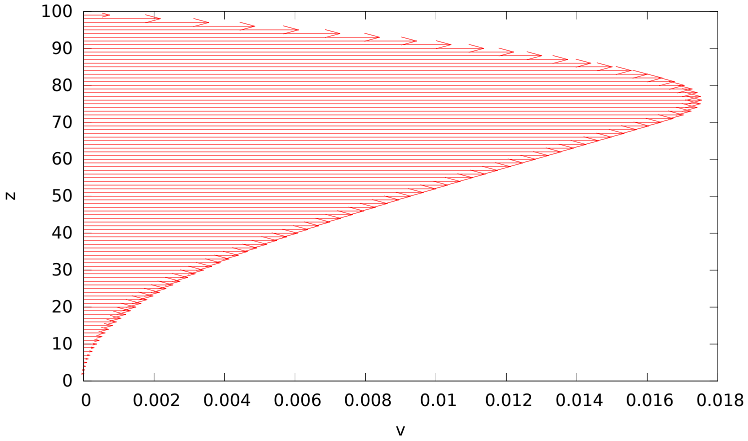

Figure 6.15: Flow field at $x = 2$ magnified by a factor of 10.

If implemented directly, a flow field like the one in Fig. 6.15 would make the drop move towards the right. In order to avoid this effect, we have fixed the velocity of the drop to zero. In this way any difference in the evaporation is solely due to the flow, and not due to the different position of the drop relative to the boundaries where the concentration is fixed.

Fig. 6.16 shows the Sh-Ra plot for this case, while Fig. 6.17 shows the relative lifetimes. The values of the Rayleigh number that can be reached in these simulations are about one order of magnitude smaller than the buoyancy flows presented in the previous section. The results show that an external flow can reduce the lifetime of an evaporating droplet by the same amount possible with buoyancy forces, but at a Rayleigh number one order of magnitude smaller than the buoyancy case.

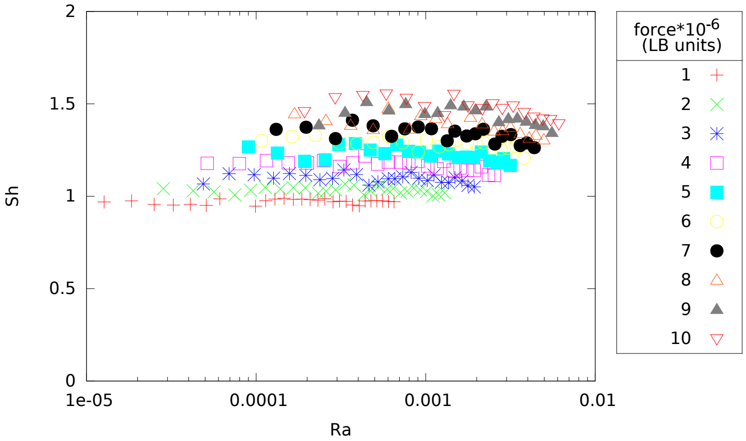

Figure 6.16: Sherwood number vs Rayleigh number for 2D hemispherical drops subject to an external flow. The Rayleigh number for this case is defined for the text.

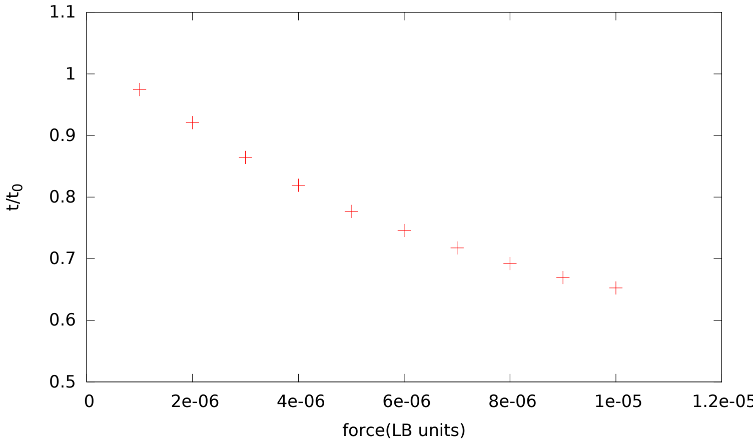

Figure 6.17: Lifetime of an evaporating droplet subject to an external flow as a function of the flow strength compared to the lifetime of a droplet subject to no flow.

The reason for this can be understood by looking at Fig. 6.18 where contour curves of the concentration field are plotted. If no buoyancy forces or external flow were present we would expect perfectly symmetrical contour curves. The contour curves show that buoyancy forces modify the concentration field by forming a little plume just

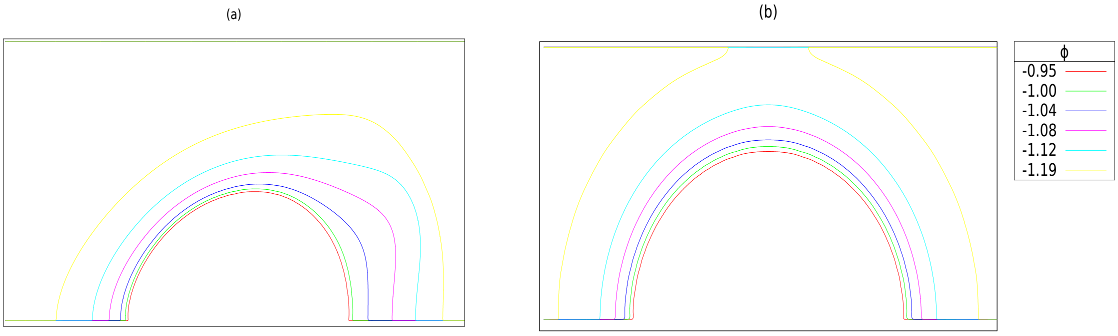

Figure 6.18: Contour curves of the order parameter ϕ around an evaporating droplet subject to an external flow (a) or buoyancy forces (b). $Ra \approx 0.1$ in both figures.

upward of the droplet, as it can be seen in the top center part of Fig. 6.18-(b). Along the plume itself the concentration gradient is diminished, because the plume is rich in vapour coming from the drop. An external flow, however, increases the concentration gradient almost everywhere (apart from the wake visible right of the drop because of the screening effect of the drop itself) because it moves “clean” fluid (i.e. fluid with no droplet’s vapour) towards the drop. This increase in the concentration gradient leads to an enhanced dissolution.

We have also simulated droplets subject to top BC and external flows (periodic BC are used on the domain’s sides). In this case the resulting Sh-Ra plot is showed in Fig. 6.19. The results show that no dependence of the dissolution dynamics on the flow is present in this case. Although counter-intuitive, this finding can be easily explained by looking at the concentration profile in Fig. 6.20. By applying top BC the concentration varies mainly along the vertical direction, thus any horizontal flow will not substantially modify the concentration gradient, and thus the dissolution dynamics (as long as the Rayleigh number is small). As a consequence the droplet lifetime is almost independent of the external flow for this configuration (data not shown).

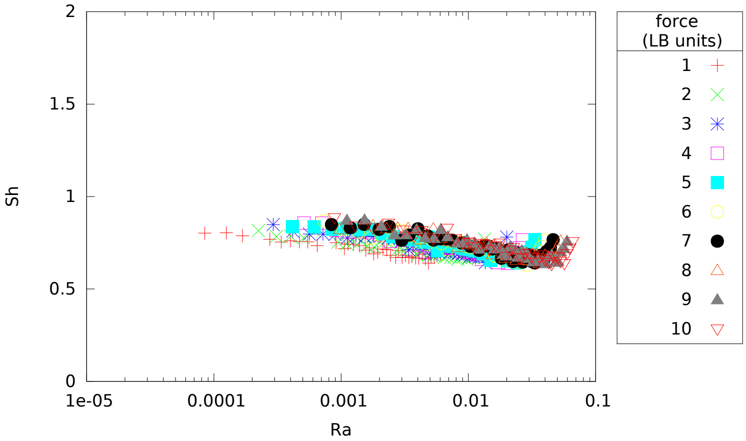

Figure 6.19: Sherwood number vs Rayleigh number for 2D hemispherical drops subject to an external flow and top BC.

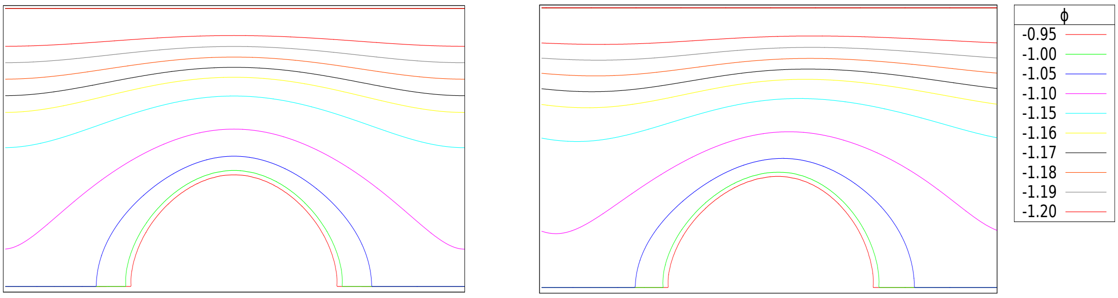

Figure 6.20: Contour curves of the order parameter ϕ around an evaporating droplet subject to no external flows (left) and external flows (right). Top BC are used.

6.3 Conclusions

In this chapter we have introduced a simulation method to model buoyancy forces in a binary fluid model where the two phases have the same densities. We have shown that these forces can considerably affect the lifetime of evaporating droplets. This is the case for both isolated drops and drops in the presence of neighbours.

We then modeled the effect of external flows on droplet evaporation. We have shown that also in this case a considerable reduction in the droplet lifetime is attainable at low values of the Rayleigh number.

By comparing these two different mechanisms, we have concluded that the same reduction in evaporation lifetimes is attainable with an external flow at values of the

Rayleigh number one order of magnitude smaller than the ones needed for buoyancy forces.

We have also studied the effect of the presence of multiple droplets evaporating together (in the limit of an infinite matrix of droplets) by using different boundary conditions. We have shown that if buoyancy forces are present the effect of other droplets is to extend the absolute drop evaporation lifetime, but the relative decrease due to flow is not modified. For external flows, however, the presence of neighbouring droplets does not have an appreciable effect on the dissolution lifetime, because the concentration profile is not modified by the presence of the flow.

Conclusions

The study of evaporation phenomena is having a resurgent interest in recent years. This is due to its applications in many industrial processes, such as printing and coating and new technologies like microfluidics. New experimental techniques have also enabled the study of droplets down to the nanometer scale, opening up new fields of study.

In this thesis we have shown that the Lattice Boltzmann method is an ideal candidate for the simulation of evaporation phenomena; its mesoscopic nature is a particularly useful feature to study fluids at the micrometer scale down to the nanometer scale. Furthermore the modeling of evaporation with the free energy approach has a clear physical interpretation.

After a general introduction of evaporation dynamics and droplets in Chapter 1, in Chapter 2 we have described the principles of the Lattice Boltzmann method, the free energy approach to model multiphase flows and the implementation of evaporation in this context. We have then validated numerical simulations against theoretical predictions of evaporation of simple systems in Chapter 3, and we have applied these numerical techniques to different systems where it is not possible to obtain analytical results.

In Chapter 4 we have studied the evaporation dynamics of matrices of droplets. In most practical applications there are multiple droplets evaporating together, and the interaction between them can lead to modifications to their evaporation dynamics compared to the single droplet case. We have shown that the presence of other droplets can slow down evaporation lifetimes up to 60% compared to the single droplet case. We also have compared numerical results with real experiments, noting a good qualitative agreement between the two. Eperimental results have also shown that convective effects are important in the evaporation dynamics, and in general there is a competition between convective effects and collective effects. The first ones tend to accelerate evaporation while the second ones tend to slow it down.

In Chapter 5 we have analyzed the stability of a liquid front in a confined geometry subject to evaporation. In this system the interplay between capillary effects, variable wettability and phase changes can lead to the destabilization of the liquid front. Beyond its theoretical interest, this problem has numerous applications; for example microfabrication techniques involve the evaporation of solvents and this can led to the rupture of the fabricated microstructures. We have developed a 2D theory to predict the instability behaviour of the system. We then have used LB simulations to extend our analysis to three dimensions.

In Chapter 6 we have analyzed the effect of flows on the evaporation dynamics of droplets. We have implemented both buoyancy driven flows and external flows. The results obtained show that flow effects can be non negligible even in situations where the diffusion is dominant over the flow.

Our results show that the LB method is a very versatile technique to model evaporation and can be used to model many systems of practical interest when it is not possible to develop theoretical predictions. Future work can extend the current model to include density differences between the two phases and to explore systems with stronger flows.

APPENDIX A

Linear stability analysis

In this appendix we derive Eq. 5.15 using linear stability analysis techniques. We first consider the case of constant wetting properties ($\theta(x) = \theta_0$), negligible gas viscosity and a tapering channel gradient β (i.e. the channel height is $h(x) = h_0 + \beta(x - x_0)$). We then incorporate variable wetting properties and finite gas viscosity in the analysis. We also discuss the pattern formation deriving from this instability.

A.1 Small perturbation

We consider the effect of a small perturbation that shifts the position of the interface, i.e., $l = x_0 + x_p$, where

$$x_p = \epsilon(t)\cos(ky), \tag{A.1}$$

$\epsilon \ll 2/k$ is the amplitude of the deformation and k is the wavenumber. For $\epsilon \ll 2/k$, the normal vector to the interface is $\hat{\mathbf{n}} \approx \hat{\mathbf{x}} - \partial_y x_p \hat{\mathbf{y}}$. Therefore, to leading order in ϵ

the normal interface speed is

$$\mathbf{v}_i \cdot \hat{\mathbf{n}} = (E_0 + \dot{x}_p)\hat{\mathbf{x}} \tag{A.2}$$

where

$$\dot{x}_p = \dot{\epsilon}\cos(ky). \tag{A.3}$$

We assume that the pressure and concentration fields respond with corresponding perturbations, so that

$$p = p_0 + \delta p(t)\cos(ky)p_1(x), \tag{A.4}$$

and

$$c = c_0 + \delta c(t)\cos(ky)c_1(x), \tag{A.5}$$

where δp and δc are small amplitudes and the spatial parts obey $p_1(x \to +\infty) = 0$ and $c_1(x \to -\infty) = 0$.

Inserting the pressure ansatz into Eq. 5.10 gives the solution for p_1 :

$$p_1(x) = \exp(-\Pi(x - x_0)). \tag{A.6}$$

where

$$\Pi = \frac{3\beta}{2h_0}\left(1 + \frac{\beta}{|\beta|}\sqrt{1 + \left(\frac{2h_0 k}{3\beta}\right)^2}\right) \approx \frac{\beta|k|}{|\beta|} \tag{A.7}$$

for $\beta k/h_0 \ll 1$, as required. Note that this solution always decays for $x \gg x_0$ provided that $\beta > 0$. Inserting the ansatz for the concentration into Eq. 5.4 gives the solution for c_1 :

$$c_1(x) = \exp(k(x - x_0)), \tag{A.8}$$

which decays for $x \ll x_0$ as required.

The Young-Laplace condition can be used to link $\delta p(t)$ and $\epsilon(t)$, i.e.,

$$\delta p(t) = \gamma \left(\frac{2\cos(\theta_0)\beta}{h_0^2} - k^2 \right) \epsilon(t) \tag{A.9}$$

where we have omitted higher-order terms in ϵ and β. The boundary condition for the concentration field, $c(x_i, y) = c_{sat}$, can be used to determine $\delta c(t)$, i.e.,

$$\delta c(t) = -\frac{c_{sat} - c_g}{x_0(t)} \epsilon(t) \tag{A.10}$$

The kinematic boundary condition (Eq. A.2) is then used to find the speed of the interface,

$$\dot{\epsilon} = \frac{h_0^2}{12\eta} \Pi \delta p(t) + \frac{D}{\rho} k \delta c(t), \tag{A.11}$$

or

$$\dot{\epsilon} = \left[\frac{\gamma h_0^2}{12\eta} \left(\frac{2\cos(\theta_0)\beta}{h_0^2} - k^2 \right) \Pi(k) - E_0 k \right] \epsilon \tag{A.12}$$

This equation has the solution

$$\epsilon(t) = \epsilon_0 exp(\sigma t), \tag{A.13}$$

where

$$\sigma(k) = \frac{\gamma h_0^2}{12\eta}\left(\frac{2\cos(\theta_0)\beta}{h_0^2} - k^2\right)\Pi(k) - E_0 k \tag{A.14}$$

is the dispersion relation, which can be non-dimensionalised to give

$$\hat{\sigma}(\hat{k}) = Ca^{-1}\left\{2\cos(\theta_0)\beta - \hat{k}^2\right\}\hat{\Pi}(\hat{k}) - \hat{k} \tag{A.15}$$

or

$$\hat{\sigma}(\hat{k}) = Ca^{-1}\left\{2\cos(\theta_0)\beta - \hat{k}^2\right\}\frac{\beta|\hat{k}|}{|\beta|} - \hat{k} \tag{A.16}$$

where $Ca \equiv 12E_0\eta/\gamma$, $\hat{\Pi} \equiv \Pi h_0$, $\hat{\sigma} \equiv \sigma h_0/E_0$ and $\hat{k} \equiv kh_0$.

A.2 Discussion

The dispersion relation of our problem reads

$$\hat{\sigma}(\hat{k}) = Ca^{-1}\left\{2\cos(\theta_0)\beta - \hat{k}^2\right\}\frac{\beta|\hat{k}|}{|\beta|} - \hat{k} \tag{A.17}$$

The term $\propto \beta$ arises from the gradient of transverse curvature and is destabilising provided that $\beta > 0$. The second term, $\propto \hat{k}^2$, is the usual stabilising capillary term in

Hele-Shaw flows. The final term arises from concentration gradients, and is stabilising for an evaporating front. The first thing to notice is that this dispersion relation is different from the Saffman-Taylor dispersion relation[137],

$$\sigma(k) = \frac{\gamma}{12\eta h_0}\left(Ca_U - \hat{k}^2\right)|\hat{k}|, \tag{A.18}$$

where $Ca_U \equiv 12\eta U/\gamma$ is the capillary number based on the base-state interface velocity U. In the Saffman-Taylor problem the instability is driven at higher Ca_U , whereas in the evaporating front the tendency seems to be the opposite. Interestingly, our result suggests that the fronts can destabilise even at $Ca = 0$, through a mechanism controlled solely by capillarity. The main features of the dispersion relation are

1. The destabilising mechanism arises from gradients in the capillary pressure, which drive fluid from the wider portion of the channel (where the capillary pressure due to transverse curvature is higher) to the narrower portions.

2. The instability occurs for wetting fluids ($\theta_0 < \pi/2$) occupying the wider portion of the channel ($\beta > 0$); by symmetry we would expect that the instability occurs for non-wetting fluids at $\beta < 0$. (This is the case according to the dispersion relation).

3. The evaporation rate only delays the instability, by reducing the amplitude of the peaks (which lie in the more narrow portion of the channel) relative to the troughs.

4. The instability is favoured in the case of a condensing front, $E_0 < 0$, even for straight channels, $\beta = 0$. In this case the dispersion relation reduces to a form similar to the Saffman-Taylor dispersion relation,

$$\sigma(\hat{k}) \propto Ca\,\hat{k} - \hat{k}^2|\hat{k}| \tag{A.19}$$

In this case the mechanism driving the instability is the local gradient of concentration: peaks lie closer to the plane $c(x_0, y) = c_0$, and therefore have a faster condensation rate, driving the growth of perturbations.

A.3 Ripening and pattern formation

Since the average position of the interface is increasing, the local thickness $h(x_0)$ gets larger over time, at a rate

$$\dot{h}(x_0) = \beta E_0, \tag{A.20}$$

where

$$E_0 = \dot{x}_0 = \frac{D}{\rho}\frac{c_{sat} - c_g}{x_0}. \tag{A.21}$$

At long times (when $|x_0| \gg 0$) it is safe to impose $x_0(t = 0) = 0$; we therefore have

$$x_0 = \sqrt{\frac{2D(c_{sat} - c_g)t}{\rho}}, \tag{A.22}$$

$$E_0 = \sqrt{\frac{D(c_{sat} - c_g)}{2\rho t}} \tag{A.23}$$

and

$$h(x_0) = h_0 + \beta\sqrt{\frac{2D(c_{sat} - c_g)t}{\rho}}. \tag{A.24}$$

From the dispersion relation, the first unstable mode is

$$k_n = \frac{1}{h_0}(2\beta \cos\theta_0 - Ca)^{1/2}, \tag{A.25}$$

For $k_n > 0$, we require that the inclination gradient exceeds a critical value

$$\beta_c > \frac{Ca}{2\cos\theta_0}. \tag{A.26}$$

However, $Ca \propto E_0 \sim t^{1/2}$. This means that the instability will eventually set in. However, since $h(x_0)$ also increases with time, the range of unstable modes decreases at long times. One may speculate that once the front is destabilised, the emerging pattern will be dominated by the fastest growing mode, given by

$$k_{max} = \frac{1}{\sqrt{3}}k_n. \tag{A.27}$$

Given the time dependence discussed above we expect that the pattern coarsens over time.

A.4 Straight channel with chemical gradient

As previously discussed, the destabilising mechanism arises from gradients in the capillary pressure, which originates from the taper of the channel. The same mechanism arises in a straight channel with fixed width h_0 and varying wetting properties along it. We assume that the wetting contact angle varies along the x axis according to

$$\theta(x) = \theta_0 + \alpha(x - x_0), \tag{A.28}$$

where $\theta_0 = \theta(x_0)$; if $\alpha > 0$ the channel is more hydrophilic at $x = 0$ and more hydrophobic at its right end. Consequently if the liquid fills the channel as shown in Fig. 5.1, it will be driven towards the left part of it.

In this case the curvature is

$$\kappa(x) = \frac{2\cos\theta(x)}{h_0} \sim \frac{2}{h_0}(\cos\theta_0 - \alpha x \sin\theta_0) \tag{A.29}$$

if $\alpha \ll 1$. The linear stability analysis is the same as the previuos case and it leads to a dispersion relation of the form

$$\sigma(k) = k\left[\frac{\gamma h_0^2}{12\eta}\left(\frac{2\alpha\sin\theta_0}{h_0} - k^2\right) - E_0\right] \tag{A.30}$$

and in its non-dimensionalised form

$$\hat{\sigma}(\hat{k}) = \hat{k}\left[Ca^{-1}\left(2\alpha h_0\sin\theta_0 - \hat{k}^2\right) - 1\right] \tag{A.31}$$

The same conclusions discussed in Sec. A.2 hold here, provided that now α plays the role of β.

A.5 Effects of finite gas viscosity

If the gas has a finite viscosity η_g we can solve the Stokes equation for the gas phase in the same way as for the liquid phase (as done in Chap. 5). For the gas velocities we get

$$v_{x,g} = -\frac{h^2}{12\eta_g}\partial_x p_g, \tag{A.32}$$

and

$$v_{y,g} = -\frac{h^2}{12\eta_g}\partial_x p_g. \tag{A.33}$$

The jump in the pressure at the interface is now given by

$$p_l(x_i, y_i) = p_g(x_i, y_i) - \gamma\kappa. \tag{A.34}$$

The linear stability analysis can be carried out in this case too; the resulting dispersion relation for the case of a straight channel with a chemical gradient is

$$\sigma(k) = k\left[\frac{\gamma h_0^2}{12(\eta_g + \eta_l)}\left(\frac{2\alpha\sin\theta_0}{h_0} - k^2\right) - E_0\right] \tag{A.35}$$

which reduces to Eq. A.30 in the limit $\eta_g \to 0$.

If the interface has an additional velocity V not due to evaporation (i.e., due to gravity), then there will be an addition term in the dispersion relation proportional to $V(\eta_g - \eta_l)$ (the derivation is the same as in the standard Saffman-Taylor instability) and Eq. A.35 becomes

$$\sigma(k) = k\left[\frac{\gamma h_0^2}{12(\eta_g + \eta_l)}\left(\frac{2\gamma\alpha\sin\theta_0}{h_0} - \gamma k^2 + V(\eta_g - \eta_l)\right) - E_0\right] \tag{A.36}$$

A.6 Tapered channel with chemical gradient and evaporation

We can consider the general case of a tapered channel with a varying contact angle. In this case the curvature is

$$\kappa(x) = \frac{2\cos\theta(x) - \beta/2}{h(x)}. \tag{A.37}$$

The linear stability analysis can be carried out in this case too (in the linear limit the two effects simply add together) and we have for the dispersion relation

$$\sigma(k) = k\left[\frac{\gamma h_0^2}{12(\eta_g+\eta_l)}\left(\frac{2\alpha\sin\theta_0}{h_0} + \frac{2\cos(\theta_0)\beta}{h_0^2} - k^2\right) - E_0\right] \tag{A.38}$$

which can be dimensionalised to give

$$\hat{\sigma}(\hat{k}) = \hat{k}(Ch + Ta - Ca) - \hat{k}^3 \tag{A.39}$$

which is Eq. 5.16; the different terms are

$$\begin{aligned} Ca &= 12E_0\eta_t/\gamma & \eta_t &= \eta_l + \eta_g \\ \hat{\sigma} &= 12\eta_t h_0\sigma/\gamma & \hat{k} &= kh_0 \\ Ch &= 2\alpha h_0\sin\theta_0 & Ta &= 2\cos(\theta_0)\beta. \end{aligned}$$

In Eq. A.39 we can clearly see the effect of each physical phenomenom on the instability: the taper and the chemical gradient destabilize the interface, while evaporation stabilise it (but destabilise it if there is condensation). We can also derive the critical wavenumber for the onset of instability

$$k_{crit} = \frac{1}{h_0}(Ch + Ta - Ca)^{1/2}. \tag{A.40}$$

As in Eq. A.26, in order to have $k_{crit} > 0$ we need to satisfy the condition

$$Ch + Ta - Ca > 0. \tag{A.41}$$

APPENDIX B

Lubrication theory

Lubrication theory studies flows in confined geometries where one length scale is much smaller than the others. The name lubrication comes from the observation that thin layers of fluid can prevent solid bodies from contact, thus reducing friction.

Let us consider a solid plane at $z = 0$ and a solid body at height $z = h(x, y, t)$. We are interested in the situation of h being much smaller than the length scale L in the x and y direction. We write the velocity field $\mathbf{u} = (u, v, w)$, where u and v have typical scales U_0 and w has typical scale W_0. Considering incompressible fluids, the continuity equation is

$$\partial_x u + \partial_y v + \partial_z w = 0 \tag{B.1}$$

and suggests that the velocity W_0 is much smaller than U_0

$$W_0 \approx U_0 h/L \ll U_0. \tag{B.2}$$

The x component of the Navier-Stokes equation is

$$\rho(\partial_t u + u\partial_x u + v\partial_y u + w\partial_z u) = -\partial_x p + \mu(\partial_x^2 u + \partial_y^2 u + \partial_z^2 u). \tag{B.3}$$

In lubrication theory we are interested in the small Reynolds number regime, i.e. in the regime where inertia is negligible. This translates to neglecting the left hand side in Eq. B.3. In this limit pressure scales as

$$P \approx \frac{\mu U_0 L}{h^2}. \tag{B.4}$$

Noting also that in Eq. B.3 the z-derivatives dominate, we have

$$\begin{aligned} \partial_x p &= \mu \partial_z^2 u \\ \partial_y p &= \mu \partial_z^2 v \\ p &= 0 \end{aligned} \tag{B.5}$$

which is easily solved to give

$$\begin{aligned} p &= p(x,y,t) \\ u &= \frac{\partial_x p}{2\mu}(z^2 + Az + B) \\ v &= \frac{\partial_y p}{2\mu}(z^2 + Cz + D). \end{aligned} \tag{B.6}$$

We now impose the boundary conditions $\mathbf{u} = 0$ at $z = 0$ and $\mathbf{u} = (U_0, V_0, W_0)$ at $z = h$. This gives

$$\begin{aligned} u &= \frac{\partial_x p}{2\mu}(z^2 - zh) + \frac{U_0 z}{h} \\ v &= \frac{\partial_y p}{2\mu}(z^2 - zh) + \frac{V_0 z}{h}. \end{aligned} \tag{B.7}$$

In the following we use the identity

$$\frac{\partial}{\partial x}\int_0^{h(x,y,t)} u(x,y,z,t)dz = \int_0^h \frac{\partial u}{\partial x}dz + u(x,y,h,t)\frac{\partial h}{\partial x} = \int_0^h \partial_x u dz + U_0 \partial_x h \tag{B.8}$$

and similar identities can be written for v and w. Using these identities in the continuity equation we get

$$W_0 = \int_0^h \partial_z w dz = -\int_0^h (\partial_x u + \partial_y v) dz = -\frac{\partial}{\partial x}\int_0^h u dz - \frac{\partial}{\partial y}\int_0^h v dz + U_0 \partial_x h + V_0 \partial_y h. \tag{B.9}$$

Inserting Eq. B.7 in Eq. B.9 and integrating over z we have

$$\frac{1}{12\mu}\left(\frac{\partial}{\partial x}(h^3 \partial_x p) + \frac{\partial}{\partial y}(h^3 \partial_y p)\right) = W_0 - \frac{1}{2}U_0 \partial_x h - \frac{1}{2}V_0 \partial_y h \tag{B.10}$$

which is called Reynolds' lubrication equation. We can write it in a more compact form by using the identity

$$0 = \frac{D}{Dt}(z - h(x,y,t)) = -\partial_t h + w - u\partial_x h - v\partial_y h = -\partial_t h + W_0 - U_0 \partial_x h - V_0 \partial_y h \tag{B.11}$$

where D/Dt is the material derivative.

Eq. B.10 can then be rewritten as

$$\nabla \cdot (h^3 \nabla p) = 6\mu(\partial_t h + W_0) \tag{B.12}$$

B.1 Hele-Shaw flow

If h is constant and $U_0 = V_0 = W_0 = 0$ we have a flow between two rigid plates which is called Hele-Shaw flow. Eq. B.12 in this case reduces to

$$\begin{aligned} &\nabla^2 p = 0 \\ &< u > = -\frac{\partial_x p}{12\mu} \\ &< v > = -\frac{\partial_y p}{12\mu} \end{aligned} \tag{B.13}$$

where <> indicates an average over z. These equations together with Eq. B.10 are used in Chapter 5.

References

[1] G. Laghezza, E. Dietrich, J. M. Yeomans, R. Ledesma-Aguilar, E. S. Kooij, H. J. W. Zandvliet, and D. Lohse. Soft Matter, 12:5787–5796, 2016. doi:10.1039/C6SM00767H. URL `http://dx.doi.org/10.1039/C6SM00767H`.

[2] H. G. Houghton. Journal of Applied Physics, 4(12), 1933.

[3] M. L. Blow. Wetting on flexible and anisotropic surfaces. PhD thesis, University of Oxford, 2010.

[4] X. Zhang, J. Wang, L. Bao, E. Dietrich, R. C. A. van der Veen, S. Peng, J. Friend, H. J. W. Zandvliet, L. Yeo, and D. Lohse. Soft Matter, 11:1889–1900, 2015.

[5] R. Deegan, O. Bakajin, T. Dupont, G. Huber, S. Nagel, and T. Witten. Nature, 389(6653):827–829, 1997.

[6] N. Shahidzadeh-Bonn, S. Rafai, A. Azouni, and D. Bonn. Journal of Fluid Mechanics, 549:307–313, 2 2006. ISSN 1469-7645. doi:10.1017/S0022112005008190. URL `http://journals.cambridge.org/article_S0022112005008190`.

[7] E. Dietrich, S. Wildeman, C. W. Visser, K. Hofhuis, E. S. Kooij, H. J. W. Zandvliet, and D. Lohse. Journal of Fluid Mechanics, 794:45–67, 5 2016. ISSN 1469-7645. doi:10.1017/jfm.2016.158. URL `http://journals.cambridge.org/article_S0022112016001580`.

[8] E. Dietrich, S. Wildeman, C. W. Visser, K. Hofhuis, E. S. Kooij, H. J. W. Zandvliet, and D. Lohse. accepted for publication in J. Fluid Mech., (in press), 2016.

[9] R. D. Deegan, O. Bakajin, T. F. Dupont, G. Huber, S. R. Nagel, and T. A. Witten. Phys. Rev. E, 62:756–765, Jul 2000. doi:10.1103/PhysRevE.62.756. URL `http://link.aps.org/doi/10.1103/PhysRevE.62.756`.

[10] S. Maheshwari, L. Zhang, Y. Zhu, and H.-C. Chang. Phys. Rev. Lett., 100:044503, Jan 2008. doi:10.1103/PhysRevLett.100.044503. URL `http://link.aps.org/doi/10.1103/PhysRevLett.100.044503`.

[11] Y. O. Popov. Phys. Rev. E, 71:036313, Mar 2005. doi:10.1103/PhysRevE.71.036313. URL http://dx.doi.org/10.1103/PhysRevE.71.036313.

[12] A. G. Marin, H. Gelderblom, D. Lohse, and J. H. Snoeijer. Phys. Rev. Lett., 107:085502, Aug 2011. doi:10.1103/PhysRevLett.107.085502. URL http://dx.doi.org/10.1103/PhysRevLett.107.085502.

[13] P. S. Epstein and M. S. Plesset. J. Chem. Phys., 18:1505–1509, 1950.

[14] R. Picknett and R. Bexon. Journal of Colloid and Interface Science, 61(2):336 – 350, 1977. ISSN 0021-9797. doi:http://dx.doi.org/10.1016/0021-9797(77)90396-4. URL http://dx.doi.org/10.1016/0021-9797(77)90396-4.

[15] A.-M. Cazabat and G. Guena. Soft Matter, 6:2591–2612, 2010. doi:10.1039/B924477H. URL http://dx.doi.org/10.1039/B924477H.

[16] H. Y. Erbil. Adv. Colloid Interface Sci., 170:67–86, 2012.

[17] P. Tabeling. Current Opinion in Biotechnology, 25(0):129 – 134, 2014. ISSN 0958-1669. doi:http://dx.doi.org/10.1016/j.copbio.2013.11.009. Analytical biotechnology.

[18] R. Enright, N. Miljkovic, A. Al-Obeidi, C. V. Thompson, and E. N. Wang. Langmuir, 28(40):14424–14432, 2012. doi:10.1021/la302599n. URL http://dx.doi.org/10.1021/la302599n. PMID: 22931378.

[19] G. McHale, S. Aqil, N. J. Shirtcliffe, M. I. Newton, , and H. Y. Erbil. Langmuir, 21(24):11053–11060, 2005. doi:10.1021/la0518795. URL http://dx.doi.org/10.1021/la0518795. PMID: 16285771.

[20] X. Zhang, S. Tan, N. Zhao, X. Guo, X. Zhang, Y. Zhang, and J. Xu. ChemPhysChem, 7(10):2067–2070, 2006. ISSN 1439-7641. doi:10.1002/cphc.200600229. URL http://dx.doi.org/10.1002/cphc.200600229.

[21] S. Tan, X. Zhang, N. Zhao, and J. Xu. Chinese Journal of Chemical Physics, 20 (2), 2007.

[22] M. L. McLauchlin, D. Yang, P. Aella, A. A. Garcia, S. T. Picraux, and M. A.

Hayes. Langmuir, 23(9):4871–4877, 2007. doi:10.1021/la062638f. URL `http://dx.doi.org/10.1021/la062638f`. PMID: 17381139.

[23] Y. C. Jung and B. Bhushan. Journal of Microscopy, 229(1):127–140, 2008. ISSN 1365-2818. doi:10.1111/j.1365-2818.2007.01875.x. URL `http://dx.doi.org/10.1111/j.1365-2818.2007.01875.x`.

[24] M. Reyssat, J. M. Yeomans, and D. Quere. EPL (Europhysics Letters), 81(2):26006, 2008. URL `http://stacks.iop.org/0295-5075/81/i=2/a=26006`.

[25] N. Anantharaju, M. Panchagnula, and S. Neti. Journal of Colloid and Interface Science, 337(1):176 – 182, 2009. ISSN 0021-9797. doi:http://dx.doi.org/10.1016/j.jcis.2009.04.095. URL `http://www.sciencedirect.com/science/article/pii/S0021979709005578`.

[26] S. Farhadi, M. Farzaneh, and S. Kulinich. Applied Surface Science, 257(14):6264 – 6269, 2011. ISSN 0169-4332. doi:http://dx.doi.org/10.1016/j.apsusc.2011.02.057. URL `http://www.sciencedirect.com/science/article/pii/S0169433211002480`.

[27] T.-S. Wong and C.-M. Ho. Langmuir, 25(22):12851–12854, 2009. doi:10.1021/la902430w. URL `http://dx.doi.org/10.1021/la902430w`. PMID: 19842620.

[28] D. H. Shin, S. H. Lee, J.-Y. Jung, and J. Y. Yoo. Microelectronic Engineering, 86(4-6):1350 – 1353, 2009. ISSN 0167-9317. doi:http://dx.doi.org/10.1016/j.mee.2009.01.026. URL `http://www.sciencedirect.com/science/article/pii/S0167931709000525`. MNE 08 The 34th International Conference on Micro- and Nano-Engineering (MNE).

[29] D. H. Shin, T. Shokuhfar, C. K. Choi, S.-H. Lee, and C. Friedrich. Nanotechnology, 22(31):315704, 2011. URL `http://stacks.iop.org/0957-4484/22/i=31/a=315704`.

[30] P. M. Hansson, L. Skedung, P. M. Claesson, A. Swerin, J. Schoelkopf, P. A. C. Gane, M. W. Rutland, and E. Thormann. Langmuir, 27(13):8153–8159, 2011. doi:10.1021/la201121p. URL `http://dx.doi.org/10.1021/la201121p`. PMID:

21667955.

[31] H. Y. Erbil and C. E. Cansoy. Langmuir, 25(24):14135–14145, 2009. doi:10.1021/la902098a. URL `http://dx.doi.org/10.1021/la902098a`. PMID: 19630435.

[32] C. E. Cansoy, H. Y. Erbil, O. Akar, and T. Akin. Colloids and Surfaces A: Physicochemical and Engineering Aspects, 386(1-3):116 – 124, 2011. ISSN 0927-7757. doi:http://dx.doi.org/10.1016/j.colsurfa.2011.07.005. URL `http://www.sciencedirect.com/science/article/pii/S0927775711004390`.

[33] M. Gross, F. Varnik, D. Raabe, and I. Steinbach. Phys. Rev. E, 81:051606, May 2010. doi:10.1103/PhysRevE.81.051606. URL `http://link.aps.org/doi/10.1103/PhysRevE.81.051606`.

[34] G. McHale, N. J. Shirtcliffe, and M. I. Newton. Analyst, 129:284–287, 2004. doi:10.1039/B400567H. URL `http://dx.doi.org/10.1039/B400567H`.

[35] F. Varnik, M. Gross, N. Moradi, G. Zikos, P. Uhlmann, P. Muller-Buschbaum, D. Magerl, D. Raabe, I. Steinbach, and M. Stamm. Journal of Physics: Condensed Matter, 23(18):184112, 2011. URL `http://stacks.iop.org/0953-8984/23/i=18/a=184112`.

[36] P. Tsai, R. G. H. Lammertink, M. Wessling, and D. Lohse. Phys. Rev. Lett., 104:116102, Mar 2010. doi:10.1103/PhysRevLett.104.116102. URL `http://link.aps.org/doi/10.1103/PhysRevLett.104.116102`.

[37] H. Gelderblom, A. G. Marin, H. Nair, A. van Houselt, L. Lefferts, J. H. Snoeijer, and D. Lohse. Phys. Rev. E, 83:026306, Feb 2011. doi:10.1103/PhysRevE.83.026306. URL `http://link.aps.org/doi/10.1103/PhysRevE.83.026306`.

[38] J. Long and P. Chen. Langmuir, 17(10):2965–2972, 2001. doi:10.1021/la001547u. URL `http://dx.doi.org/10.1021/la001547u`.

[39] J. C. Crocker and D. G. Grier. Journal of Colloid and Interface Science, 179(1): 298 – 310, 1996. ISSN 0021-9797. doi:http://dx.doi.org/10.1006/jcis.1996.0217. URL `http://www.sciencedirect.com/science/article/pii/`

S0021979796902179.

[40] L. Landau and E. Lifshitz. Fluid Mechanics. Number v. 6. Elsevier Science, 2013. ISBN 9781483140506. URL https://books.google.co.uk/books?id=CeBbAwAAQBAJ.

[41] E. Fermi. Thermodynamics. Dover books in physics and mathematical physics. Dover Publications, 1956. ISBN 9780486603612. URL https://books.google.co.uk/books?id=VEZ1ljsT3IwC.

[42] In R. Bradley and N. Fuchs, editors, Evaporation and Droplet Growth in Gaseous Media. Pergamon, 1959. ISBN 978-1-4832-0060-6. doi:http://dx.doi.org/10.1016/B978-1-4832-0060-6.50001-6. URL http://www.sciencedirect.com/science/article/pii/B9781483200606500016.

[43] T. Young. Philosophical Transactions of the Royal Society of London, 95:65–87, 1805. doi:10.1098/rstl.1805.0005. URL http://rstl.royalsocietypublishing.org/content/95/65.short.

[44] A. Mendez-Vilas, A. B. Jodar-Reyes, and M. L. Gonzalez-Martin. Small, 5(12): 1366–1390, 2009. ISSN 1613-6829. doi:10.1002/smll.200800819. URL http://dx.doi.org/10.1002/smll.200800819.

[45] D. Quere. Nature Materials, 3(2):79–80, 2 2004. ISSN 1476-1122. doi:10.1038/nmat1062. URL http://dx.doi.org/10.1038/nmat1062.

[46] A. Ma, J. Xu, L. Yu, X. Zhang, D. Wang, and H. Xu. Chem. Commun., 49: 11563–11565, 2013. doi:10.1039/C3CC47509C. URL http://dx.doi.org/10.1039/C3CC47509C.

[47] T. Pompe and S. Herminghaus. Phys. Rev. Lett., 85:1930–1933, Aug 2000. doi:10.1103/PhysRevLett.85.1930. URL http://link.aps.org/doi/10.1103/PhysRevLett.85.1930.

[48] M. Hampton and A. Nguyen. Advances in Colloid and Interface Science, 154(1-2): 30 – 55, 2010. ISSN 0001-8686. doi:http://dx.doi.org/10.1016/j.cis.2010.01.006. URL http://www.sciencedirect.com/science/article/pii/S0001868610000084.

[49] J. R. T. Seddon and D. Lohse. Journal of Physics: Condensed Matter, 23(13): 133001, 2011. URL `http://stacks.iop.org/0953-8984/23/i=13/a=133001`.

[50] V. S. J. Craig. Soft Matter, 7:40–48, 2011. doi:10.1039/C0SM00558D. URL `http://dx.doi.org/10.1039/C0SM00558D`.

[51] N. Kameda, N. Sogoshi, and S. Nakabayashi. Surface Science, 602(8):1579 – 1584, 2008. ISSN 0039-6028. doi:http://dx.doi.org/10.1016/j.susc.2008.02.023. URL `http://www.sciencedirect.com/science/article/pii/S0039602808001131`.

[52] J. Yang, J. Duan, D. Fornasiero, , and J. Ralston. The Journal of Physical Chemistry B, 107(25):6139–6147, 2003. doi:10.1021/jp0224113. URL `http://dx.doi.org/10.1021/jp0224113`.

[53] C. U. Chan and C.-D. Ohl. Phys. Rev. Lett., 109:174501, Oct 2012. doi:10.1103/PhysRevLett.109.174501. URL `http://link.aps.org/doi/10.1103/PhysRevLett.109.174501`.

[54] V. Belova, M. Krasowska, D. Wang, J. Ralston, D. G. Shchukin, and H. Mohwald. Chem. Sci., 4:248–256, 2013. doi:10.1039/C2SC21321D. URL `http://dx.doi.org/10.1039/C2SC21321D`.

[55] W. Walczyk, N. Hain, and H. Schonherr. Soft Matter, 10:5945–5954, 2014. doi:10.1039/C4SM01024H. URL `http://dx.doi.org/10.1039/C4SM01024H`.

[56] X. Zhang, D. Y. C. Chan, D. Wang, and N. Maeda. Langmuir, 29(4):1017–1023, 2013. doi:10.1021/la303837c. URL `http://dx.doi.org/10.1021/la303837c`. PMID: 23234353.

[57] Y. Liu and X. Zhang. The Journal of Chemical Physics, 138(1):014706, 2013. doi:http://dx.doi.org/10.1063/1.4773249. URL `http://scitation.aip.org/content/aip/journal/jcp/138/1/10.1063/1.4773249`.

[58] X. H. Zhang, A. Khan, and W. A. Ducker. Phys. Rev. Lett., 98:136101, Mar 2007. doi:10.1103/PhysRevLett.98.136101. URL `http://link.aps.org/doi/10.1103/PhysRevLett.98.136101`.

[59] X. Zhang, J. Ren, H. Yang, Y. He, J. Tan, and G. G. Qiao. Soft Matter, 8:

4314–4317, 2012. doi:10.1039/C2SM07267J. URL `http://dx.doi.org/10.1039/C2SM07267J`.

[60] S. Peng, D. Lohse, and X. Zhang. Langmuir, 30(33):10043–10049, 2014. doi:10.1021/la5022774.

[61] X. H. Zhang, X. D. Zhang, S. T. Lou, Z. X. Zhang, J. L. Sun, , and J. Hu. Langmuir, 20(9):3813–3815, 2004. doi:10.1021/la0364542. URL `http://dx.doi.org/10.1021/la0364542`. PMID: 15875421.

[62] X. H. Zhang, , and W. Ducker. Langmuir, 23(25):12478–12480, 2007. doi:10.1021/la702453g. URL `http://dx.doi.org/10.1021/la702453g`. PMID: 17973512.

[63] H. Yang, S. Peng, X. Hao, T. A. Smith, G. G. Qiao, and X. Zhang. Soft Matter, 10: 957–964, 2014. doi:10.1039/C3SM52568F. URL `http://dx.doi.org/10.1039/C3SM52568F`.

[64] J. Turner and J. Turner. Buoyancy Effects in Fluids. Cambridge Monographs on Mechanics. Cambridge University Press, 1979. ISBN 9780521297264. URL `https://books.google.co.uk/books?id=x8NqYA97-wMC`.

[65] U. Frisch, B. Hasslacher, and Y. Pomeau. Phys. Rev. Lett., 56:1505–1508, Apr 1986. doi:10.1103/PhysRevLett.56.1505. URL `http://link.aps.org/doi/10.1103/PhysRevLett.56.1505`.

[66] D. Rothman and S. Zaleski. Lattice-Gas Cellular Automata: Simple Models of Complex Hydrodynamics. Alea-Saclay. Cambridge University Press, 2004. ISBN 9780521607605. URL `https://books.google.co.uk/books?id=STHngizh7LoC`.

[67] B. Chopard and M. Droz. Cellular Automata Modeling of Physical Systems. Alea-Saclay. Cambridge University Press, 2005. ISBN 9780521673457. URL `https://books.google.co.uk/books?id=jfcxaoNZuMUC`.

[68] J. Rivet and J. Boon. Lattice Gas Hydrodynamics. Cambridge Nonlinear Science Series. Cambridge University Press, 2005. ISBN 9780521019712. URL `https://books.google.co.uk/books?id=3gaK_X-XOWAC`.

[69] G. R. McNamara and G. Zanetti. Phys. Rev. Lett., 61:2332–2335, Nov 1988.

doi:10.1103/PhysRevLett.61.2332. URL `http://link.aps.org/doi/10.1103/PhysRevLett.61.2332`.

[70] F. J. Higuera and J. Jimenez. EPL (Europhysics Letters), 9(7):663, 1989. URL `http://stacks.iop.org/0295-5075/9/i=7/a=009`.

[71] K. Huang. Statistical mechanics. Wiley, 1987. ISBN 9780471815181. URL `https://books.google.co.uk/books?id=M8PvAAAAMAAJ`.

[72] C. Cercignani. The Boltzmann Equation and Its Applications. Applied Mathematical Sciences. Springer New York, 2012. ISBN 9781461210399. URL `https://books.google.co.uk/books?id=0cTcBwAAQBAJ`.

[73] M. Born and H. S. Green. Proceedings of the Royal Society of London A: Mathematical, Physical and Engineering Sciences, 188(1012):10–18, 1946. ISSN 0080-4630. doi:10.1098/rspa.1946.0093. URL `http://rspa.royalsocietypublishing.org/content/188/1012/10`.

[74] J. G. Kirkwood. The Journal of Chemical Physics, 15(1), 1947.

[75] J. Yvon. La theorie statistique des fluides et l'equation d'etat. Actualites scientifiques et industrielles. Hermann & cie, 1935. URL `https://books.google.co.uk/books?id=S1I_AQAAIAAJ`.

[76] N. Bogoliubov. Journal of Experimental and Theoretical Physics, 16(8):691–702, 1946.

[77] S. Chapman and T. Cowling. The Mathematical Theory of Non-uniform Gases: An Account of the Kinetic Theory of Viscosity, Thermal Conduction and Diffusion in Gases. Cambridge Mathematical Library. Cambridge University Press, 1970. ISBN 9780521408448. URL `https://books.google.co.uk/books?id=Cbp5JP2OTrwC`.

[78] H. Grad. Principles of the Kinetic Theory of Gases, pages 205–294. Springer Berlin Heidelberg, Berlin, Heidelberg, 1958. ISBN 978-3-642-45892-7. doi:10.1007/978-3-642-45892-7_3. URL `http://dx.doi.org/10.1007/978-3-642-45892-7_3`.

[79] P. L. Bhatnagar, E. P. Gross, and M. Krook. Phys. Rev., 94:511–525, May 1954.

doi:10.1103/PhysRev.94.511. URL http://dx.doi.org/10.1103/PhysRev.94.511.

[80] A. J. Wagner. Adt. notes for Statistical Mechanics, 463:663, 2008.

[81] D. R. Noble, S. Chen, J. G. Georgiadis, and R. O. Buckius. Physics of Fluids, 7 (1), 1995.

[82] T. Inamuro, M. Yoshino, and F. Ogino. Physics of Fluids, 7(12), 1995.

[83] S. Chen and G. D. Doolen. Annual Review of Fluid Mechanics, 30(1):329–364, 1998. doi:10.1146/annurev.fluid.30.1.329. URL http://dx.doi.org/10.1146/annurev.fluid.30.1.329.

[84] X. Shan and H. Chen. Phys. Rev. E, 47:1815–1819, Mar 1993. doi:10.1103/PhysRevE.47.1815. URL http://link.aps.org/doi/10.1103/PhysRevE.47.1815.

[85] X. Shan and H. Chen. Phys. Rev. E, 49:2941–2948, Apr 1994. doi:10.1103/PhysRevE.49.2941. URL http://link.aps.org/doi/10.1103/PhysRevE.49.2941.

[86] M. R. Swift, W. R. Osborn, and J. M. Yeomans. Phys. Rev. Lett., 75:830–833, Jul 1995. doi:10.1103/PhysRevLett.75.830. URL http://link.aps.org/doi/10.1103/PhysRevLett.75.830.

[87] X. Shan and G. Doolen. Journal of Statistical Physics, 81(1-2):379–393, 1995.

[88] X. Shan. Phys. Rev. E, 73:047701, Apr 2006. doi:10.1103/PhysRevE.73.047701. URL http://link.aps.org/doi/10.1103/PhysRevE.73.047701.

[89] R. Benzi, L. Biferale, M. Sbragaglia, S. Succi, and F. Toschi. Phys. Rev. E, 74:021509, Aug 2006. doi:10.1103/PhysRevE.74.021509. URL http://link.aps.org/doi/10.1103/PhysRevE.74.021509.

[90] R. Benzi, L. Biferale, M. Sbragaglia, S. Succi, and F. Toschi. Journal of Fluid Mechanics, 548:257–280, 2 2006. ISSN 1469-7645. doi:10.1017/S0022112005007512. URL http://journals.cambridge.org/article_S0022112005007512.

[91] M. Sbragaglia, R. Benzi, L. Biferale, S. Succi, K. Sugiyama, and F. Toschi.

Phys. Rev. E, 75:026702, Feb 2007. doi:10.1103/PhysRevE.75.026702. URL http://link.aps.org/doi/10.1103/PhysRevE.75.026702.

[92] P. Yuan and L. Schaefer. Physics of Fluids, 18(4):042101, 2006. doi:http://dx.doi.org/10.1063/1.2187070. URL http://scitation.aip.org/content/aip/journal/pof2/18/4/10.1063/1.2187070;jsessionid=kiXMXJjMpX8MBrO-6zOZr77w.x-aip-live-02.

[93] A. Kupershtokh, D. Medvedev, and D. Karpov. Computers and Mathematics with Applications, 58(5):965 – 974, 2009. ISSN 0898-1221. doi:http://dx.doi.org/10.1016/j.camwa.2009.02.024. URL http://www.sciencedirect.com/science/article/pii/S0898122109001011. Mesoscopic Methods in Engineering and Science.

[94] X. Shan. Phys. Rev. E, 77:066702, Jun 2008. doi:10.1103/PhysRevE.77.066702. URL http://link.aps.org/doi/10.1103/PhysRevE.77.066702.

[95] R. Benzi, M. Sbragaglia, S. Succi, M. Bernaschi, and S. Chibbaro. The Journal of Chemical Physics, 131(10):104903, 2009. doi:http://dx.doi.org/10.1063/1.3216105. URL http://scitation.aip.org/content/aip/journal/jcp/131/10/10.1063/1.3216105.

[96] M. Sbragaglia and X. Shan. Phys. Rev. E, 84:036703, Sep 2011. doi:10.1103/PhysRevE.84.036703. URL http://link.aps.org/doi/10.1103/PhysRevE.84.036703.

[97] V. M. Kendon, M. E. Cates, I. Pagonabarraga, J.-C. Desplat, and P. Bladon. Journal of Fluid Mechanics, 440:147–203, 2001.

[98] A. Briant, A. Wagner, and J. Yeomans. Physical Review E, 69(3):031602, 2004.

[99] H. Kusumaatmaja, J. Leopoldes, A. Dupuis, and J. Yeomans. EPL (Europhysics Letters), 73(5):740, 2006.

[100] H. Kusumaatmaja and J. Yeomans. Langmuir, 23(11):6019–6032, 2007.

[101] T. Lee and L. Liu. Journal of Computational Physics, 229(20):8045–8063, 2010.

[102] B. M. Mognetti, H. Kusumaatmaja, and J. Yeomans. Faraday discussions, 146:153–165, 2010.

[103] A. Bray. Advances in Physics, 43(3):357–459, 1994. doi:10.1080/00018739400101505.

[104] H. Kusumaatmaja and J. M. Yeomans. Lattice boltzmann simulations of wetting and drop dynamics. In Simulating Complex Systems by Cellular Automata, pages 241–274. Springer Berlin Heidelberg, 2010. ISBN 9783642122026.

[105] R. Ledesma-Aguilar, D. Vella, and J. M. Yeomans. Soft Matter, 10:8267–8275, 2014. doi:10.1039/C4SM01291G. URL `http://dx.doi.org/10.1039/C4SM01291G`.

[106] D. N. Sibley, A. Nold, and S. Kalliadasis. Journal of Fluid Mechanics, 736:5–43, 12 2013. ISSN 1469-7645.

[107] P. G. de Gennes. Rev. Mod. Phys., 57:827–863, 1985.

[108] C. Huh and L. Scriven. Journal of Colloid and Interface Science, 35(1):85 – 101, 1971.

[109] P. Yue, C. Zhou, and J. J. Fend. Journal of Fluid Mechanics, 645:279–294, 2 2010. ISSN 1469-7645.

[110] A. J. Briant and J. M. Yeomans. Phys. Rev. E, 69:031603, 2004.

[111] D. Jacqmin. Journal of Fluid Mechanics, 402:57–88, 1 2000. ISSN 1469-7645.

[112] H. Kusumaatmaja, E. J. Hemingway, and S. M. Fielding. Journal of Fluid Mechanics, 788:209–227, 2 2016. doi:10.1017/jfm.2015.697.

[113] J.-C. Desplat, I. Pagonabarraga, and P. Bladon. Computer Physics Communications, 134(3):273 – 290, 2001. ISSN 0010-4655. doi:http://dx.doi.org/10.1016/S0010-4655(00)00205-8. URL `http://dx.doi.org/10.1016/S0010-4655(00)00205-8`.

[114] D. Lohse and X. Zhang. Rev. Mod. Phys., 87:981–1035, Aug 2015. doi:10.1103/RevModPhys.87.981. URL `http://dx.doi.org/10.1103/RevModPhys.87.981`.

[115] S. K. Aggarwal and F. Peng. J. Eng. Gas Turb. Power, 117:453–461, 1995.

[116] T. Kalwarczyk, N. Ziebacz, M. Fialkowski, and R. Holyst. Langmuir, 24(13):6433–6440, 2008. doi:10.1021/la704003q. URL `http://dx.doi.org/10.1021/`

la704003q. PMID: 18507426.

[117] P. S. Sanchez. Modeling the dispersion and evaporation of sprays in aeronautical combustion chambers. PhD thesis, Institut National Polytechnique de Toulouse, 2012.

[118] M. Rohloff, T. Lapp, and J. Vollmer. arXiv:1411.7882v1, 2014.

[119] J. H. Weijs, J. R. T. Seddon, and D. Lohse. ChemPhysChem, 13(8):2197–2204, 2012. ISSN 1439-7641. doi:10.1002/cphc.201100807. URL http://dx.doi.org/10.1002/cphc.201100807.

[120] J. H. Weijs and D. Lohse. Phys. Rev. Lett., 110:054501, Jan 2013.

[121] O. Carrier, N. Shahidzadeh-Bonn, R. Zargar, M. Aytouna, M. Habibi, J. Eggers, and D. Bonn. www.maths.bris.ac.uk/majge/evaporationwater_v32012.03.40.pdf accessed April 2016.

[122] H. Gelderblom, A. G. Marin, H. Nair, A. van Houselt, L. Lefferts, J. H. Snoeijer, and D. Lohse. Phys. Rev. E, 83:026306, Feb 2011. doi:10.1103/PhysRevE.83.026306. URL http://dx.doi.org/10.1103/PhysRevE.83.026306.

[123] A. J. D. Shaikeea and S. Basu. Langmuir, 32(5):1309–1318, 2016.

[124] F. Carle, S. Semenov, M. Medale, and D. Brutin. International Journal of Thermal Sciences, 101:35 – 47, 2016.

[125] R. C. A. van der Veen, T. Tran, D. Lohse, and C. Sun. Phys. Rev. E, 85:026315, Feb 2012.

[126] B. Roman and J. Bico. Journal of Physics: Condensed Matter, 22(49):493101, 2010.

[127] J. Bico, B. Roman, L. Moulin, and A. Boudaoud. Nature, 432(7018):690, 2004.

[128] C. Py, P. Reverdy, L. Doppler, J. Bico, B. Roman, and C. N. Baroud. Phys. Rev. Lett., 98:156103, Apr 2007.

[129] T. Tanaka, M. Morigami, and N. Atoda. Japanese Journal of Applied Physics, 32(12S):6059, 1993.

[130] J. Ju, H. Bai, Y. Zheng, T. Zhao, R. Fang, and L. Jiang. Nature Communications,

3, 2012.

[131] A. Parker and C. Lawrence. Nature, 414(6859):33–34, 2001.

[132] K.-H. Chu, R. Xiao, and E. N. Wang. Nature Materials, 9(5):413–417, 2010.

[133] T. T. Al-Housseiny, P. A. Tsai, and H. A. Stone. Nat Phys, 8(10):747–750, Oct 2012.

[134] L. Keiser, R. Herbaut, J. Bico, and E. Reyssat. Journal of Fluid Mechanics, 790: 619–633, 3 2016. ISSN 1469-7645.

[135] R. Ledesma-Aguilar. private communication.

[136] A. Bejan. Convection Heat Transfer. Wiley, 2004. ISBN 9780471271505. URL `https://books.google.co.uk/books?id=T6keAQAAIAAJ`.

[137] P. G. Saffman and G. Taylor. The penetration of a fluid into a porous medium or hele-shaw cell containing a more viscous liquid. In Proceedings of the Royal Society of London A: Mathematical, Physical and Engineering Sciences, volume 245, pages 312–329. The Royal Society, 1958.